UNIVERSITY OF CALIFORNIA
SANTA CRUZ

THE QUANTIFICATION OF CO-OCCURRING METEOROLOGICAL EXTREMES AND THE ANTHROPOGENIC CONTRIBUTION TO HYDROMETEOROLOGICAL VARIATION

A dissertation submitted in partial satisfaction of the
requirements for the degree of

DOCTOR OF PHILOSOPHY

in

EARTH SCIENCES

by

John Patrick O'Brien

December 2019

The Dissertation of John Patrick O'Brien
is approved:

Professor Patrick Y. Chuang, Chair

Research Scientist Travis A. O'Brien

Research Scientist Christina M. Patricola

Professor Nicole Feldl

Quentin Williams
Vice Provost and Dean of Graduate Studies

Table of Contents

List of Figures

Abstract

The Quantification of Co-occurring Meteorological Extremes and the Anthropogenic Contribution to Hydrometeorological Variation

by

John Patrick O'Brien

It is a well-established fact that the present climate is changing as a result of human activities, the implications of which we are just now beginning realize. From record breaking heatwaves, wildfires, and extreme droughts, to sea level rise, ocean acidification, and severe flooding, there is little doubt that the consequences of anthropogenically driven climate change are wide and far reaching. One of the most confounding problems to date in understanding the effects of a changing climate is the absence of a world with a climate free from human interference to which to compare. The chaotic nature of atmospheric motions, naturally occurring low-frequency oscillations, and extreme events are all an inherent part of the climate system, and within that naturally occurring variability exists the signature of human interference with the global climate system. Thus the overarching aim of this dissertation is to describe, understand, and quantify the nature of extreme meteorological events in a climate subject to both natural and human induced forcings. In Chapter one, we employ a novel nonparametric probability density estimation method that allows for the characterization of nonlinear multivariant relationships among climatological variables. We develop and use this framework to quantify the multivariant relationships that exist between California wintertime temperature and pre-

cipitation as a function of naturally occurring low-frequency modes of variability to understand how they alter the probabilities for experiencing co-occurring extremes. Of the several modes studied, we find that a circumpolar Rossby wave of wave number 5 is uniquely capable of simultaneously driving both high temperatures and low precipitation thereby inducing or exacerbating antecedent drought conditions. Chapters two and three both employ two large ensembles of global climate model simulations. One ensemble is configured to represent the climate as it is today and the other configured to represent the best estimate of what the climate would have looked like in the absence of human interference. In chapter two we leverage the statistical power provided by the large ensembles to study the anthropogenic influence on the spatio-temporal characteristics of extreme hydrometeorological events across the continental U.S. from 1960-2018. We identify an anthropogenic signal at nearly every time scale considered and find that hydrometeorological events characteristic of the mean scale at approximately Clausius-Clapeyron ($7\%\mathrm{K}^{-1}$), while extreme events representing the 99^{th} percentile are found to scale at nearly double that rate. In Chapter three, we use the same dataset to isolate and quantify the human contribution to the observed hydroclimate variability. We find that anthropogenic forcing has resulted in a large increase in western U.S. hydroclimate variability and volatility, a decrease predictability for any given ocean state, and to simultaneously permit an increased probability for both droughts and floods in California. Our results suggest that the outcomes of both the strong El Niño of 2015/16 failing to drive the expected hydroclimate response in California and the following extremely wet winter of 2016/17 were both made more likely as a result of anthropogenic forcing.

To my parents for always supporting my questionable life choices

and for never urging me to be practical... It has led me here.

Thank you

Acknowledgments

Travis O'Brien has literally been the best advisor I could have ever hoped for. The depth of his knowledge and countless talents are only surpassed by the depth of his patience, compassion, and heart. Travis took me on as a graduate student five and a half years ago, and from day one, his steadfastness and diligence in seeing me succeed has not wavered one iota.

Chris Patricola has also been an amazing and tremendous source of support, encouragement, and always incredibly insightful feedback on any questions I have brought to her. Chris joined my committee three years ago and like Travis, she has been unwavering in her dedication to always putting in the time and effort to give me any support I've needed, even when I didn't know I needed it.

Travis and Chris have been my primary advisors over the course of my Ph.D and together they have provided me with the best support and guidance I could have ever hoped for. My committee members at U.C. Santa Cruz, Patrick Chuang and Nicole Feldl have been equally supportive and encouraging and have always seen to ensuring my success and forward progress. Together, my committee has been beyond excellent and without their guidance and inspiration this dissertation would not have been possible.

Further, the people in the CASCADE SFA specifically, and more generally, those at Lawrence Berkeley National Laboratory have been absolutely instrumental in my success. The broader group of people at LBNL I have met there and worked with along the way, have in addition to becoming scientific colleagues, also have become life-long friends, and I am deeply indebted to, and grateful for them all.

Introduction

Since the industrial revolution, human activities have significantly altered the composition of the global atmosphere, primarily from the combustion of fossil fuels, and have further modified the environment through the physical alteration of the landscape itself. These changes have in turn affected the behavior and character of the global climate system, seen in the observed rise in global mean temperatures and the increased occurrence of extreme events such as drought, heat waves, and extreme precipitation among others. Recent research indicates that changes to the nature and probability of occurrence of such extreme events are being caused by human activities. However, extreme events are also a fundamental part of nature, and have always occurred regardless of any human influences. Thus, as a critical and parallel component to understanding the anthropogenic contribution to changes in extremes, it is also necessary to understand their spatio-temporal characteristics as a function of natural climate variability.

Human societies, ecological systems, and the natural environment have long been subject to extreme weather and dramatic climate fluctuations. The Intergovernmental panel on Climate Change (IPCC) defines extremes as weather phenomena that are either very infrequent or unusually intense under historical climatological

conditions (IPCC, 2012). Extremes, although by definition rare, have strong and disproportionate effects on human and natural systems. It is exactly because of the rarity of meteorological and climatological extremes that human societies, ecological, and environmental systems are not well adapted to cope with them and as such, often sustain tremendous damage when extreme events occur. Examples include heat waves, cold snaps, droughts, wildfires, extreme rainfall, floods, extreme snow and ice storms, and tropical cyclones, to name but a few. While temporally infrequent and spatially limited, the impacts stemming from these types of events can be substantial. For example, during the European heatwave of 2003, extreme maximum temperatures of 35-40°C were repeatedly recorded in July and August (Cassardo et al., 2007), which resulted in excess of 70,000 fatalities across Europe (Robine et al., 2008). The 2011-2015 California drought caused multi-billion dollar losses due to extensive regions of farmland laid fallow from the lack of available irrigation water (Medellín-Azuara et al., 2016). Further, across California's widespread forest regions, an estimated 3.3 million trees were killed and wide swaths of drought-weakened forest have experienced higher mortality rates due to infestations of bark beetles and other wood borers (Moore and Ellis, 2015). This in turn has increased the risk of wildfire conflagrations, which in 2015, wildfires burned over 750,000 acres destroying over 3,200 structures in California (CAL FIRE., 2015). In 2005, Hurricane Katrina battered the U.S. Gulf Coast resulting in at least 500,000 people evacuating and never returning (Reardon, 2015), over 1800 fatalities, 800,000 housing units destroyed or damaged, and total estimated costs of over $250 billion (Glantz, 2008).

Given the profound and disproportionate impacts of extreme events, an accurate and comprehensive characterization and prediction of extremes would be important even in the absence of a changing climate. However, climate change is projected to appreciably alter the background state of the climate system, and in fact is already doing so, thereby altering the meteorological conditions under which extremes form. In the latter half of the 20th century, a period dominated by global mean temperature rise primarily attributable to anthropogenic influences, temperature records indicate an increasing number of warm nights, decreasing number of frost days, and decreases in the intra-annual extreme temperature range (Frich et al., 2002). Currently, at an observed warming of 0.85°C, the probability of 1-in-1,000-day hot extreme over land is about five times higher than in pre-industrial conditions – that is, roughly 75% of those moderate hot extremes are attributable to global mean temperature rise (Fischer and Knutti, 2015). Similarly, trends in precipitation have also emerged, showing increasing numbers of wet days, maximum five day accumulations, and decreasing a number of consecutive dry days (Frich et al., 2002). Additionally, in the present-day climate, the probability of experiencing a daily precipitation extreme in the 99.9 percentile has increased 1.2 times above pre-industrial controls, and 18% of that increase is attributable to human influence (Fischer and Knutti, 2015). Changes to temporal trends and spatial patterns in precipitation and the occurrence of extremes in a warming climate are complex, but not unexpected. First, the amount of precipitable water in the Earth's atmosphere is growing at the rate of approximately 5-6%/°C as a consequence of the global mean temperature rise (Flato et al., 2014). Second, Arctic amplifica-

tion reduces the surface meridional temperature gradient while upper tropospheric warming/cooling near the tropics/poles due to GHG forcing results in equatorward and poleward shifts respectively of the extratropical storm tracks (Shaw et al., 2016, Barnes and Screen, 2015). Third, the physics of radiative convective equilibrium and global mean temperature rise dictate that global mean rainfall increases at approximately 2%/°C, and the difference between this rate of growth and that for water vapor implies that the probability distribution function (PDF) of precipitation has to "broaden," leading to both more downpours and more frequent and severe droughts (Flato et al., 2014, Allen and Ingram, 2002, Held and Soden, 2006, O'Gorman and Schneider, 2009). Taken as a whole, projections into the 21st century suggest that wet regions will become wetter and dry regions will become drier, by increasing hourly and daily precipitation extremes, while heat waves and droughts will simultaneously increase in intensity, duration, and frequency (Held and Soden, 2006, O'Gorman and Schneider, 2009, Trenberth, 2011, Prein et al., 2017, Meehl, 2004, Sheffield and Wood, 2008).

Societal changes, such as higher concentrations of people living in coastal and urban settings and aging infrastructure, have made us more susceptible to environmental fluctuations than we ever have been. Thus, there is little doubt that society as a whole has become more exposed to meteorological and climatological extremes (Kunkel et al., 1999). The threats posed to infrastructure by climate-change-intensified meteorological extremes reach far beyond the loss of the infrastructure itself. The impacts and disruptions resulting from extreme events involve not only the costs associated with the cleanup, repair, and/or replacement of affected in-

frastructures but also the economic, social, and environmental effects as supply chains are disrupted, economic activities are suspended, and/or social well-being is threatened (Wilbanks and Fernandez, 2014). Further, extreme meteorological event-induced failures and disruptions often cascade across infrastructures because of extensive interdependencies – threatening health and local economies, especially in areas where human populations and economic activities are concentrated in urban areas (Wilbanks and Fernandez, 2014). There also exist separate but parallel threats to human health and well-being resulting from both direct and indirect impacts. For example, heat waves and the effects of thermal stress on human physiology have shown a direct and positive correlation with mortality in elderly people (Basu, 2002), and especially elderly women (Díaz et al., 2002). Since 1900, floods resulting from extreme precipitation have killed nearly 7 million people worldwide (EM-DAT, 2016). The health impacts from floods can be immediate, such as fatalities due to drowning; however, they can also be indirect and delayed, such as allowing human and animal wastes to seep into drinking water supplies, facilitating the transmission of waterborne infectious diseases. In the United States, 51% of waterborne disease outbreaks between 1948 and 1994 were preceded by precipitation events exceeding the 90^{th} percentile (Curriero et al., 2001). However, of all meteorological extremes, droughts tend to take the highest human toll due to their large areal extent, the impact on crop yields and food supplies, the reduction of potable water, the increases in stagnant water that facilitates mosquito breeding and the propagation of infectious diseases, and the societal and political disruptions that can occur as a result of drought stresses. For example, the Syrian drought stretching

from 2006-2011, made 2 to 3 times more likely by anthropogenic forcing, resulted in massive agricultural failures and livestock mortality, an exodus of over 1.5 million people, and ultimately the onset of the Syrian civil war (Kelley et al., 2015).

As we move into a future that will almost certainly be characterized by unabated carbon emissions, and as a consequence, a changing climate, the combination of increasing extremes, an exponentially increasing population, and aging infrastructures present a potentially disastrous intersection for present and future generations. Regions such as California, USA, will face changing pressures on many fronts. An increasing demand for water resources from competing interests such as municipal districts, agricultural sectors, and environmental advocacy groups will place unique pressures on an already stressed system. Projected increasing water-cycle extremes and inter-annual variability will complicate the planning, distribution, and politics of water resource allocation. At the same time, the combination of aging infrastructures and inadequate design to handle more extreme extremes will introduce a greater degree of uncertainty regarding how best to plan for both years of longer and deeper droughts and years of more intense precipitation and flooding. Understanding and planning for these opposing extremes presents a unique challenge both scientifically and politically. While much is known about heat extremes, drought extremes, and precipitation extremes individually (e.g., see the lit. review in this section), very little is known about what controls their co-occurrence regionally and globally.

Chapter one of this dissertation focuses on understanding and quantifying the nature and drivers of co-occurring extreme events. We develop a novel approach to

do this by employing a state-of-the-science probability density estimation method capable of evaluating complex multivariate nonlinear relationships among variables. We develop this framework using California wintertime temperature and precipitation as a test bed. This choice is motivated by the extreme drought of 2011-2015, which was characterized by not only by an extreme dearth of rainfall, but also record high temperatures. The spatio-temporally co-located occurrence of these two extremes led to the most extreme drought California has experienced on observational record (Seager et al., 2015). We evaluate the bivariate relationship between temperature and precipitation in a probabilistic framework using indices which capture large-scale modes of change as covariates. Naturally occurring low-frequency oscillations (modes of variability) are well known to alter the probabilities for single extreme events. However, it is not clear how these modes of variability modulate the probabilities for extremes jointly. Moreover, we also consider global mean temperature rise as a covariate as well since it is one of the defining modes of change occurring today. Therefore, following from the unique stresses caused by extremes and the lack of knowledge about how they co-vary in a natural and anthropogenically forced climate, Chapter one focuses on addressing the following three questions:

- *What are the contributions of natural variability and large-scale climate forcings to relationships in single and co-occurring extremes and what are the relevant physical processes that drive such changes?*

- *How does accounting for large-scale drivers such as SST and CO2 forcings affect the probability and frequency of experiencing co-occurring extremes in California wintertime temperature and precipitation?*

- *Does the treatment of extremes in this experimental nonparametric framework reproduce known results and does the explicit accounting for nonstationarity lead to new conclusions?*

Chapter two is aimed at detecting and attributing the anthropogenically forced component of changes to extreme hydrometeorological events in the observed record. We focus our analysis across a range of temporal and spatial scales to identify potentially nonuniform and disproportionate expressions of anthropogenic influence. To do this we employ two large ensembles of global climate model simulations run under two different protocols. The first ensemble is configured with all observed radiative and oceanic forcings and is meant to simulate the climate as it is today. The second ensemble is configured using the same radiative and oceanic forcings, however, the best estimate of the human induced radiative component to the model boundary conditions has been removed, and therefore the simulations represent our best estimate of what the world today might have been had humans not been around. Both ensembles share the same ocean variability and total 50 members each spanning the period from 1960-2018 resulting in 2950 simulated years each. We focus our analysis over the continental Unites States (CONUS) and consider time-scales ranging from 1-day to seasonal accumulations across the November-March time period. Using the output from the two large ensembles of simulations we address the following questions:

- *When controlling for the observed natural variability in the climate system, what conclusions do we reach about the anthropogenic contributions to hydrometerlogical extreme events?*

- *Are the effects of anthropogenic forcing on hydrometerlogical extremes expressed and distributed equally across all temporal and spatial scales?*

- *Does using large ensembles of simulations lead to more robust statistical conclusions about the impact of anthropogenic forcing on mean and extreme hydrometerlogical events?*

Chapter three builds on the work of Chapter two by addressing the anthropogenic contribution to hydrometeorological variability. As previously described, extreme events are disproportionately impactful to human and environmental systems. However, additionally, their temporal variation year-to-year greatly complicates adapting to, and planning for, their disproportionate impacts. We employ the same large ensembles leveraged for the analysis in Chapter two, but instead we quantify the temporal variability of December-February (DJF) average precipitation rate from year-to-year. We begin with a global analysis isolating the contribution to temporal variability forced by the common boundary condition to all ensemble members, that is, the component of variability forced by ocean variability. From this we can then isolate and identify the residual variability that results from anthropogenic forcing. We identify regions in the northern hemisphere (a focus on the boreal winter) where anthropogenic contributions to increased variability are most strongly expressed. We then focus in on the continental U.S., and in particular the western U.S. where the anthropogenic contribution to increased temporal variability stands out the most, for a detailed analysis. We decompose how, when, and where excess variability is expressed and quantify its implications on hydroclimate predictability and volatility. Chapter three addresses the following main questions:

- *When controlling for naturally occurring variability, how has anthropogenic forcing altered the temporal distribution of hydrometeorological extremes?*

- *Is year-to-year anthropogenically induced excess variability expressed equally in all years or have some years become disproportionately more variable and less predictable than others?*

- *Within each year, is the anthropogenically induced excess variability expressed equally in all percentiles of the precipitation distribution?*

With an overarching focus on the western U.S. and California climate, the original research contained in this dissertation is directly aimed at addressing these critically important questions. Ultimately, it is the author's goal to provide scientifically accurate results to advance the understanding of the changing climate system, and to help inform decision-makers and stakeholders alike on how to move forward in the face of the unique and pressing challenges posed by meteorological and climatological extreme events.

This page left intentionally blank.

Chapter 1

Metrics for Understanding Large-scale Controls of Multivariate Temperature and Precipitation Variability

Climate Dynamics (2019) 53:3805–3823
https://doi.org/10.1007/s00382-019-04749-6

Metrics for understanding large-scale controls of multivariate temperature and precipitation variability

John P. O'Brien[1,2] · Travis A. O'Brien[2] · Christina M. Patricola[2] · S.-Y. Simon Wang[3]

Received: 25 October 2018 / Accepted: 26 March 2019 / Published online: 16 April 2019

Abstract
Two or more spatio-temporally co-located meteorological/climatological extremes (co-occurring extremes) place far greater stress on human and ecological systems than any single extreme could. This was observed during the California drought of 2011–2015 where multiple years of negative precipitation anomalies occurred simultaneously with positive temperature anomalies resulting in California's worst drought on observational record. The large-scale drivers which modulate the occurrence of extremes in two or more variables remains largely unexplored. Using California wintertime (November–April) temperature and precipitation as a case study, we apply a novel, nonparametric conditional probability distribution method that allows for evaluation of complex, multivariate, and nonlinear relationships that exist among temperature, precipitation, and various indicators of large-scale climate variability and change. We find that multivariate variability and statistics of temperature and precipitation exhibit strong spatial variation across scales that are often treated as being homogeneous. Further, we demonstrate that the multivariate statistics of temperature and precipitation are highly non-stationary and therefore require more robust and sophisticated statistical techniques for accurate characterization. Of all the indicators of the large-scale climate conditions we studied, the dipole index explains the greatest fraction of multivariate variability in the co-occurrence of California wintertime extremes in temperature and precipitation.

Keywords ENSO · El Niño · La Niña · PDO · AMO · Global change · Climate variability · Teleconnections · California · Joint extremes · Precipitation extremes · Non-stationarity

1 Introduction

Single meteorological or climatological extremes have a strong and disproportionate impact on societies, ecological systems, and natural environments. However, the joint occurrence of two or more co-occurring extremes has the potential to negatively impact human and natural systems in ways far greater than any single event could (Leonard et al. 2014). For example, drought is commonly thought of as a result of only a lack of precipitation, i.e. meteorological drought. However, negative precipitation anomalies co-occurring with positive temperature anomalies can greatly exacerbate drought conditions due to the increased evapotranspirative demand placed on the system, i.e. agricultural drought (AghaKouchak et al. 2014; Diffenbaugh et al. 2015). Positive temperature anomalies coupled with high humidity can result in extreme heat index values, which can be detrimental to human health (Steadman 1979; Wehner et al. 2016). Flooding can result from both unusually intense precipitation events and unusually long-lived events; however, when unusually long-lived

Electronic supplementary material The online version of this article (https://doi.org/10.1007/s00382-019-04749-6) contains supplementary material, which is available to authorized users.

✉ Travis A. O'Brien
taobrien@lbl.gov

John P. O'Brien
jopobrie@ucsc.edu

Christina M. Patricola
cmpatricola@lbl.gov

S.-Y. Simon Wang
simon.wang@usu.edu

[1] Department of Earth and Planetary Sciences, University of California, Santa Cruz, 1156 High Street, Santa Cruz, CA 95064, USA

[2] Climate and Ecosystem Sciences Division, Lawrence Berkeley National Laboratory, 1 Cyclotron Rd, MS74R-316C, Berkeley, CA 94720, USA

[3] Department of Plants, Soils and Climate, Utah State University, 4820 Old Main Hill, Logan, UT 84322, USA

events are also unusually intense in terms of their precipitation rate, flooding can be abrupt and extreme, leading to loss of life, property damage, and severely compromised infrastructure. While much is known about heat extremes, drought extremes, and precipitation extremes individually, little is known about what controls their co-occurrence both regionally and globally.

Understanding what controls the co-occurrence of extremes, their natural variability, and how they have changed in past, present, and future climates is challenging in light of anthropogenic forcing and the lack of a historical analogue that could shed light on the climate response to such forcing. In addition to anthropogenic forcing, variability also arises naturally from the presence of large-scale, low-frequency atmosphere–ocean interactions known as teleconnections (Polade et al. 2013). These modes of variability are well-documented to have a detectable signature on climatological precipitation and temperature patterns and to modulate the occurrence of extremes (Cayan et al. 1999; Krichak et al. 2014). To date, few studies have focused on the role large-scale climate patterns play in driving and altering the probabilities for experiencing co-occurring extremes. Diffenbaugh et al. (2015) demonstrated that the occurrence of drought has been exacerbated by anthropogenic factors, specifically in California, USA, by increasing the probability that any given dry year(s) will coincide with warm years. AghaKouchak et al. (2014) showed that the return period for the hot and dry conditions that prevailed during the California winter of 2014 was dramatically increased by considering the joint probability of temperature and precipitation (AghaKouchak et al. 2014). While these and similar studies begin to address the role that large-scale climate conditions may play in modulating extremes and their joint occurrence, there has been no systematic study that addresses the role modes of variability play in altering the probabilities for experiencing co-occurring extremes. Further, previous studies (e.g. AghaKouchak et al. 2014) assume that the statistics of meteorological and climatological variables are stationary, meaning that the descriptive statistics of variables do not change over time. However, given the influence these modes of variability have on California's hydroclimate and the significant alteration of the background state of the climate by human activities, it is reasonable to assume that climate statistics are not stationary (Serinaldi and Kilsby 2015). To account for nonstationarity in higher dimensional distributions Sarhadi et al. (2018) employ a vine copula approach to assess the change in risk of hot and dry conditions in CMIP5 models resulting from human activities, but do not consider the roles of natural modes of variability have on the bivariate distributions.

To address the highlighted gap in knowledge, we use California as a testbed for exploring the influence of natural variability and large-scale climate change on the multivariate statistics of temperature and precipitation. Specifically, we seek to understand the role teleconnections play in modulating the wintertime co-occurrence of extremes, while at the same time addressing the potential violation of data stationarity assumptions. We achieve this by directly estimating joint conditional probability density functions of temperature and precipitation, in two representative California regions, conditional on several indices of natural variability and climate change. Using this methodology, we seek to understand: (1) How the joint probability of California temperature and precipitation is modulated by several well-known teleconnections that potentially affect California's climate, (2) How the strength of each climate mode varies regionally within California, and (3) the degree to which teleconnections modulate return intervals of co-occurring extremes in temperature and precipitation. Considering California's rapidly increasing population and, hence, water demands, we place particular emphasis on understanding joint occurrences of wintertime extremes in high temperature and low precipitation anomalies, which greatly exacerbate drought conditions, as was observed in 2014. Quantifying the contributions from naturally occurring modes of variability is a key requirement for isolating and understanding the role anthropogenic forcing plays in modulating the pattern of occurrence of extremes and their co-occurrence. However, the goal here moving forward will be to document the roles various modes of natural variability have in the altering probabilities of co-occurring extremes in temperature and precipitation rather than to disentangle natural variation from anthropogenic forcing.

2 Methods

2.1 Data

For this study we employ NOAA's, National Centers for Environmental Information, NCEI (formerly NCDC), temperature and precipitation datasets for California (Center USNCD 2016). The temperature and precipitation data consist of station data, averaged within regions known as climate divisions, geographically defined to encompass broadly similar regional climates. These data are averaged to monthly time periods and extend from 1895 to present. For each climate division in California we then temporally average these data across the wintertime, wet-season period, defined here to be the six month period extending from November through April the following calender year. We use the data extending from November, 1895 to April, 2017 resulting in 122 wet-season periods. To study California's joint wintertime temperature and precipitation dependence on the large-scale state of the climate, we leverage five datasets. To

study the El Niño Southern Oscillation (ENSO) dependence we use the Multivariate ENSO Index (MEI) (Wolter and Timlin 1993). Pacific Decadal Oscillation (PDO) dependence is modeled using the time series from NCEI (Center USNCD 2016), as originally derived by Mantua et al. (1997). The Atlantic Multidecadal Oscillation data is obtained from ESRL (Enfield et al. 2001). The North American winter "dipole index" (DPI) (Wang et al. 2014, 2015) is calculated from both twentieth century reanalysis (20CR) (Compo et al. 2011) and NCEP reanalysis II (Kanamitsu et al. 2002). We use the NCEP data to fill in the years 2015, 2016, 2017, which are missing from the 20CR data. We do this using a simple linear correlation between the two datasets and then use the linearly interpolated values. Integrated Vapor Transport (IVT) and 250 hPa temperature fields are calculated from the ERA-20C dataset (Poli et al. 2016). Finally, we consider the global mean temperature anomaly (GMTA) as reported by NOAA (Center USNCD 2016). These conditioning datasets are averaged over the same time period as the temperature and precipitation data. No temporal lags are considered in this analysis.

The large-scale modes of variability we chose for primary analysis in this study, specifically, ENSO, PDO, AMO, DPI, and GMTA, were based on a several factors. First, we wanted to use modes of variability that were generally well-established, well-studied, and well-known across a wide range of disciplines. Second, we wanted to represent independent modes of variability arising from different genesis mechanisms: ENSO, PDO, and AMO are largely SST forced modes affecting remote locations through atmospheric teleconnections, while DPI and GMTA are largely connected to atmospheric variations only. We do note however, that according to Newman et al. (2016), ENSO and PDO are likely not independent of each other and that DPI is also likely to have a connection to SSTAs in the West Pacific Warm Pool (Wang et al. 2014; Teng and Branstator 2017; Swain et al. 2017). Finally, considering the wide array of climate indices available (National Center for Atmospheric Research Staff 2019; National Oceanic and Atmospheric Administration 2019), we also used a pairplot (Fig. S11) to help identify independent and correlated modes.

To assess regional variation of each climate mode we choose to focus on two climate divisions representing the coastal latitudinal end-members of the state. CD1 represents the coastal northern most division and is sparely populated, heavily forested, and typified by a temperate rain-forest climate. CD6 represents the coastal southern most climate division and is densely populated, with large areas of urban sprawl, and is typified by a largely arid, Mediterranean climate surrounded by a dry desert environment.

2.2 Probability density estimation

A central goal of this study is to understand how the joint statistics of temperature and precipitation depend on various large-scale modes of variability and climate change: conditional probability density functions. To this end, we employ the method of O'Brien et al., fastKDE (O'Brien et al. 2014, 2016), which objectively and directly computes non-parametric kernel density estimates based on the self-consistent, unbiased, and optimal method of Bernacchia and Pigolotti (2011). We estimate conditional probability density functions (cPDFs) directly from trivariate probability density estimates and marginal density estimates as follows:

$$\hat{\mathrm{P}}(R, T|X) = \frac{\hat{\mathrm{P}}(R, T, X)}{\hat{\mathrm{P}}(X)}, \tag{1}$$

where R and T denotes precipitation and temperature respectively, and X is the conditioning variable: $X \in$ (MEI, PDO, AMO, DPI, GMTA). Thus Eq. 1 is a trivariate function that gives the joint probability of co-occurring values of wintertime temperature and precipitation given the conditioning variable at a specific value. As such we are able to directly estimate the probability of co-occurring extreme winter temperature and precipitation as a function of indices of large-scale climate variability and change. Further, with this methodology we are able to explore the effects non-stationary in the data, with respect to the conditioning variables. This methodology allows us to uniquely isolate the influences of the given covariate on the joint distribution in a probabilistic framework (O'Brien et al. 2014). Error estimates on the cPDFs shown on panels d,e,i,j on all Figs. 1, 2, 3, 4 and 5 are derived from bootstrap resampling the data 5000 times and recalculating the cPDFs for each resampling. From the set of 5000 cPDFs, we calculate the 5th and 95th percentiles of the density estimates at each data value. The cPDFs on which we calculate the error estimates represent the PDFs associated with the P10/90 values of each mode of variability. We choose to compute the error on the P10/90 cPDFs such that we capture the end member behavior of the conditional distributions while at the same time retaining enough samples to be able to compute robust estimates of the conditional densities. The years associated with the respective modes of variability having winter averages less than (greater than) the P10 (P90) values are documented in Table S1.

3 Results

3.1 The ENSO conditional distributions

The El Niño-Southern Oscillation (ENSO) is a well-documented, naturally occurring coupled ocean–atmosphere

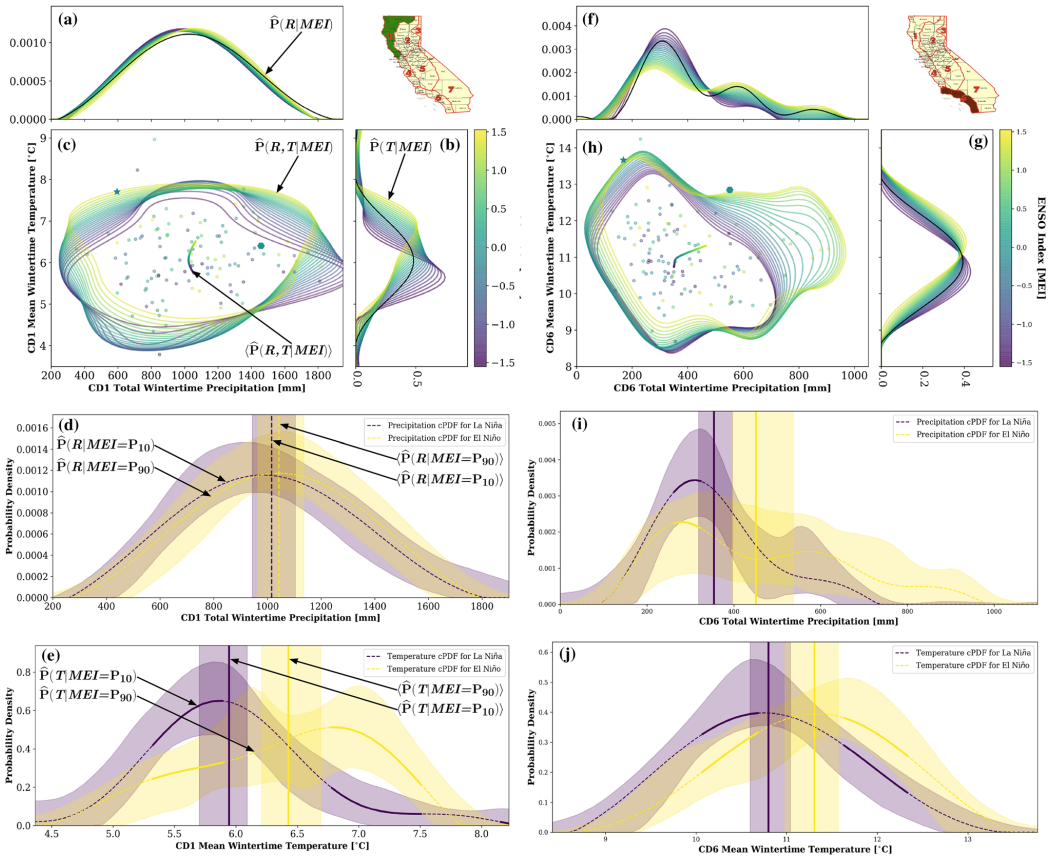

Fig. 1 **c** The fastKDE estimate of temperature versus precipitation, calculated as the wintertime spatiotemporal averages over stations within California, USA, climate division 1 (filled dots), and conditioned on (as a continuous function of) the ENSO strength phase (MEI index). Dots show data points that went into the fastKDE estimate. The starred and hexagon points represent 2014 and 2017 respectively, each colored by the MEI value corresponding to that year. The colored, closed contours (the colored wireframe) depict the levels of constant probability corresponding to the 95th percentile from the conditional trivariate PDF. The thick colored line centered in **c** depicts the expected value of the trivariate distribution. For the points, the closed contours, and the mean line, colors correspond to the phase of ENSO, cool colors (low values of MEI) representing La Niña conditions and warm colors (high values of MEI) representing El Niño conditions. **a** The conditional marginal distribution of precipitation colored by the corresponding to the MEI value or ENSO phase. The black PDF shows the stationary distribution for twentieth century precipitation. **b** As in **a**, but for conditional PDFs and percentiles for temperature. **d**, **e** The precipitation (temperature) cPDFs corresponding to the 10th and 90th percentile values of the MEI index. Shading denotes the 5th and 95th percentiles of the bootstrapped cPDFs. Lines/regions drawn as dashes represent statistical insignificance at the 0.05 level. Lines/regions drawn as solid represent statistical significance at the 0.05 level. The vertical lines represent the expected value (mean) of the respective distributions where the shading indicates the 5th/95th percentiles of the expected values of the bootstrapped cPDFs. **f**–**j** As in **a**–**e**, but for temperature and precipitation data corresponding California climate division 6

oscillation, which transitions between its warm/positive phase known as El Niño and its cool/negative phase known as La Niña. ENSO is known to affect global weather and climate on the seasonal to inter-annual timescales (Gershunov and Barnett 1998) and it has the ability to impact remote locations, such as California via teleconnections (Cayan et al. 1999). Cayan et al. (1999) considered median and 90th percentile precipitation, and showed increases in both percentiles for the El Niño phase over the southern half of California and no change for both percentiles over the northern portion of the state. Here, we consider the joint distribution of California wintertime temperature and precipitation using ENSO as a continuous conditioning variable. This methodology allows us to calculate the joint and marginal

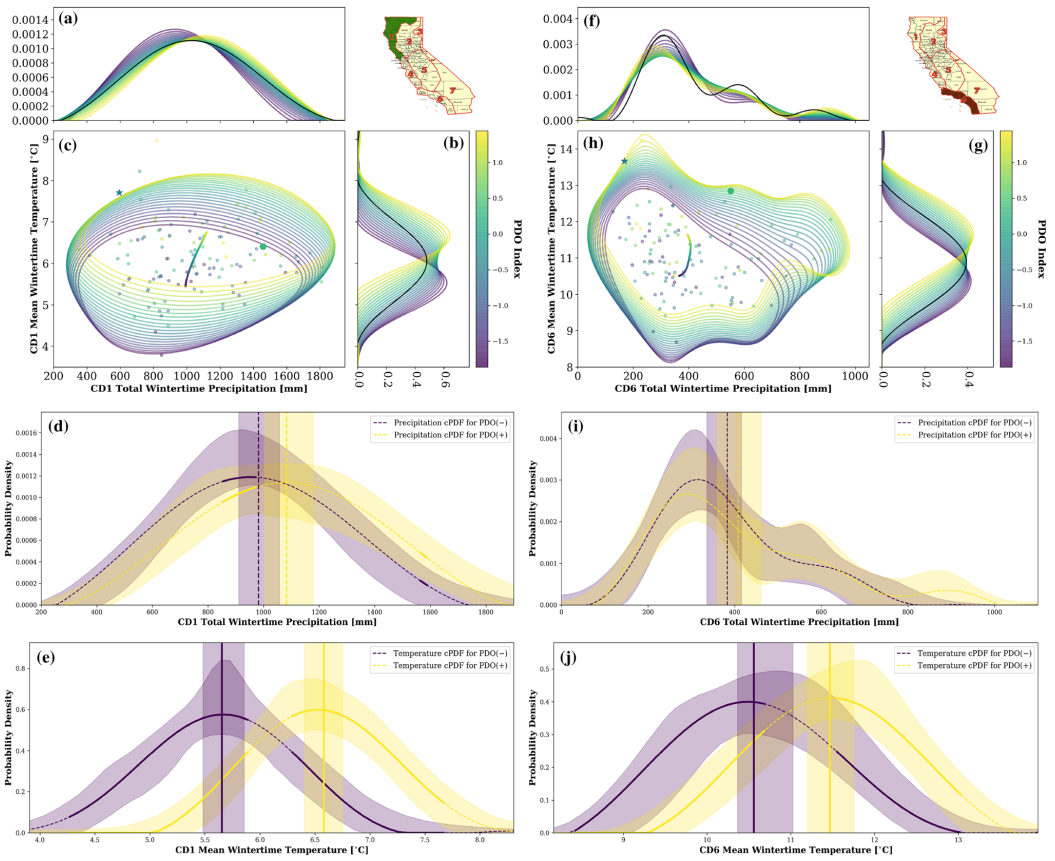

Fig. 2 As in Fig. 1, however all distributions are conditional on the phase of the PDO. The coloring in all panels here represents the phase of the PDO where cool colors represent the negative (cool) phase and warm color represent the positive (warm) PDO phase

conditional distributions as a function of ENSO phase and strength thus controlling for the non-stationarity in the data introduced by ENSO forcing. Further, we break the temperature and precipitation data down by climate division to illustrate the regional differences ENSO has on joint temperature and precipitation relationships. Figure 1c, h show the cPDFs of wintertime temperature and precipitation for Climate Division 1 (CD1) and Climate division 6 (CD6) as a function of ENSO phase and strength as monitored by the MEI. Central to those panels are color coded hoops representing the 95th percentile of the trivariate conditional distributions. Each of the hoops correspond to the contour of constant probability containing 95% of the cPDF. Near the center of each panel is a single continuous curve, which tracks the expected value of each joint cPDF. Underlying the closed contours of constant probability, are the precipitation and temperature data as a scatter plot along the horizontal axis and vertical axis respectively and are the data that went into the cPDF estimation. In Fig. 1a, the conditional marginal precipitation density estimates are shown (i.e. estimates of the precipitation PDF as a function of ENSO), likewise, panel b shows the conditional marginal temperature density estimates. In both panels a and b, the cPDFs drawn in black represent the twentieth century distributions for each variable. In all panels the color of each density estimate and all data indicate the value of the MEI index on which the PDF was conditioned. The colors of the cPDFs track the phase of ENSO ranging from negative values (cool colors) representing La Nina conditions to positive values (warm colors) representing El Niño conditions.

Figure 1 shows the striking difference of how ENSO affects these two geographically distinct climate divisions.

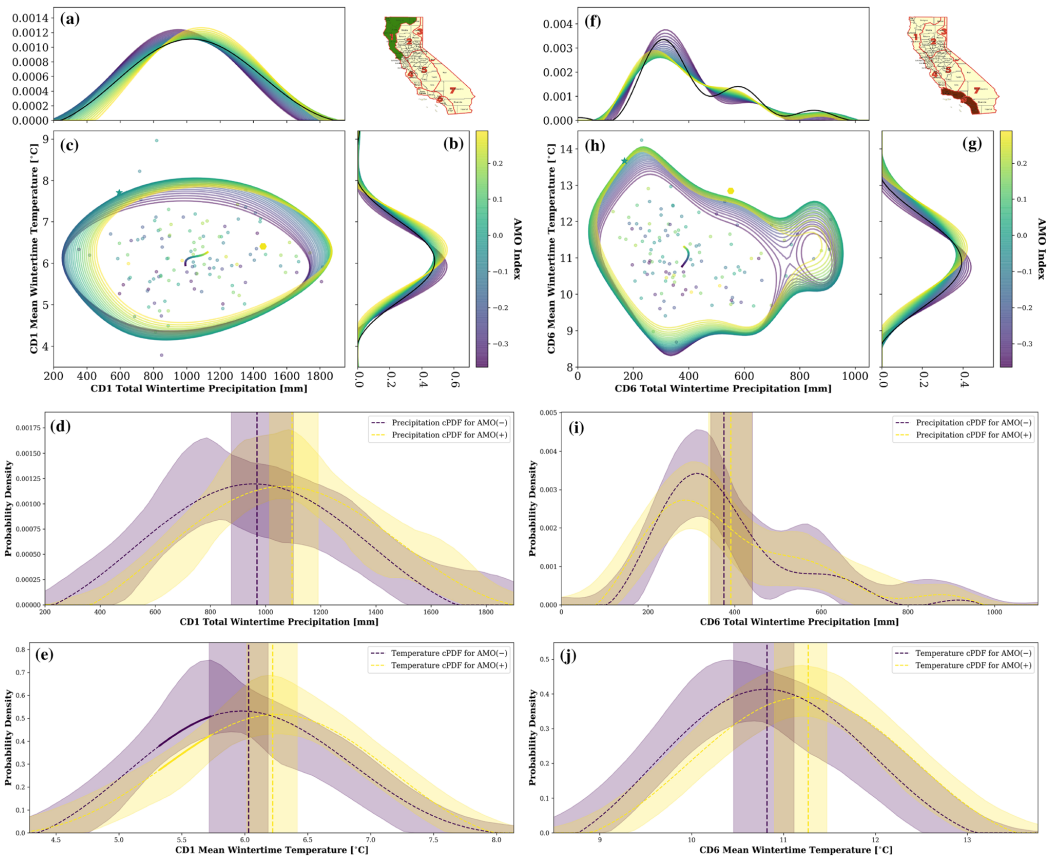

Fig. 3 As in Fig. 1, however all distributions are conditional on the phase of the AMO. The coloring in all panels here represents the phase of the AMO where cool colors represent the negative (cool) phase and warm color represent the positive (warm) AMO phase

In both CD1 and CD6, the multivariate relationship between ENSO and winter temperature and precipitation is non-linear as seen in Fig. 1c, h by the multivariate conditional mean line drawn at the center of each panel. Despite many studies using linear techniques to describe ENSO and its teleconnections, the non-linearity observed here is expected due ENSO's linkages to tropical deep convection, which has been documented in previous studies (Hoerling et al. 1997; Livezey et al. 1997; Gershunov 1998; Williams and Patricola 2018). Both CD1 and CD6 show an increase in temperature during the El Niño phase, statistically significant at the 0.05 confidence level. However, interestingly, CD1 experiences a slightly larger temperature increase than CD6 while also developing a strong left (cool/low-temp) skew during El Niño as seen in Fig. 1b, e. This means that while the majority of strong El Niño events result in very warm winters in northern California, there is also a substantial probability of experiencing very cold winters in northern California during strong El Niño events. This El Niño cold tail temperature skew is also observed at the daily timescale for the DJF period whereby the mean tends to warmer relative to La Niña, but with cold tail probabilities that rival those associated with La Niña (Guirguis et al. 2015). In addition to interpreting the mean of the bivariate distributions and the marginal distributions, additional information can be gleaned from the contours of the conditional bivariate distributions in panels c and h. The orientations of the conditional contours indicate the primary axes of variability associated with the respective phases of ENSO. For example, the major axis of the La Niña conditional closed contours (purple contours) for CD6 (panel h) shows a primarily negative orientation indicating that during La Niña, temperature

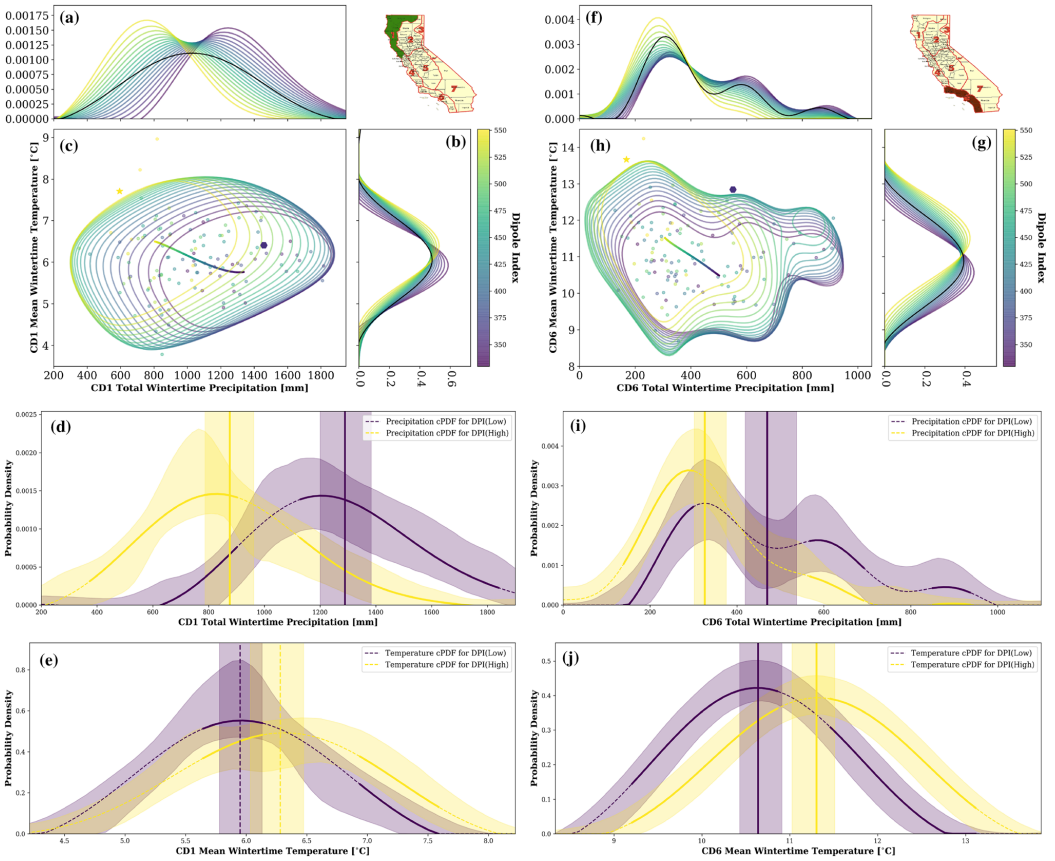

Fig. 4 As in Fig. 1, however all distributions are conditional on the strength of the dipole index. In all panels, the coloring corresponds to the strength of the dipole index where cool colors represent a weak dipole and warm colors represent a strong dipole, i.e. strong ridging in the western U.S. with a deep trough present over the eastern U.S.

and precipitation tend to be negatively correlated. However, the orientation of the major axis of the El Niño conditional closed contours (yellow contours) has shifted and is nearly horizontal, indicating that in general winter temperature and precipitation are not highly correlated during El Niño events. However, the outermost El Niño contour shows an inflated lobe in the upper left corner (panel h) indicating the occurrence of a winter characterized by a strong El Niño with high temperatures but anomalously low precipitation. That winter, indicated by the bright yellow dot in the upper left hand region of panel h is the winter of 2015–2016, in which the canonically strong El Ni no event failed to deliver even average precipitation to Southern California (L'Heureux et al. 2017). With the exception of 2015–2016 winter, the conditional El Niño contours show a positively sloping major axis indicating that overall, during El Niño events, winter temperature and precipitation are positively correlated.

With respect to wintertime precipitation, CD6 shows a large and statistically significant increase during the warm El Niño phase while CD1 shows only a modest, not statistically significant, increase, and only for the very strongest El Niño events. Moreover, the increases in mean precipitation for both CD1 and CD6 are occurring for very different reasons: CD1 experiences an increase in the mean due to a mode shift in the distribution while CD6 experiences an increase in the mean due to a disproportionate increase in the tail probabilities for experiencing extremely wet winters. The respective shape changes to the distributions are important observations as the societal and environmental risks and impacts from a disproportionate increase in the

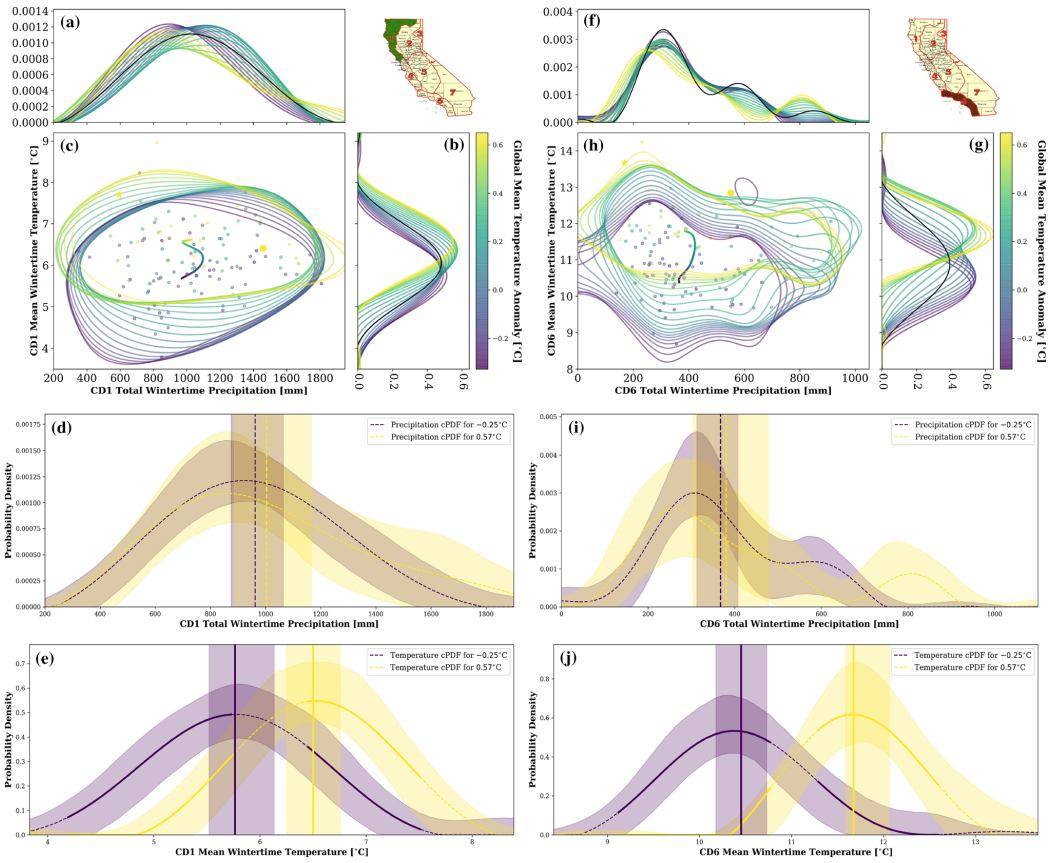

Fig. 5 As in Fig. 1, however all distributions are conditional on the global mean temperature anomaly

probability for extremes is not the same as an increase in the mean due to a uniform shifting of all probabilities. In other words, from a societal or environmental impacts perspective, not all shifts in the mean are created equal. Further, the respective changes to the precipitation distributions may happen for different physical reasons. In CD6, it has been shown that increases in the mean during the warm ENSO phase result from an increase in the daily rainfall rate (Feldl and Roe 2011; Gershunov 1998); however, this may not account for total shift in the mean due to the disproportionate increase in the tail probabilities at seasonal timescales. Similarly, what is the physical mechanism for the mode shift in precipitation as observed in CD1? The physical drivers of these changes will be explored in a future manuscript.

Comparing the precipitation marginals of CD1 and CD6 (Fig. 1a, f), qualitatively, the tails of the CD1 cPDFs are smooth and uniform while those of CD6 have an undulating character to them. This is something that can be noticed associated with the CD6 precipitation marginals throughout and is primarily due to two factors. (1) The precipitation variability in CD6 is inherently larger than in CD1, thus the estimates of the tails are less well-constrained/resolved for the equivalent number of samples. And (2), the underlying mechanics of the kernel density estimation method, fastKDE, rely on a Fourier transform of the data whereby the tails of kernels associated with data that are sparse (i.e. extreme values) can constructively interfere leading to undulations in those regions. The bootstrap error analysis we use, described in the methods section, is designed to quantify the uncertainty in the PDF associated with this phenomenon. By definition, every sample is included in the estimate of the cPDFs, however, the amount each sample contributes to the cPDF estimate is determined by the width of the optimally

calculated kernel associated with the conditioning variable, here the ENSO index MEI. Specifically, the kernel used here has a width of approximately 3.5 MEI units, which spans a large portion of the data having a range of 4.5 MEI units. This means for the max MEI value of 2.7, the kernels associated with data less than MEI $\approx 1.0\,(2.7 - 3.5/2)$ do not contribute much to the density at the max MEI value. This implies that at the max MEI value of 2.7, approximately only 20 data points are actively contributing to the density there. This example illustrates why we chose to use P10/90 values for our end-member analyses rather than min/max values, as we increase the number of kernels contributing to our estimates to approximately 90, which greatly increases the number of samples that inform our estimates. See O'Brien et al. (2016) for further details.

The starred and hexagon points mark 2014 and 2017 respectively. The coloring of both points indicate that both the very dry winter of 2014 and the very wet winter of 2017 occurred during ENSO neutral conditions, highlighting the substantial variability in winter precipitation in California not explained by ENSO. In fact, our results show that statewide, El Niño increases the expected (mean) precipitation from 486 to 520 mm, making the El Niño phase of ENSO only responsible for a modest 7% increase the expected statewide winter precipitation. This result is consistent with the satellite-based findings of Savtchenko et al. (2015). In addition, California obtains roughly 60% of its freshwater resources from snow melt runoff (Lauer 2011) and CD1 is home to the Salmon–Klamath–Trinity mountains, the primary snow melt source for Shasta and Trinity lakes, the second and third largest reservoirs, respectively, in northern California. As seen in Fig. 1a, CD1 experiences roughly the same wintertime precipitation regardless of ENSO phase; however, winter temperatures are much cooler during the La Niña phase, likely resulting in deeper snow packs, a lower snow line, and a delayed spring melt, thereby contributing to a more reliable water source for the dry summer months to follow. Thus for northern California, contrary to popular belief, from a water security and reliability perspective, La Niña winters may in fact actually be preferable.

3.2 The PDO conditional distributions

The Pacific Decadal Oscillation is a low frequency north Pacific ocean sea surface temperature pattern first described by Mantua et al. (1997). ENSO and PDO are not independent and recently it has become apparent that PDO may be directly forced by ENSO forcing (Newman et al. 2016). However, in terms of their respective effects on the climate system, specifically precipitation and temperature patterns, they each have unique and distinct effects (DeFlorio et al. 2013), despite their broadly similar SST patterns (see Figs. S1, S3). While ENSO has a direct physical causal pathway for affecting the climate system, the causal physical mechanisms by which the PDO affects temperature and precipitation patterns is less clear (Pierce 2002). However, more recently Meehl and Hu (2006) found that wind anomalies forced ocean Rossby waves, which sets the PDO decadal timescale, and are themselves linked to anomalous mid-latitude atmospheric circulations which in turn drive precipitation anomalies. Figure 2 shows the conditional distributions of temperature and precipitation as a continuous function of the PDO phase and strength. As with the ENSO distribution shown in Fig. 1, non-stationarity introduced into the data by PDO forcing is evident. With respect to the precipitation marginal distribution the overall effect of PDO (Fig. 2a) is larger than that of ENSO in northern California; however, the shift in the mean is still statistically insignificant at the 0.05 confidence level (Fig. 2a). In CD6 the contrast between the effects of PDO and ENSO are more stark. While ENSO results in a strong and statistically significant increase in mean precipitation resulting from an increased probability for experiencing extreme wet winters, the effects of PDO in CD6 shows a nonlinear, but ultimately zero correlation to changes in wintertime precipitation. This is not true for temperature. Both CD1 and CD6 show large, uniform, and statistically significant increases in wintertime temperature. For CD1 during the cool PDO phase, the probability of exceeding the 90th percentile of twentieth century temperature is near zero ($P \approx 0.01$) while during the warm phase that probability is over 20 times greater ($P \approx 0.2$). Correspondingly, the return period for experiencing very warm wintertime temperatures exceeding the 90th percentile decreases from a 1-in-100 year event during the cool phase to a 1-in-5 year event during the warm PDO phase. It should be noted however, that the PDO is not the only physical mechanism by which the return periods of temperature and precipitation are affected. The effect shown in Fig. 2 is the role PDO plays in affecting those statistics. The case is similar for CD6 though slightly less pronounced. The many implications for these changes in wintertime temperatures as a function of the PDO phase. During the positive phase of the PDO, elevated wintertime temperatures increase the snow line elevation, can produce more rain-on-snow events, decrease snow pack, and alter the peak runoff timing, all of which have a large impact on California's water supply (McCabe and Dettinger 2002). Given the slow evolution of the PDO, the results here could provide a measure of predictability for inter-decadal precipitation and temperature forecasts for state water managers to better manage water supplies. However, interdecadal and seasonal variability may be the dominate control for extreme years as for both the very dry and warm winter of 2014 and the very wet winter of 2017, PDO was in near neutral conditions and consequently, likely did not play a major role in driving those extreme conditions. We note however, that the PDO may not

be an independent mode of SST variability, but more a result of an integration of several modes of variability occurring across a range of temporal and spatial scales (Newman et al. 2016). Newman et al. (2016) show the PDO to likely be a result of ocean memory i.e. re-emergence, tropical forcing from ENSO, and the Aleutian Low, which were shown using lagged correlations to lead the PDO. Given that ENSO conditions were in near neutral conditions during the 2014/2017 extreme years, perhaps the Aleutian low, taken as a primary driver of PDO variability, could have played a larger role in driving those extreme years. To consider this possibility, we used the North Pacific Index (NPI) (Trenberth and Hurrell 1994), an often employed index to characterize the strength of the Aleutian low, as a conditioning variable for the temperature and precipitation distributions. The results indicate (figure not shown) that, as with ENSO, the Aleutian low was in near neutral conditions and as such, is not a likely driver for the extreme years of 2014/2017.

3.3 The AMO conditional distributions

The Atlantic Multidecadal Oscillation is a long-term warming and cooling of North Atlantic sea surface temperatures with a period of 60–70 years (Schlesinger and Ramankutty 1994; Kerr 2000). The warm phase of the AMO has been previously connected to increased drought conditions over the central U.S., increased rainfall in Florida, and a low-frequency modulation of ENSO (Enfield et al. 2001). Of interest here is what effect the AMO has on the multivariate statistics of wintertime temperature and precipitation in California. Mestas-Nuñez and Enfield (1999) showed that the AMO was inextricably linked to a warming of the North Pacific through an atmospheric bridge involving the Arctic Oscillation. Thus one plausible physical mechanism for the AMO to affect west coast weather statistics would be the warming of north Pacific acting as an enhanced moisture source for west coast storms thereby affecting the precipitation distribution and in turn the multivariate statistics. Also of interest, the composite SST pattern which captures AMO values at or exceeding the 90th percentile also shows a strong ENSO signal in the eastern Pacific. This appears to be driven primarily by the years 1998 and 2016 when both ENSO and AMO exceeded their respective 90th percentile thresholds (Fig. S5). Figure 3 shows the multivariate distributions of California CD1 and CD6 temperature and precipitation as a function of the AMO phase and strength. Northern California's relationship with AMO is positive in both temperature and precipitation and close to linear in both variables. However, in southern California while temperature increases monotonically with AMO phase, precipitation increases linearly from cool to neutral conditions but then the relationship reverses and decreases linearly from neutral to warm AMO conditions. The behavior of the multivariate relationships may indeed be real (Fig. 3c, h); however, it is difficult to assert conclusively as the mean changes between the cool and warm phases of the AMO are not statistically at the 0.05 confidence level (Fig. 3d, e, i, j). California, taken as a whole (Fig. S6), shows a multivariate relationship with AMO more similar in character to how CD1 behaves. While there is slightly more non-linearity in the relationship, both temperature and precipitation increase monotonically as AMO transitions from its cool phase to its warm phase. However, again like both CD1 and CD6, the relationships between California temperature and precipitation are not significant at the 0.05 confidence level, suggesting that the AMO does not have an appreciable direct effect on California's temperature and precipitation statistics. However, as described in previous literature (e.g. Levine et al. 2017a; Kang et al. 2014), the AMO may exert an indirect effect on California temperature and precipitation via the low-frequency modulation of ENSO variability and strength. In both the aforementioned studies, the AMO tended to suppress both ENSO variability and strength.

3.4 The DPI conditional distributions

The Dipole Index (DPI) described by Wang et al. (2014), characterizes a state of the atmosphere whereby, when in the positive phase, a persistent, quasi-stationary pattern produces deep troughing in the eastern U.S. and strong ridging over the western U.S. and eastern Pacific, which reverses in the negative phase (Wang et al. 2017, Fig. S7). During the winter of 2013–2014, the positive phase of this index reached an all-time high and resulted in record setting cold snaps in the Eastern U.S., while the U.S. west coast was simultaneously gripped by record setting drought conditions (Swain et al. 2014; Wolter et al. 2015). As in the previous plots, Fig. 4 shows the multivariate relationships of CD1 and CD6 temperature and precipitation. Most evident here is how highly non-stationary the data are as a function of the DPI. Panels a and c show a strong precipitation response to the DPI, whereby the expected value of precipitation for CD1 decreases from 1342 mm during the negative phase of the DPI to 801 mm during the positive phase of the DPI representing a drop of ~40%. The change in mean expected precipitation between the two phases of the DPI is achieved through a uniform shifting of all probabilities as shown in Fig. 4a. Collectively the DPI explains ~50% of the wintertime precipitation variance for CD1 and statewide and ~36% for CD6, far greater than any other large-scale index we considered. The high explanatory power of the DPI makes it an obvious candidate to explore as a predictor variable. However, we refrain from assessing the potential predictability of the DPI and reserve that analysis for a future manuscript. Interestingly, for CD1 wintertime temperature, the strong ridging does not produce a statistically significant increase

in temperature as one might expect (Fig. 4e). For the very wet winter of 2017 Fig. 6 shows CD1 received 1458 mm of precipitation, which is a ~P90 event with respect to the 20th century distribution. However, when taking the 2017 DPI value of 360 into account, with respect to the conditional distribution at that DPI level, the winter of 2017 was only a ~P75 event. In other words, the anomalous winter of 2017 was much more likely when considering the probability of occurrence with respect to the DPI conditional distributions. This suggests that there is a level of probabilistic predictability to the outcome of any given winter in California when monitoring/forecasting the state of the dipole circulation. Similarly, during the drought winter of 2014 CD1 received only 594 mm of precipitation, which is 56% of normal or equivalently a 8th percentile event. However, if one was to consider this event from the perspective of the corresponding conditional DPI distribution then the anomalous dry winter of 2014 is a 20th percentile event. So when considering the winter of 2014 with respect to a cPDF which takes into account the atmospheric circulation features present, what was an extreme event becomes more likely and thus more predictable. Taken together, Fig. 6 shows the how dramatically the probabilities change for experiencing either drought or deluge depending on the strength of the DPI.

Southern California, CD6, shows a similar strong and statistically significant ($p \leq 0.1$) precipitation response to changing of phases of the DPI. During the negative phase of the DPI, the mean expected wintertime precipitation is 475 mm, while during the positive phase its only 290 mm. For CD6 the winter of 2017 resulted in 551 mm of precipitation. Shown in Fig. 4g, i, the probability of experiencing a winter of this magnitude or larger during the positive phase of the DPI is 0.014. However, during the negative phase of the DPI that probability increases to 0.36, representing an increase by a factor of 26. Correspondingly, the return period for experiencing the winter of 2017 during the positive phase of the DPI is a 1-in-70 year event while during the negative phase its a 1-in-3 year event. Unlike CD1, CD6 experiences a statistically significant ($p \leq 0.1$, significance test described in the "Methods" section) increase in temperature transitioning from the negative to the positive phase of the DPI.

Statewide, DPI causes California to experience statistically significant shifts in both mean wintertime temperature

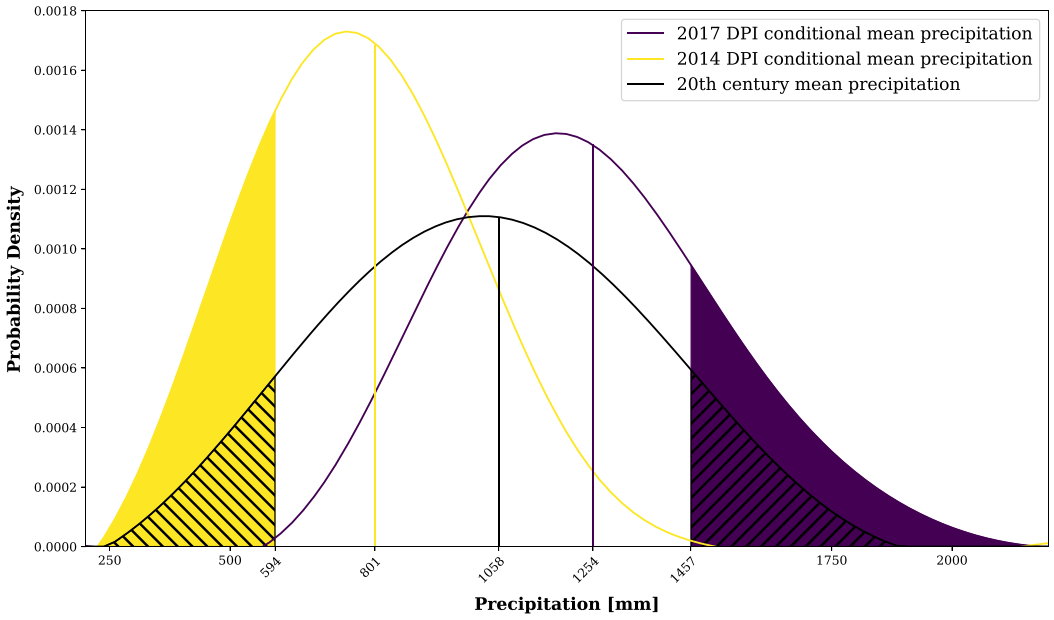

Fig. 6 The conditional probability distribution functions (cPDF) for CD1 DPI corresponding to 2014 in yellow, 2017 in purple, and the full distribution of 20th century winter precipitation in black. The vertical lines in the corresponding colors represent the expected values of those distributions respectively. The region shaded in yellow represents the probability of getting a year as dry or dryer than 2014 according to the 2014 DPI cPDF. The purple shaded region represents the probability of getting a year as wet or wetter than 2017 according to the 2017 DPI cPDF. The hashed regions represent what those same probabilities would be if estimating them from the full PDF of twentieth century precipitation

and precipitation (Fig. S8). While the twentieth century mean precipitation is 486 mm, during the positive phase of the DPI that decreases to 362 mm while during the negative phase it increases to 589 mm. The drought winter of 2014, statewide California received 262 mm of precipitation, which ranks as the sixth driest winter on record. With respect to the twentieth century distribution, this level of winter precipitation or lower only has a ~ 0.06 probability of occurrence. However, when taking in to account the corresponding DPI level, the probability of experiencing a winter that dry increases by over a factor of 2 ($P \approx 0.13$). Similarly for the wet winter of 2017, statewide California received 744 mm of rain, making it the 7th wettest winter statewide. The probability of experiencing a winter this wet or wetter with respect to the twentieth century distribution is ~ 0.07. However, taking into account the corresponding DPI index, that probability also increases by over a factor of 2.

3.5 The GMTA conditional distributions

One of the most prominent changes to the global climate from the early twentieth century to present is that of anthropogenically forced temperature rise (Intergovernmental Panel on Climate Change 2014). From the late 1800's to present the earth has experienced nearly a 1 °C rise in average temperature (Team 2018), (Fig. S9). Figure 5 shows the conditional multivariate distributions of wintertime temperature and precipitation as a function of the global mean temperature anomaly (GMTA) for CD1 and CD6. Cool colors represent periods with low GMTA occurring primarily in the late 19th century and early twentieth century. While warm colors represent periods with high GMTA occurring almost exclusively in the early twenty-first century. Not surprisingly, the relationship between global mean temperature and regional temperature in both climate divisions is positive and both exhibit statistically significant shifts. However, its notable that CD6 has experienced roughly twice the increase in wintertime regional temperatures as CD1 has for the same amount of global mean temperature rise as seen in Fig. 5e, j. This is also true of the JJA period (figure not shown) and therefore carries with it a significant increased risk for heat-related health issues in CD6 that is not present in CD1, which contains a large portion of California's population. This highlights a critical aspect of climate change: the risks and negative impacts from a changing climate are not distributed evenly, globally, as well as regions as geographically limited as California. We hypothesize that the differential warming rates in CD6 versus CD1, as a function of global mean temperature rise, is driven by the urban heat island effect, as CD1 is primarily densely forested temperate rain forest, while CD6 is primarily an urbanized semi-arid Mediterranean environment. Exploring this hypothesis however is beyond the scope of this manuscript. Similarly, statewide, California has experienced a statistically significant increase in wintertime temperatures as a function of global mean temperature rise (Fig. S10). This increase in wintertime temperatures over the last century has significant consequences for California ranging from an earlier spring, shorter warmer winters, decreased snow pack to the disruption of ecological niches to sensitive native and endemic plants and animals (Stewart et al. 2005; Mote et al. 2005; Parmesan 2006). Another notable feature of Fig. 5e, j as well is an apparent reduction of wintertime temperature variance indicated by the contraction of the cPDFs transitioning from an early century cool climate to our present relatively warm climate. We tested whether the variance reduction was statistically significant and in this framework, it was not. However, that said, the effect may be real as several studies have documented and predict a decrease in wintertime mid-latitude temperature variance with warming (Rhines et al. 2017; Holmes et al. 2016).

The dominant mode of historical natural variability is within the precipitation dimension. However, the conditional climate change signal in all cases is approximately orthogonal to the axis of natural variability (Fig 5c, h). Mahony and Cannon (2018) identified this behavior, departure intensification, in projections of future climate in CMIP5 models analyzing the climate change behavior of summertime temperature and precipitation. The univariate relationship between global mean temperature and precipitation is much more complicated than temperature and highly non-linear. Both CD1 and CD6 wintertime precipitation show a positive relationship with the GMTA early in the century. That is, early in the record both climate divisions trend toward warmer wetter winters. However, mid-century at a GMTA of ~ 0.15 °C, the relationship reverses such that warmer winters become increasingly associated with drier winters. This is also true of California precipitation state wide. The combination of decreasing wintertime precipitation and warmer winter temperatures represents two trends which exacerbate each other whereby California receives less precipitation that falls as snow and snow that melts more quickly, ultimately having a large effect on California's summertime water supply (Knowles et al. 2006; Cayan et al. 2001). Moreover, monotonically increasing wintertime temperatures increase summertime wildfire risks in a commensurate fashion (Yoon et al. 2015). This, combined with negative precipitation anomalies greatly exacerbates wildfire risk. To this point, in January 2018 the Thomas fire became the largest fire in California history burning nearly 300,000 acres causing nearly two billion dollars in damages (Cal Fire 2018b; Ding 2018). In the October–December period of 2017 preceding the Thomas fire, CD6 experienced its second lowest precipitation anomaly and highest temperature anomaly for that period, the co-occurrence of which, was likely at the root of the intensity of that fire. As a side-note, at the time of

this writing, the Ranch fire (Mendocino complex) has now become the largest fire in state history charing over 450,000 acres of land (Cal Fire 2018a).

4 Discussion

We have applied the novel kernel density estimation method of O'Brien et al. (2014) to characterize the multivariate behavior of wintertime temperature and precipitation in California as a function of selected large-scale modes of climate variability. This methodology allows us to investigate the impacts and contributions of various large-scale climate conditions to altering the probabilities of co-occurring extremes as continuous variables as opposed to simple "on/off switches". This is an important advancement in the understanding of how large-scale climate modes affect variability in temperature and precipitation and their joint behavior, as it is demonstrated that relationships observed are often non-linear and therefore cannot be well-described by linear correlation analysis typically employed in this area of climate research. Further, this methodology allows us to account for non-stationarity in the data regardless of what time scale that non-stationarity occurs on. For example, the PDO introduces non-stationarity into the data on the decadal timescale while ENSO introduces non-stationarity on the inter-annual timescale. Being able to account for this non-stationarity allows for a more robust and nuanced estimate of how the univariate and multivariate statistics vary as a function of each index.

Overall the relationships between ENSO and winter temperature and precipitation are non-linear, stronger in the southern California than in northern California, and statewide, only explain about 7% of the precipitation variance. Both CD1 and CD6 experience statistically significant increases in winter temperature during El Niño. However, the utility of this method demonstrates that, while the increases in mean temperature are roughly equal in CD1 and CD6, the full distributions themselves look very different. CD1 has a strong left (cool) skew that is not present in CD6 indicating that in CD1, some strong El Niño winters can be quite cold relative to the mean during that phase. The worst drought conditions in California occur when negative precipitation anomalies co-occur with positive temperature anomalies as happened in 2014. California winter temperature and precipitation, regionally and statewide, show an overall positive relationship with ENSO indicating that co-occurring extremes for drought conditions are not favored by this teleconnection. In general with ENSO, California winters are either wet and warm (El Niño) or cool and dry (La Niña). To verify that the MEI was accurately capturing ENSO's teleconnection with California, we repeated the analysis with the commonly used Niño3.4 index (Rayner 2003). Not surprisingly, the relationships were nearly identical save for small variations in the shape of the multivariate distributions (figure not shown). Finally it is known that there are different flavors of ENSO, the most commonly known of which is the Modoki (Capotondi et al. 2015). To consider how this variation of El Niño differs in its teleconnection to California winter temperature and precipitation relative to its standard counterpart described by the MEI, we used the monthly Modoki index from JAMSTEC and repeated the analysis (Ashok et al. 2007; JAMSTEC 2018). Despite having a distinct spatial SST pattern, we find that overall, in CD1, CD6, and statewide, the Modoki teleconnection to temperature and precipitation exhibits very similar behavior to the standard El Niño.

Of the decadal-scale teleconnections, PDO has the greatest effect on California temperature and precipitation statistics. Although statewide, PDO is correlated with increased precipitation, which is primarily driven by regional correlations in northern California, no relationships statewide or regional are statistically significant at the 0.05 level. However, PDO may exert other effects on precipitation not reflected in Fig. 2 through its connection with ENSO. As shown by Newman et al. (2016) and by Fig. S11, PDO and ENSO are not independent. When PDO is in its warm phase, ENSO tends to sit at a higher background state, enhancing El Niños and suppressing La Niñas. The converse is also true, when PDO is in its cool phase, El Niños are suppressed and La Niñas enhanced. In addition, ENSO–PDO interactions are further documented by Gershunov and Barnett (1998) who showed that ENSO teleconnections to North American Climate via heavy daily precipitation frequency are also sensitive to the PDO phase. Statewide, and in both CD1 and CD6, PDO does exert a statistically significant effect on temperature raising expected mean statewide, CD1, and CD6 temperature by approximately 0.7 °C, 1 °C, and 0.5 °C respectively during its positive warm phase. However, despite these increases in temperature, evidence seems to suggest that it is suppressed precipitation during the PDO cool phase that drives drought in the west (Meehl and Hu 2006; Cook et al. 2016). Less important for California climate is the AMO, which showed no statistically significant relationships to either temperature or precipitation. However, again like PDO, AMO may effect precipitation in California by modulation of ENSO teleconnections as there is some evidence to suggest that AMO tends to suppress ENSO variability and strength (Levine et al. 2017b; Kang et al. 2014).

Of all of the indices we studied, the DPI has the largest control over precipitation in California explaining ~ 50% of the variance statewide and in CD1 and ~ 36% in CD6. In addition, the DPI is the only index to show a positive correlation with temperature and a negative correlation with precipitation, thus making it the only large-scale index to increase the risk of experiencing co-occurring extremes in

both suppressed precipitation and elevated temperatures, which together exacerbate drought conditions. Given that the DPI explains such a large fraction of the variance in California precipitation, it presents an opportunity to use the index and the associated conditional probability distributions shown in Fig. 6, as a tool for water supply forecasting and reservoir management. For example, reservoirs in California operate based on rule curves, which specify storage targets that provide a flood management pool in the winter months to accommodate increased inflow while increasing storage during the summer months to provide additional water supply during the summer months when the risk of high impact storms is virtually non-existent. These rule curves are derived from historical observations and risk analysis (Brekke et al. 2009). Recently, the idea of forecast informed reservoir operations (FIRO) has gained increased attention as a potential alternative to rule curves to provide additional water storage without diminishing the flood control capability the reservoirs provide (Jasperse et al. 2017). Leveraging the the cDPI distribution to provide longer range probability estimates of precipitation along with shorter range numerical weather prediction could further enhance reservoir operations for more efficient use of California's water supply.

Figures 4 and 6 demonstrate the strong control the dipole circulation pattern has on California temperature and precipitation through statistical characterization. However, the physical processes which underlie and drive such changes to the respective conditional probability distributions are not uncovered by such analyses. To that end, Fig. 7 demonstrates the connection between the large-scale dipole circulation pattern and integrated vapor transport (IVT), which is strongly correlated with precipitation (Neiman et al. 2009; Rutz et al. 2014), and temperature anomalies at the seasonal timescale. Figure 7a shows the negative phase of the dipole pattern as indicated by the P10 DPI index relative to NDJFMA climatology. Panel a shows an enlarged and deepened Northeast Pacific trough with strengthened cyclonic flow that enhances and directs moisture transport to the Western U.S. via an Eastward extension of the storm track centered around 40°N. Comparatively, panel c shows the positive phase of the dipole circulation (P90 years) the pattern is reversed, and the associated ridging and anticyclonic flow weakens the Pacific storm track and results in its termination over the Eastern Pacific before it reaches the U.S West coast resulting in reduced winter precipitation. The temperature signal for the negative and positive phases of the dipole circulation shown in panels b and d respectively are quite

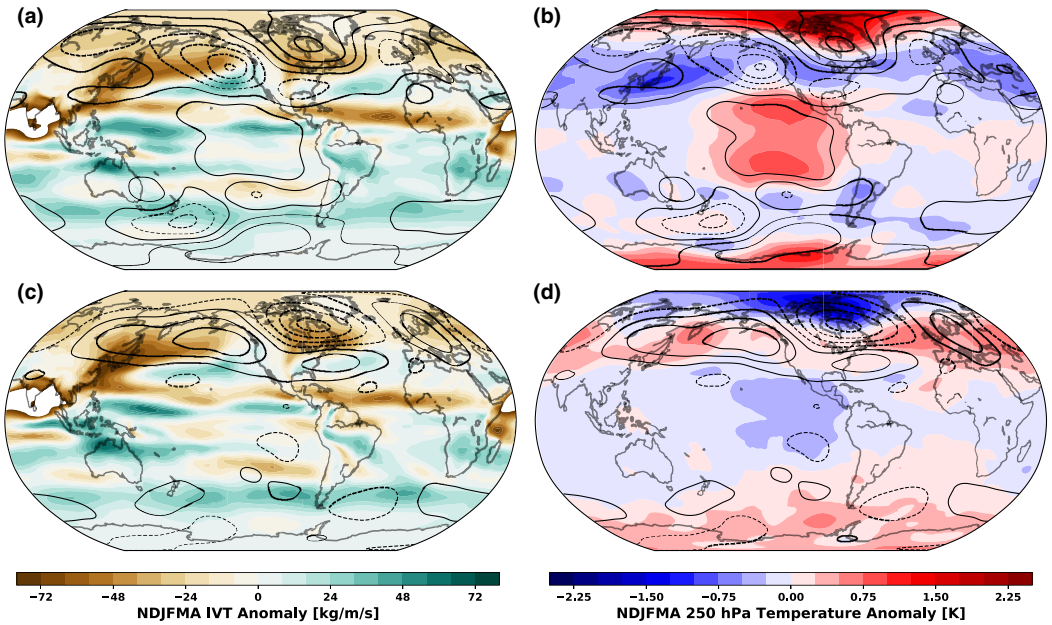

Fig. 7 Wintertime (NDJFMA) integrated vapor transport (IVT) and 250 hPa temperature anomalies relative to twentieth century climatology for DPI P10 years (**a**, **b**) and DPI P90 years (**c**, **d**). All four panels have the corresponding 250 hPa geopotential height anomalies overlaid as contours drawn in black with dashed/solid contours indicating negative/positive anomalies with contour interval of 15 m

distinct. The negative/positive phase show confined narrow bands of circumglobal midlatitude cooling/warming. These features are suggestive signatures of jet acting as waveguides for the propagation of Rossby waves as described in Branstator et al. (2017). Taken together, Fig. 7c, d show how the positive phase of the dipole circulation results in the simultaneous occurrence of both reduced rainfall and increased temperatures during the boreal winter, the combination of which, can result in greatly exacerbated drought risk. While Fig. 4e indicates that the warming experienced in CD1 is not statistically significant, Fig. 7d shows that during the positive (ridging) phase of the dipole circulation, the midlatitude warming signal is both robust and circumglobal. The lack of statistical significance in the warming signal for CD1 could result from a signal-to-noise issue. We also note that wintertime Northeast Pacific anticyclonic circulation has been shown to induce an anomalous cold northerly flow along the west coast of North America (Favre and Gershunov 2006), which would serve to dampen the warming response typically associated with anticyclones during the boreal summer.

The dipole index depicts the amplification and attenuation of the wintertime stationary waves, the dominate wither circulation feature over North America. As such it contains no intrinsic information about the generation of the circulation regime. The dipole pattern the DPI measures can arise from various mechanisms and was the focus of many different studies, particularly with respect to the North American winter of 2013/14. That winter was characterized by drought across the west and record snow and cold over much of the east (Palmer 2014). It was at this time the DPI hit its highest level. The mechanisms of the dipole circulation are rooted in mid-latitude atmospheric internal dynamics however, it can be enhanced by tropical diabatic heating of the atmosphere and the resulting Rossby wave that forms. Teng and Branstator (2017), who refer to the dipole pattern as a circumglobal Rossby wave of wavenumber 5, found that while tropical heating anomalies are not necessary for formation of the dipole pattern, they do double the chance of them forming. Seager et al. (2015) and Wang and Schubert (2014) came to similar conclusions finding that while SST anomalies can cause ridging over the west coast, the magnitude of the observed ridging in 2011–2014 is not explained by SST anomalies alone suggesting the role of internal atmospheric variability or other forcings constructively interfering in contributing to the extreme ridging. We find using the twentieth century reanalysis and NCEP/NCAR reanalysis that the wintertime DPI has been increasing by 0.6 m/year ($p < 0.001$) and 0.7 m/year ($p < 0.1$) respectively, while Wang et al. (2014) showed that the variance in DJF DPI has been increasing as well. Using different metrics, Singh et al. (2016) also observed an amplification of the dipole pattern. This suggests that this type of circulation pattern is become stronger with time and is switching polarities more intensely and frequently. Practically, inferring from the DPI cPDFs in Fig. 6, this means an increasing frequency of dramatic shifts between very dry winters and very wet winters. This increase in precipitation volatility was found in an analysis of CMIP5 models to result from an increased frequency in the number of dry days per year in conjunction with an increase in rainfall intensity on days it does rain, thereby increasing the seasonal-scale precipitation variability (Polade et al. 2014, 2017). More recently, in an analysis of the LENS RCP8.5 ensemble, Swain et al. (2018) found a twenty-first century increase in both wet and dry extremes which results in a 25–100% increase in dry-to-wet precipitation events with little change in the mean. Further, in that study it was shown that relative to the preindustrial control runs, the pressure anomalies driving both wet and dry years at the end of the twenty-first century were more extreme suggesting the DPI characterizing these anomalous features would be correspondingly more extreme as well. Similarly, Wang and Schubert (2014) found in an analysis of 12 AMIP model runs, the distribution of geopotential heights in the latter half of the century relative to the first increased suggesting an increase in blocking events. However, in this same study, the corresponding precipitation PDF remained unchanged suggesting the decrease in precipitation from storm occurrences due to blocking was offset by an increase in precipitable water following Clausius–Clapeyron. Despite model-based evidence suggesting an increase in the frequency and strength of geopotential height anomalies and blocking, robust observational evidence is lacking and/or mixed (Barnes 2013; Barnes et al. 2014; Francis and Vavrus 2015; Screen and Simmonds 2013). However, the extent to which anthropogenic forcing plays a role in generating extreme geopotential height (GPH) anomalies is less clear. Swain et al. (2014) show that the occurrence of extreme geopotential heights exceeding the 99th percentile of preindustrial control runs increases by up to 670% in twentieth century CMIP5 simulations including both natural and anthropogenic forcing, no increases in extreme heights were found in simulations including only natural forcing. Similarly Wang et al. (2014) found an increase in sliding variance of the DPI present both in the 20CR reanalysis and CESM1-GHG simulations, however this signal was not present in the CESM1-NAT simulations suggesting a anthropogenic component to the increase in frequency of dipole pattern occurrences. Additionally, Williams et al. (2015) found that while precipitation is the primary driver of drought variability, anthropogenic warming accounted for 8–27% of the observed drought in 2012–2014 and 5–18% in 2014. While the physical mechanisms of how climate change may alter the strength and/or frequency of the dipole pattern, both in its cyclonic and anticyclonic configurations, several potential pathways exist. Arctic warming (Francis and Vavrus 2015; Cohen et al. 2014), Pacific SST anomalies

(Seager and Henderson 2016; Watson et al. 2016; Swain et al. 2017), and sea-ice concentration and extent (Alexander et al. 2004; Sewall 2005), are all projected to change due to human activities over the twenty-first century and have roles in influencing mid-latitude weather patterns and large-scale circulations.

The Dipole circulation pattern is highly related to the Tropical/Northern Hemisphere (TNH) pattern (Mo and Livezey 1986). DJF correlations between the TNH and the DPI are extremely high with an r value of 0.87. The TNH is defined as the forth rotated EOF of 700 mb winter height anomalies and when correlated with rain gauge stations around the globe, finds its larges correlations with those stations in the maritime continent. This suggests that the TNH/DPI is likely related to convection generated gravity/Rossby waves originating in the warm-pool region. This would be consistent with the findings of Wang et al. (2014). Moreover, Mo and Livezey (1986) found that the TNH was associated with variability on timescales longer than a season, thus potentially partially explaining the extreme persistence of the ridge that formed over California during the winter of 2013/14.

Finally, we considered the effect the Arctic oscillation may have on the occurrence of joint extremes in California temperature and precipitation. Despite the attention the Arctic gets on modulating mid-latitude weather, when it comes to temperature and precipitation change in California, we obtained a null result (figure not shown). For CD1, CD6, and state wide averaged data, both temperature and precipitation showed little sensitivity to the phase of the Arctic oscillation.

5 Summary

We have implemented a novel, nonparametric conditional probability distribution method that allows evaluation of complex, multivariate, and nonlinear relationships that exist among temperature, precipitation, and various indicators of large-scale climate variability and change. We have shown that the multivariate statistics of temperature and precipitation are demonstrably non-stationary and therefore benefit from more sophisticated statistical techniques for accurate characterization. In addition, the multivariate variability and statistics of temperature and precipitation exhibit strong spatial variation across a region that is often treated as having homogeneous and stationary statistics (AghaKouchak et al. 2014). We find that inter annual-to-multi decadal modes of atmosphere-ocean variability in the Pacific and Atlantic explain modest amounts of variability in co-occurring extremes in California, at best. Despite the historic focus on ENSO as the main driver of precipitation variability in California, we find that ENSO only explains about 7% of the variability statewide. However, the dipole index, a measure of the strength and polarization of the mean-state circulation present over North America, accounts for a much larger fraction of precipitation variance, nearly 40% statewide. This suggests that a better understanding of the drivers and predictability of large-scale atmospheric variability is key to interannual—to decadal prediction of co-occurring hydroclimate extremes in the western U.S.

Acknowledgements The authors would like to thank three anonymous reviewers for their insightful and helpful comments that greatly improved the quality of this manuscript. This research was supported by the Director, Office of Science, Office of Biological and Environmental Research of the U.S. Department of Energy as part of their Regional and Global Climate Modeling Program (RGCM) under contract no. DE-AC02-05CH11231, and SYW is supported by DOE Grant DESC0016605.

References

AghaKouchak A, Cheng L, Mazdiyasni O, Farahmand A (2014) Global warming and changes in risk of concurrent climate extremes: Insights from the 2014 California drought. Geophys Res Lett 41(24):8847–8852. https://doi.org/10.1002/2014GL062308

Alexander MA, Bhatt US, Walsh JE, Timlin MS, Miller JS, Scott JD (2004) The atmospheric response to realistic Arctic Sea ice anomalies in an AGCM during winter. J Clim 17(5):890–905. https://doi.org/10.1175/1520-0442(2004)017<0890:TARTRA>2.0.CO;2

Ashok K, Behera SK, Rao SA, Weng H, Yamagata T (2007) El Niño Modoki and its possible teleconnection. J Geophys Res 112(C11):C11,007. https://doi.org/10.1029/2006JC003798

Barnes E (2013) Revisiting the evidence linking Arctic amplification to extreme weather in midlatitudes. Geophys Res Lett 40(17):4734–4739. https://doi.org/10.1002/grl.50880

Barnes EA, Dunn-Sigouin E, Masato G, Woollings T (2014) Exploring recent trends in Northern Hemisphere blocking. Geophys Res Lett 41(2):638–644. https://doi.org/10.1002/2013GL058745

Bernacchia A, Pigolotti S (2011) Self-consistent method for density estimation. J R Stat Soc B Stat Methodol 73(3):407–422. https://doi.org/10.1111/j.1467-9868.2011.00772.x. arXiv:0908.3856

Branstator G, Teng H, Branstator G, Teng H (2017) Tropospheric waveguide teleconnections and their seasonality. J Atmos Sci JAS-D-16-0305.1. https://doi.org/10.1175/JAS-D-16-0305.1

Brekke LD, Maurer EP, Anderson JD, Dettinger MD, Townsley ES, Harrison A, Pruitt T (2009) Assessing reservoir operations risk under climate change. Water Resour Res 45(4):1–16. https://doi.org/10.1029/2008WR006941

Cal Fire (2018a) Ranch Fire (Mendcino complex). http://www.fire.ca.gov/current_incidents/incidentdetails/Index/2175

Cal Fire (2018b) InciWeb. Thomas fire incident information. http://cdfdata.fire.ca.gov/incidents/incidents_details_info?incident_id=1922. Accessed 6 Aug 2018

Capotondi A, Wittenberg AT, Newman M, Di Lorenzo E, Yu JY, Braconnot P, Cole J, Dewitte B, Giese B, Guilyardi E, Jin FF,

Karnauskas K, Kirtman B, Lee T, Schneider N, Xue Y, Yeh SW (2015) Understanding ENSO diversity. Bull Am Meteorol Soc 96(6):921–938. https://doi.org/10.1175/BAMS-D-13-00117.1

Cayan DR, Redmond KT, Riddle LG (1999) ENSO and hydrologic extremes in the western United States. J Clim 12(9):2881–2893. https://doi.org/10.1175/1520-0442(1999)012<2881:EAHEIT>2.0.CO;2

Cayan DR, Dettinger MD, Kammerdiener SA, Caprio JM, Peterson DH (2001) Changes in the onset of spring in the western United States. Bull Am Meteorol Soc 82(3):399–415. https://doi.org/10.1175/1520-0477(2001)082<0399:CITOOS>2.3.CO;2

Center USNCD (2016) National Climate Data Center NCDC climate data online. http://www7.ncdc.noaa.gov/CDO/CDODivisionalSelect.jsp

Cohen J, Screen JA, Furtado JC, Barlow M, Whittleston D, Coumou D, Francis J, Dethloff K, Entekhabi D, Overland J, Jones J (2014) Recent Arctic amplification and extreme mid-latitude weather. Nat Geosci 7(9):627–637. https://doi.org/10.1038/ngeo2234. http://www.nature.com/articles/ngeo2234. arXiv:1204.5445

Compo GP, Whitaker JS, Sardeshmukh PD, Matsui N, Allan RJ, Yin X, Gleason BE, Vose RS, Rutledge G, Bessemoulin P, Brönnimann S, Brunet M, Crouthamel RI, Grant AN, Groisman PY, Jones PD, Kruk MC, Kruger AC, Marshall GJ, Maugeri M, Mok HY, Nordli Ø, Ross TF, Trigo RM, Wang XL, Woodruff SD, Worley SJ (2011) The twentieth century reanalysis project. Q J R Meteorol Soc 137(654):1–28. https://doi.org/10.1002/qj.776

Cook BI, Cook ER, Smerdon JE, Seager R, Williams AP, Coats S, Stahle DW, Díaz JV (2016) North American megadroughts in the common era: reconstructions and simulations. Wiley Interdiscip Rev Clim Change 7(3):411–432. https://doi.org/10.1002/wcc.394

DeFlorio MJ, Pierce DW, Cayan DR, Miller AJ (2013) Western U.S. extreme precipitation events and their relation to ENSO and PDO in CCSM4. J Clim 26(12):4231–4243. https://doi.org/10.1175/JCLI-D-12-00257.1

Diffenbaugh NS, Swain DL, Touma D (2015) Anthropogenic warming has increased drought risk in California. Proc Natl Acad Sci 112(13):3931–3936. https://doi.org/10.1073/pnas.1422385112

Ding A (2018) Charting the financial damage of the Thomas Fire. https://thebottomline.as.ucsb.edu/2018/04/charting-the-financial-damage-of-the-thomas-fire

Enfield DB, Mestas-Nuñez AM, Trimble PJ (2001) The Atlantic multidecadal oscillation and its relation to rainfall and river flows in the continental U.S. Geophys Res Lett 28(10):2077–2080. https://doi.org/10.1029/2000GL012745

Favre A, Gershunov A (2006) Extra-tropical cyclonic/anticyclonic activity in north-eastern Pacific and air temperature extremes in western North America. Clim Dyn 26(6):617–629. https://doi.org/10.1007/s00382-005-0101-9

Feldl N, Roe GH (2011) Climate variability and the shape of daily precipitation: a case study of ENSO and the American west. J Clim 24(10):2483–2499. https://doi.org/10.1175/2010JCLI3555.1

Francis JA, Vavrus SJ (2015) Evidence for a wavier jet stream in response to rapid Arctic warming. Environ Res Lett 10(1):014005. https://doi.org/10.1088/1748-9326/10/1/014005. http://stacks.iop.org/1748-9326/10/i=1/a=014005?key=crossref.74581076f734b2377ec8042d3aebe25d

Gershunov A (1998) ENSO influence on intraseasonal extreme rainfall and temperature frequencies in the contiguous United States: implications for long-range predictability. J Clim 11(12):3192–3203. https://doi.org/10.1175/1520-0442(1998)011<3192:EIOIER>2.0.CO;2

Gershunov A, Barnett TP (1998) Interdecadal modulation of ENSO teleconnections. Bull Am Meteorol Soc 79(12):2715–2725. https://doi.org/10.1175/1520-0477(1998)079<2715:IMOET>2.0.CO;2

Guirguis K, Gershunov A, Cayan DR (2015) Interannual variability in associations between seasonal climate, weather, and extremes: wintertime temperature over the southwestern United States. Environ Res Lett 10(12). https://doi.org/10.1088/1748-9326/10/12/124023

Hoerling MP, Kumar A, Zhong M (1997) El Niño, La Niña, and the nonlinearity of their teleconnections. J Clim 10(8):1769–1786. https://doi.org/10.1175/1520-0442(1997)010<1769:ENOLNA>2.0.CO;2

Holmes CR, Woollings T, Hawkins E, de Vries H (2016) Robust future changes in temperature variability under greenhouse gas forcing and the relationship with thermal advection. J Clim 29(6):2221–2236. https://doi.org/10.1175/JCLI-D-14-00735.1

Intergovernmental Panel on Climate Change (ed) (2014) Climate change 2013—the physical science basis. Cambridge University Press, Cambridge. https://doi.org/10.1017/CBO9781107415324. http://ebooks.cambridge.org/ref/id/CBO9781107415324

JAMSTEC (2018) Modoki index. http://www.jamstec.go.jp/frsgc/research/d1/iod/DATA/emi.monthly.txt

Jasperse J, Ralph M, Anderson M, Brekke LD, Dillabough M, Dettinger M, Haynes A, Hartman R, Jones C, Forbis J, Rutten P, Talbot C, Webb RH (2017) Preliminary viability assessment of Lake Mendocino forecast informed reservoir operations. In: Technical report, USGS. http://pubs.er.usgs.gov/publication/70192184

Kanamitsu M, Ebisuzaki W, Woollen J, Yang SK, Hnilo JJ, Fiorino M, Potter GL (2002) NCEP-DOE AMIP-II reanalysis (R-2). Bull Am Meteorol Soc 83(11):1631–1644. https://doi.org/10.1175/BAMS-83-11-1631

Kang IS, No Hh, Kucharski F (2014) ENSO amplitude modulation associated with the mean SST changes in the tropical central Pacific induced by Atlantic multidecadal oscillation. J Clim 27(20):7911–7920. https://doi.org/10.1175/JCLI-D-14-00018.1

Kerr RA (2000) A North Atlantic climate pacemaker for the centuries. Science 288(5473):1984–1985. https://doi.org/10.1126/science.288.5473.1984

Knowles N, Dettinger MD, Cayan DR (2006) Trends in snowfall versus rainfall in the western United States. J Clim 19(18):4545–4559. https://doi.org/10.1175/JCLI3850.1. arXiv:0504262v1

Krichak SO, Breitgand JS, Gualdi S, Feldstein SB (2014) Teleconnection-extreme precipitation relationships over the Mediterranean region. Theor Appl Climatol 117(3–4):679–692. https://doi.org/10.1007/s00704-013-1036-4

Lauer S (2011) Sierra Nevada water facts. In: Technical report, Water Education Foundation. http://www.sierranevadaconservancy.ca.gov/our-region/docs/sierrabookletfinal.pdf

Leonard M, Westra S, Phatak A, Lambert M, van den Hurk B, McInnes K, Risbey J, Schuster S, Jakob D, Stafford-Smith M (2014) A compound event framework for understanding extreme impacts. Wiley Interdiscip Rev Clim Change 5(1):113–128. https://doi.org/10.1002/wcc.252

Levine AFZ, McPhaden MJ, Frierson DMW (2017a) The impact of the AMO on multidecadal ENSO variability. Geophys Res Lett 44(8):3877–3886. https://doi.org/10.1002/2017GL072524

Levine AFZ, McPhaden MJ, Frierson DMW (2017b) The impact of the AMO on multidecadal ENSO variability. Geophys Res Lett 44(8):3877–3886. https://doi.org/10.1002/2017GL072524

L'Heureux ML, Takahashi K, Watkins AB, Barnston AG, Becker EJ, Di Liberto TE, Gamble F, Gottschalck J, Halpert MS, Huang B, Mosquera-Vásquez K, Wittenberg AT (2017) Observing and predicting the 2015/16 El Niño. Bull Am Meteorol Soc 98(7):1363–1382. https://doi.org/10.1175/BAMS-D-16-0009.1. arXiv:9812034

Livezey RE, Masutani M, Leetmaa A, Rui H, Ji M, Kumar A (1997) Teleconnective response of the Pacific-North American region atmosphere to large central equatorial Pacific SST anomalies. J Clim 10(8):1787–1820. https://doi.org/10.1175/1520-0442(1997)010<1787:TROTPN>2.0.CO;2

Mahony CR, Cannon AJ (2018) Wetter summers can intensify departures from natural variability in a warming climate. Nat Commun 9(1):783. https://doi.org/10.1038/s41467-018-03132-z. http://www.nature.com/articles/s41467-018-03132-z

Mantua NJ, Hare SR, Zhang Y, Wallace JM, Francis RC (1997) A Pacific interdecadal climate oscillation with impacts on salmon production. Bull Am Meteorol Soc 78(6):1069–1079. https://doi.org/10.1175/1520-0477(1997)078<1069:APICOW>2.0.CO;2

McCabe GJ, Dettinger MD (2002) Primary modes and predictability of year-to-year snowpack variations in the western United States from teleconnections with Pacific Ocean climate. J Hydrometeorol 3(1):13–25. https://doi.org/10.1175/1525-7541(2002)003<0013:PMAPOY>2.0.CO;2

Meehl GA, Hu A (2006) Megadroughts in the Indian monsoon region and southwest North America and a mechanism for associated multidecadal Pacific Sea surface temperature anomalies. J Clim 19(9):1605–1623. https://doi.org/10.1175/JCLI3675.1

Mestas-Nuñez AM, Enfield DB (1999) Rotated global modes of non-ENSO sea surface temperature variability. J Clim 12(9):2734–2746. https://doi.org/10.1175/1520-0442(1999)012<2734:RGMONE>2.0.CO;2

Mo KC, Livezey RE (1986) Tropical-extratropical geopotential height teleconnections during the Northern Hemisphere winter. Mon Weather Rev 114(12):2488–2515. https://doi.org/10.1175/1520-0493(1986)114<2488:TEGHTD>2.0.CO;2

Mote PW, Hamlet AF, Clark MP, Lettenmaier DP (2005) Declining mountain snowpack in western North America. Bull Am Meteorol Soc 86(1):39–50. https://doi.org/10.1175/BAMS-86-1-39

National Center for Atmospheric Research Staff (2019) The climate data guide: overview: climate indices. https://climatedataguide.ucar.edu/climate-data/overview-climate-indices

National Oceanic and Atmospheric Administration, Earth System Research Laboratory PSD (2019) Climate indices: monthly atmospheric and ocean time-series. https://www.esrl.noaa.gov/psd/data/climateindices/list/

Neiman PJ, White AB, Ralph FM, Gottas DJ, Gutman SI (2009) A water vapour flux tool for precipitation forecasting. Proc Inst Civil Eng Water Manag 162(2):83–94. https://doi.org/10.1680/wama.2009.162.2.83

Newman M, Alexander MA, Ault TR, Cobb KM, Deser C, Di Lorenzo E, Mantua NJ, Miller AJ, Minobe S, Nakamura H, Schneider N, Vimont DJ, Phillips AS, Scott JD, Smith CA (2016) The Pacific decadal oscillation. Revisited. J Clim 29(12):4399–4427. https://doi.org/10.1175/JCLI-D-15-0508.1

O'Brien TA, Collins WD, Rauscher SA, Ringler TD (2014) Reducing the computational cost of the ECF using a nuFFT: a fast and objective probability density estimation method. Comput Stat Data Anal 79:222–234. https://doi.org/10.1016/j.csda.2014.06.002

O'Brien TA, Kashinath K, Cavanaugh NR, Collins WD, O'Brien JP (2016) A fast and objective multidimensional kernel density estimation method: FastKDE. Comput Stat Data Anal 101:148–160. https://doi.org/10.1016/j.csda.2016.02.014. http://linkinghub.elsevier.com/retrieve/pii/S0167947316300408

Palmer T (2014) Record-breaking winters and global climate change. Science 344(6186):803–804. https://doi.org/10.1126/science.1255147. http://science.sciencemag.org/content/344/6186/803.abstract

Parmesan C (2006) Ecological and evolutionary responses to recent climate change. Annu Re Ecol Evol Syst 37(1):637–669. https://doi.org/10.1146/annurev.ecolsys.37.091305.110100

Pierce DW (2002) The role of sea surface temperatures in interactions between ENSO and the North Pacific oscillation. J Clim 15(11):1295–1308. https://doi.org/10.1175/1520-0442(2002)015<1295:TROSST>2.0.CO;2

Polade SD, Gershunov A, Cayan DR, Dettinger MD, Pierce DW (2013) Natural climate variability and teleconnections to precipitation over the Pacific–North American region in CMIP3 and CMIP5 models. Geophys Res Lett 40(10):2296–2301. https://doi.org/10.1002/grl.50491

Polade SD, Pierce DW, Cayan DR, Gershunov A, Dettinger MD (2014) The key role of dry days in changing regional climate and precipitation regimes. Sci Rep 4:1–8. https://doi.org/10.1038/srep04364

Polade SD, Gershunov A, Cayan DR, Dettinger MD, Pierce DW (2017) Precipitation in a warming world: assessing projected hydro-climate changes in California and other Mediterranean climate regions. Sci Rep 7(1):1–10. https://doi.org/10.1038/s41598-017-11285-y

Poli P, Hersbach H, Dee DP, Berrisford P, Simmons AJ, Vitart F, Laloyaux P, Tan DG, Peubey C, Thépaut JN, Trémolet Y, Hólm EV, Bonavita M, Isaksen L, Fisher M (2016) ERA-20C: an atmospheric reanalysis of the twentieth century. J Clim 29(11):4083–4097. https://doi.org/10.1175/JCLI-D-15-0556.1

Rayner NA (2003) Global analyses of sea surface temperature, sea ice, and night marine air temperature since the late nineteenth century. J Geophys Res 108(D14):4407. https://doi.org/10.1029/2002JD002670. http://www.ncbi.nlm.nih.gov/pubmed/509

Rhines A, McKinnon KA, Tingley MP, Huybers P (2017) Seasonally resolved distributional trends of North American temperatures show contraction of winter variability. J Clim 30(3):1139–1157. https://doi.org/10.1175/JCLI-D-16-0363.1

Rutz JJ, Steenburgh WJ, Ralph FM (2014) Climatological characteristics of atmospheric rivers and their inland penetration over the western United States. Mon Weather Rev 142(2):905–921. https://doi.org/10.1175/MWR-D-13-00168.1

Sarhadi A, Ausín MC, Wiper MP, Touma D, Diffenbaugh NS (2018) Multidimensional risk in a nonstationary climate: Joint probability of increasingly severe warm and dry conditions. Sci Adv 4(11):eaau3487. https://doi.org/10.1126/sciadv.aau3487

Savtchenko AK, Huffman G, Vollmer B (2015) Assessment of precipitation anomalies in California using TRMM and MERRA data. J Geophys Res Atmos 120(16):8206–8215. https://doi.org/10.1002/2015JD023573

Schlesinger ME, Ramankutty N (1994) An oscillation in the global climate system of period 65–70 years. Nature 367(6465):723–726. https://doi.org/10.1038/367723a0

Screen JA, Simmonds I (2013) Exploring links between Arctic amplification and mid-latitude weather. Geophys Res Lett 40(5):959–964. https://doi.org/10.1002/grl.50174

Seager R, Henderson N (2016) On the role of Tropical Ocean forcing of the persistent North American west coast ridge of winter 2013/14. J Clim 29(22):8027–8049. https://doi.org/10.1175/JCLI-D-16-0145.1

Seager R, Hoerling M, Schubert S, Wang H, Lyon B, Kumar A, Nakamura J, Henderson N (2015) Causes of the 2011–14 California drought. J Clim 28(18):6997–7024. https://doi.org/10.1175/JCLI-D-14-00860.1

Serinaldi F, Kilsby CG (2015) Stationarity is undead: uncertainty dominates the distribution of extremes. Adv Water Resour 77:17–36. https://doi.org/10.1016/j.advwatres.2014.12.013. https://linkinghub.elsevier.com/retrieve/pii/S0309170815000020

Sewall JO (2005) Precipitation shifts over western North America as a result of declining Arctic Sea ice cover: the coupled system response. Earth Interact 9(26):1–23. https://doi.org/10.1175/EI171.1

Singh D, Swain DL, Mankin JS, Horton DE, Thomas LN, Rajaratnam B, Diffenbaugh NS (2016) Recent amplification of the North American winter temperature dipole. J Geophys Res Atmos 121(17):9911–9928. https://doi.org/10.1002/2016JD025116

Steadman RG (1979) The assessment of sultriness. Part I: A temperature-humidity index based on human physiology and clothing science. J Appl Meteorol 18(7):861–873. https://doi.org/10.1175/1520-0450(1979)018<0861:TAOSPI>2.0.CO;2

Stewart IT, Cayan DR, Dettinger MD (2005) Changes toward earlier streamflow timing across western North America. J Clim 18(8):1136–1155. https://doi.org/10.1175/JCLI3321.1

Swain DL, Tsiang M, Haugen M, Singh D, Charland A, Rajaratnam B, Diffenbaugh NS (2014) The extraordinary California drought of 2013/2014: character, context, and the role of climate change (in "explaining extremes of 2013 from a climate perspective"). Bull Am MeteorOL Soc 95(9):S3–S7

Swain DL, Singh D, Horton DE, Mankin JS, Ballard TC, Diffenbaugh NS (2017) Remote linkages to anomalous winter atmospheric ridging over the northeastern Pacific. J Geophys Res Atmos 122(22):12,194–12,209. https://doi.org/10.1002/2017JD026575

Swain DL, Langenbrunner B, Neelin JD, Hall A (2018) Increasing precipitation volatility in twenty-first-century California. Nat Clim Change 8(5):427–433. https://doi.org/10.1038/s41558-018-0140-y. http://www.nature.com/articles/s41558-018-0140-y

Team G (2018) GISS surface temperature analysis (GISTEMP)

Teng H, Branstator G (2017) Causes of extreme ridges that induce California droughts. J Clim 30(4):1477–1492. https://doi.org/10.1175/JCLI-D-16-0524.1

Trenberth KE, Hurrell JW (1994) Decadal atmosphere-ocean variations in the Pacific. Clim Dyn 9(6):303–319. https://doi.org/10.1007/BF00204745. arXiv:0601117

Wang H, Schubert S (2014) Causes of the extreme dry conditions over California during early 2013 (in "explaining extremes of 2013 from a climate perspective"). Bull Am Meteorol Soc 95(9):S7–S11. https://doi.org/10.1175/1520-0477-95.9.S1.1

Wang SY, Hipps L, Gillies RR, Yoon JH (2014) Probable causes of the abnormal ridge accompanying the 2013–2014 California drought: ENSO precursor and anthropogenic warming footprint. Geophys Res Lett 41(9):3220–3226. https://doi.org/10.1002/2014GL059748

Wang SYS, Huang WR, Yoon JH (2015) The North American winter 'dipole' and extremes activity: a CMIP5 assessment. Atmos Sci Lett 16(3):338–345. https://doi.org/10.1002/asl2.565

Wang SYS, Yoon JH, Becker E, Gillies R (2017) California from drought to deluge. Nat Clim Change 7(7):465–468. https://doi.org/10.1038/nclimate3330

Watson PAG, Weisheimer A, Knight JR, Palmer TN (2016) The role of the tropical West Pacific in the extreme Northern Hemisphere winter of 2013/2014. J Geophys Res Atmos 121(4):1698–1714. https://doi.org/10.1002/2015JD024048

Wehner M, Stone D, Krishnan H, AchutaRao K, Castillo F (2016) The deadly combination of heat and humidity in India and Pakistan in summer 2015. Bull Am Meteorol Soc 97(12):S81–S86. https://doi.org/10.1175/BAMS-D-16-0145.1

Williams AP, Seager R, Abatzoglou JT, Cook BI, Smerdon JE, Cook ER (2015) Contribution of anthropogenic warming to California drought during 2012–2014. Geophys Res Lett 42(16):6819–6828. https://doi.org/10.1002/2015GL064924

Williams IN, Patricola CM (2018) Diversity of ENSO events unified by convective threshold sea surface temperature: a nonlinear ENSO index. Geophys Res Lett 45(17):9236–9244. https://doi.org/10.1029/2018GL079203

Wolter K, Timlin MS (1993) Monitoring ENSO in COADS with a seasonally adjusted principal component index

Wolter K, Hoerling M, Eischeid JK, van Oldenborgh GJ, Quan XW, Walsh JE, Chase TN, Dole R (2015) How unusual was the cold winter of 2013/14 in the upper midwesT? (in "explaining extremes of 2014 from a climate perspective"). Bull Am Meteorol Soc 96(12):S10–S14

Yoon JH, Kravitz B, Rasch PJ, Simon Wang SY, Gillies RR, Hipps L (2015) Extreme fire season in California: a glimpse into the future? Bull Am Meteorol Soc 96(12):S5–S9. https://doi.org/10.1175/BAMS-D-15-00114.1

This page left intentionally blank.

Chapter 2

The Anthropogenic Contribution to the Observed Hydrometeorology over the Continental U.S. from 1960-2018

2.1 Introduction

Since the industrial revolution, human activities have been steadily altering the composition and thermal properties of the global atmosphere (Arrhenius, 1897, Myhre et al., 2013). Since that time, the global mean temperature has risen by about 1°C (Lenssen et al., 2019), primarily due to carbon dioxide emissions from the combustion of fossil fuels and industrial processes (Olivier et al., 2005, Myhre et al., 2013). While the temperature response of the global climate system to increased radiative forcing from greenhouse gasses is fairly well-constrained(Andrews et al., 2012), the response of the hydrologic cycle is less well understood. As a func-

tion of temperature, atmospheric water vapor increases at a predictable 7%/°C rate following Clausius-Clapeyron (Allen and Ingram, 2002, Held and Soden, 2006). However, globally, the mean precipitation rate scales more modestly (1-3%/°C) (Allen and Ingram, 2002, Lambert et al., 2004), and is capped by an energy constraint, namely the ability of the earth's atmosphere to radiatively cool and balance the latent heating generated by precipitation (Mitchell et al., 2007, Held and Soden, 2006, Pendergrass and Hartmann, 2014). In addition, it is expected that with climate change, wet regions will tend to get wetter and dry regions to get drier, accompanied by an increase in extreme events such as episodes of intense precipitation and extended periods of drought (Trenberth, 1999, Allen and Ingram, 2002, Held and Soden, 2006). The disparity between the rate of increase of atmospheric water vapor and the global mean precipitation rate suggests that for precipitation rates to balance globally, there must be a decrease in light/moderate rain events and an increase in heavy events (Trenberth, 1999, Trenberth et al., 2003, Hennessy et al., 1997, Allan and Soden, 2008). Indeed, both observations and model simulations show increasing trends in both mean and extreme precipitation with trends in the extremes generally outpacing trends in the mean (Karl and Knight, 1998, Kunkel et al., 2013).

Given that it is generally well-established that extreme events are increasing with climate change, it is natural to ask to what extent, and how, anthropogenic forcing altered an extreme event once it has happened (Stone and Allen, 2005, Otto et al., 2018). However, this question is often intractable due many factors including but not limited to natural forcing, subgrid-scale processes, and random chance

(Zwiers et al., 2013). Broadly, detection refers to the identification of some change in the climate system, or, with respect to individual weather events, the observation of an extreme event with a low probability of occurrence (Mirle et al., 2013). Attribution on the other hand, seeks to assign some proportion of the simulated response (the extreme event) to one or more of the variables implicated in the process underlying the generation of the event. Thus, the class of studies referred to as 'Detection and Attribution' (D&A) seeks to identify and document a change in the physical system, then describe how the probability of occurrence (or intensity) of that event has changed resulting from a change to one or more of the physical drivers of the event in question (Barnett et al., 2005b).

While the detection and attribution of extremes is still a relatively new and developing field (Otto, 2017), there exist several different methods to understand the relative contributions of individual drivers of extreme events, the one typically of greatest interest being human caused climate change. Among the most employed method, is "fingerprinting" whereby detection is commonly accomplished by correlating a predicted anthropogenic signal with observations to detect/identify the anthropogenic fingerprint (Madden and Ramanathan, 1980, Santer et al., 1993, 1995, Hegerl and North, 1997, Allen and Stott, 2003, Barnett et al., 2005b, Santer et al., 2009, Hegerl and Zwiers, 2011). Fingerprinting methods have been successfully used to detect anthropogenically forced changes in many different climate variables, most notably temperature (Hegerl et al., 1997, Tett et al., 1999, Barnett et al., 2005b, Stott et al., 2007), and CO_2 (Hegerl et al., 1996, 1997). Additionally, anthropogenically forced changes have been detected in sea level pressure (Gillett et al., 2003),

tropopause height (Santer et al., 2003), and ocean heat uptake (Barnett et al., 2005a).

More recently, interest has grown in attributing human induced change to individual weather events such as heatwaves, cold snaps, droughts, and severe storms such as regionally confined mesoscale convective events such as monsoonal precipitation to synoptic scale tropical cyclones (Otto et al., 2018). Broadly, studies aimed at preforming D&A on individual weather events follow a concept involving modeling "factual" and "counterfactual" cases (Stone and Allen, 2005, Otto, 2017). The modeled factual case represents the event in question as it occurred, driven by an all-forcing scenario, whereas the counterfactual case models the event with forcings that would be expected had human-induced climate change never happened. Attribution studies designed under this framework have seen promising success demonstrated by recent work on the U.K. floods of 2000 (Pall et al., 2011), the European heatwave of 2003 (Stott et al., 2004), the Boulder, Colorado floods of 2013 (Pall et al., 2017), and several land-falling Atlantic hurricanes including Katrina, Maria, and Irma (Patricola and Wehner, 2018). In addition, D&A studies employing covariate-based Generalized Extreme Value (GEV) theory have been developed to isolate natural versus anthropogenic effects on extreme events such as hurricane Harvey (Risser and Wehner, 2017).

2.2 Changes in Precipitation over the Continental U.S.

There is little doubt that society and our infrastructure have become increasingly vulnerable to weather and climate extremes (Kunkel et al., 1999). At present, there

is a large and ever-growing body of research that has documented increased mean and extreme precipitation across a range of spatial and temporal scales (Karl and Knight, 1998, Kunkel et al., 2013, Higgins and Kousky, 2013, Easterling et al., 2017). On average, across the Continental U.S. (CONUS), annual precipitation has increased by approximately 4% since 1901, marked by decreases in the West, Southwest, and Southeast, while increases across the greater Plains region, the Northeast, and Midwest (Easterling et al., 2017). Additionally, since 1958, extreme precipitation corresponding to daily events that exceed the 99^{th} percentile has increased uniformly across all regions of CONUS, showing an average increase of nearly 27% (Easterling et al., 2017). Moreover, it is not just that the magnitude of extreme precipitation that is changing, but also the areas that are affected by increasing extreme precipitation are expanding as well (Dittus et al., 2016).

These changes manifest in a number of different ways, perhaps most notably, in the increase in the number of billion dollar disasters associated with flooding and thunderstorms, of which flooding is among the costliest (Kunkel et al., 1999, Changnon, 2003, Bell et al., 2018, NOAA National Centers for Environmental Information (NCEI), 2019). Extreme precipitation and major flooding events are continuing to increase in both magnitude and frequency (Kunkel et al., 1999, 2013), and people are increasingly asking if anthropogenic climate change is implicated (Otto et al., 2018). In many instances, this is appearing more and more to be the case. For example, in the southern U.S. from August 12-14, 2016, central Louisiana sustained three days of extreme rain that resulted in unprecedented flooding for the area and caused damage to over 60,000 homes and displaced over 10,000 people

(Van der Wiel et al., 2017). In a rapid attribution study published soon after the event occurred, the authors found that anthropogenic forcing increased the probability of 3-day precipitation of that magnitude by at least 1.4 times (Van der Wiel et al., 2017). In the inter-mountain west, on September 9^{th} - 15^{th} 2013, Boulder, Colorado, experienced severe flooding resulting in over two billion dollars worth of damage and nine fatalities (Gochis et al., 2015). The extreme rainfall Boulder experienced was unprecedented in the historical record and researchers have estimated that anthropogenic forcing increased the magnitude of such an event by at least 30% (Pall et al., 2017). Increasingly, researchers are finding more and more evidence that human activities are having an effect on the global hydrologic cycle and extreme events (Min et al., 2011, Marvel et al., 2019). This motivates asking how and to what extent anthropogenic forcing has altered the precipitation patterns we experienced.

2.3 Detection and Attribution using Counterfactual Climates and Large Ensembles

Extreme events are by definition rare events, therefore quantifying their probability of occurrence from the observational record is difficult due to the low sample size (Easterling, 2000). Moreover, understanding how and if human activities have altered those probabilities is even more difficult due to the confounding fact that we do not have observations of a world without human influence. Thus given our one "realization" of observations of the climate system, we have nothing with which to

compare as a baseline case of what the global climate would be like had humans never interfered. As such, we cannot say from observations alone how the climate and weather patterns, and in particular the extreme events, we have experienced were or were not changed due to anthropogenic forcing.

In light of these difficulties, we can employ climate models to allow us to probe alternate climate scenarios. These so-called "counterfactual" climate simulations are constructed such that the human-induced radiative forcing due to greenhouse gasses (GHG) and aerosols are removed from the historical climate observed over the last 60 years (see Section 2.4.2 below for full details) (Folland et al., 2014, Stone and Pall, 2017, Stone et al., 2018, 2019). We compare the counterfactual climate to the "factual" climate modeled using the observed radiative forcings and boundary conditions. Both these scenarios are simulated 50 times with perturbed initial conditions for each year between 1959 and 2018. This results in 2950 simulated years for both the factual (All-hist) case and the counterfactual (Nat-hist) case. With a sampling of years this large, we are able to increase the signal-to-noise and directly calculate the probabilities of precipitation extremes and mean responses. That is, for example, in this ensemble a 1-in-100 year event will roughly 30 times. We calculate the anthropogenic effect on changes in the probability of hydrometeorological extremes as the residual between the modeled factual climate and the counterfactual climate. By doing this, model biases for simulated precipitation are removed, leaving self-consistent estimates of the anthropogenic effect on the observed hydrometeorology. Further, this approach removes the confounding factor of natural variability (Kunkel et al., 2003, Hoerling et al., 2016, Stegall and Kunkel,

2019), arising from internal climate forcings (Deser et al., 2004, 2014), such as the El Niño Southern Oscillation (ENSO) and the Pacific Decadal Oscillation (PDO) since the observed ocean variability is preserved in both the All- and Nat-hist simulations (Stone et al., 2019).

Thus the primary goal of this study is to understand the role anthropogenic forcing has played in altering modeled boreal wintertime precipitation patterns over CONUS from 1960-2018. We employ a "counterfactual" methodology as a means of separating out the bulk anthropogenic signal on precipitation from naturally ocean-forced variability experienced over this time period. We diagnose anthropogenically forced changes to both expected (mean) and extreme precipitation at multiple timescales ranging from seasonal to daily. We seek to quantify these changes and to place them in the broader context of an altered hydrologic cycle, which includes as well, extremely dry winter seasons, changes to the number of dry wintertime days, and their consecutive occurrence. We focus on the boreal winter season as the drivers of ascent during this time are controlled by synoptic scale disturbances associated with large-scale, resolved precipitation.

2.4 Data and Methods

2.4.1 Indices of Environmental Change

For this analysis we focus on metrics of the hydrologic cycle that are most relevant to human and environmental systems on timescales ranging from daily to seasonal. To that end, we choose a subset of indices guided by the Expert Team of Climate

Change Detection and Indices that are designed to enable the ongoing monitoring of changes to both the frequency and magnitude of extreme events in light of a changing climate (Zhang et al., 2011). The recommended indices are chosen such that they are physically-based and have broad geographical relevance. The subset of indices used in this study are adapted from an annual timescale as described in Zhang et al. (2011), to the seasonal timescale used in this study, specifically the boreal winter defined here to be November - March the following calendar year. The subset of indices we consider here are as follows: Rx1d- the maximum amount of precipitation received in one day; Rx5d- the maximum amount of 5-day total precipitation; Rx10d- the maximum amount of 10-day total precipitation; Rx40d- the maximum amount of 40-day total precipitation; the mean precipitation rate when raining (labeled SDII in (Zhang et al., 2011)); the max continuous wet period (CWD); the number of consecutive dry days (NDD); and the max continuous dry period (CDD). Taken together, these metrics give a comprehensive view the behaviour of the hydrologic cycle across a range of temporal scales.

2.4.2 Data

For this study we employ data from the database of the Climate of the 20th Century Plus Detection and Attribution project (C20C + D&A, henceforth C20C+) (Folland et al., 2014). Broadly, the C20C+ experiment consists of a multi-model large ensemble of AMIP-style simulations (Gates, 1992), forced by observed land, ocean, and atmospheric boundary conditions (Stone et al., 2019). Specifically this study uses daily output from two large ensembles from the Community Atmosphere Model

(CAM5.1), the atmospheric component of the Community Earth System Model (CESM) (Neale et al., 2012), run at a 1-degree horizontal grid resolution. The first large ensemble set of simulations are run under an all-forcings scenario (the "factual" scenario), referred to here as the All-hist simulations. Model output from these simulations are subject to radiative forcings from changing carbon dioxide levels and solar luminosity as well as from prescribed sulphate, organic, black carbon, dust, sea salt, and volcanic aerosol burdens (see Stone et al. (2018) for additional details). Further, observed ocean sea surface temperatures (SSTs) are used as well as observed sea ice concentrations (SIC). The ocean in this configuration does not interact with the atmospheric model, thus observed SST variability is preserved. Observed land surface cover/use are incorporated into the simulations using the community land model 4.0 (CLM4.0), which dynamically interacts with CAM5.1.

The second large ensemble we use is from the subset simulations that make up the detection and attribution part of the C20C+ experiment (Gillett et al., 2016). These simulations are run under a natural-forcings scenario (the "counterfactual" scenario), referred to here as the Nat-hist simulations. The configuration of these simulations are identical to the All-hist simulations with the key difference being the removal of the estimated effects of human activities on the global climate system. This entails removing the excess radiative forcing from atmospheric tropospheric and ocean warming due to anthropogenic forcing. The excess radiative forcing due to human activities in the atmosphere is removed by fixing the carbon dioxide and aerosol levels in each Nat-hist simulation to the estimated preindustrial levels of the year 1855 (for carbon dioxide this equates to approximately 285ppm). Anthro-

pogenically forced ocean warming is calculated as the residual warming between the historical and the historicalNat simulations that make up the coupled model intercomparison project phase 5 (CMIP5) (Taylor et al., 2012). The models that make up the CMIP5 archive are fully coupled and have dynamically interacting modules, which can take into account feedbacks among the different climate systems, nonlinear or otherwise. The historical simulations include radiative forcings from both anthropogenic and natural sources while the historicalNat simulations include only natural forcings. This method of removing the anthropogenic contribution to ocean warming is a key and distinguishing feature of C20C+ experimental design in that it achieves cooling the oceans to the estimated preindustrial temperatures while also preserving the observed ocean variability (e.g. ENSO, PDO, AMO, etc.). As such, for example, years where strong El Niño occurred in the observed record (e.g. 1983,1998) also occur in the corresponding years in both the All- and Nat-hist simulations, however, at a lower mean SST in the Nat-hist simulations. Additionally, in the Nat-hist simulations, sea ice concentrations are adjusted to be consistent with the cooler adjusted radiative environment according the observed temperature - sea ice relationship detailed in (Stone and Pall, 2017). Thus the Nat-hist simulations are designed to be a representation of the global climate system as have might have existed without human interference.

The simulations that make up each large ensemble have random uniform initial condition perturbations applied to the three-dimensional temperature field such that the trajectory of each simulation spans the climate and weather states possible under the applied boundary conditions. Each large ensemble (All-hist and Nat-hist)

include 400 ensemble members each; however, for this study we choose to use only the subset of the 50 "long-duration" simulations spanning years 1959-2018 (Stone et al., 2018). We make this choice in order to have enough years to calculate meaningful changes in the chosen indices across time and so that each year is represented (weighted) equally in the ensemble means. The data from the two large ensembles used in this study are under the experiment headings "All_Hist/est1/v2-0" and "Nat_Hist/CMIP5_est1/v2-0" respectively and are free and available to download at http://portal.nersc.gov/c20c/.

2.4.3 Methods

To study the effects of anthropogenic forcing on the indices described in Section 2.4.1 we consider two primary quantities: changes in the mean and changes in the 100 year return levels. Assessing changes in the mean of any of the given indices in this framework is relatively straightforward: we take the mean across all 50 members (ensemble mean) and across all 59 Nov-March years (time mean) and calculate the anthropogenic effect as the residual between the All-hist and the Nat-hist simulations. This quantity is then the difference in the means of two distributions with 2950 total simulated years and represents the average anthropogenic effect on the index being considered over the Nov-March period spanning 1960 - 2018. As such, to assess the statistical significance in the difference in the two means, we can apply the two-tailed students t-test. We report the significance in the difference of the means at two levels, $p \leq 0.1$ signified by a single horizontal dash ($-$), and at $p \leq 0.01$ signified by a plus ($+$) sign. These hatchings represent medium and high confi-

dence in the result respectively. Finally, it is well-known that no model is perfect and that all have biases to one degree or another for any given field (e.g. Sheffield et al. (2013), Davy and Esau (2014), Kay et al. (2012), Liu et al. (2014)). However, in this framework, using a single model large ensemble and calculating the anthropogenic effects as the residual between model experiments, we avoid the use of observations. This then follows a "perfect model" approach akin to that described by Kirchmeier-Young et al. (2019) where events are framed internally (within model experiments) thus avoiding concerns whether the model is able to reproduce observed values. This then allows the difference between the All- and Nat-hist simulations to be interpreted as the anthropogenic effect on the extreme event in question. That said, a number of different studies have documented the ability of global models forced by observed SSTs to reproduce observed regional precipitation trends with fidelity (e.g. Hoerling et al. (2016), Seager and Hoerling (2014).

To assess changes in the 100 year return levels we approach using two methods, one frequency based and the other magnitude based. For the frequency based method we first calculate the 100 year Nat-hist return level for the index being considered. Note that since we are using daily output from a large ensemble of 50 simulations spanning 59 years, we are able to directly (empirically) calculate 100 year return levels without relying on the theoretical parametric distributions employed by extreme value theory typically used to estimate high percentiles beyond that which the data sampling support. We then count the number of times this threshold is exceeded in the All-hist simulations, which can also be less than the number of times it was exceeded in the Nat-hist simulations. Using the cumulative number of counts

over the threshold in both the All- and Nat-hist simulations we calculate the risk (probability) ratio (RR) in terms of P_F, the probability of an event under the factual (All-hist) scenario and P_C, the same probability under the counterfactual (Nat-hist) scenario as the ratio. The RR is defined as,

$$RR = \frac{P_F}{P_C}, \ni P_F = \frac{\sum I(X_F > c)}{N_F} \quad \text{and} \quad P_C = \frac{\sum I(X_C > c)}{N_C}, \tag{2.1}$$

where X_F is the variable of interest, c the threshold under consideration, $I(\cdot)$ an indicator function which returns 1 when $X > c$ and 0 when $X \leq c$, and N_F, N_C, the number of samples in the factual and counterfactual scenarios respectively (see Paciorek et al. (2018) for full details). Since the counts-over-threshold method is a binary process, that is, for a given sample at a given time/lat/lon, either the threshold was exceeded (1), or it wasn't (0), the distribution of outcomes can be modeled as a binomial process. As such, confidence intervals (CI) on the RR can be estimated at different significance levels (Koopman, 1984, Paciorek et al., 2018). To do this we use the open source statistical software package Climextremes (Paciorek et al., 2018), implemented in Python and available for download at https://bitbucket.org/lbl-cascade/climextremes-dev/src/master/.

We use the RR in this framework for its ease of computation and its straightforward interpretability. For example in this implementation, $RR = 2$ means that the given event under consideration was twice as likely to occur with anthropogenic forcing than was not, and likewise $RR = 0.5$ means that the event probability decreased by half due to anthropogenic climate change. Additionally, we calculate

confidence intervals on the RR at two significance levels, $p \leq 0.1$ signified by a horizontal dash $(-)$ (medium confidence), and $p \leq 0.01$ signified by a plus $(+)$ (high confidence). We stipple grid cells as having a significant positive change in the RR if the lower bound of the CI for the given significance level does not include 1. Similarly, we stipple grid cells where negative changes are observed if the upper bound of the CI for the given significance level does not include 1.

For the magnitude-based method of diagnosing anthropogenically forced changes to the indices under consideration, we directly evaluate changes to the 100 year return level threshold itself. We report values of this metric by the percent change in the magnitude of the 100 year return level between the All-hist and the Nat-hist scenarios. We use all ensemble members and all years to calculate 100 year return level in both the All- and Nat-hist simulations and compare the difference to the magnitude of the 100 year return level in the Nat-hist simulations. For testing statistical significance in this metric of evaluation, we directly calculate the two-tailed p-values from the null distribution. The null distribution, by definition, is a distribution such that the null hypothesis is true, in this case meaning, that there is no difference in the magnitudes of the 100 year return levels between the All- and Nat-hist simulations. To construct the null distribution we pool the data from the All- and Nat-hist simulations, randomly shuffle the pooled data, and then separate the pooled data into two randomly mixed distributions. From these we calculate the 100 year return levels and compute the difference, which on average is zero. We repeat this calculation 500 times to obtain the null distribution. By compute the P-value by assessing the proportion of values in the null distribution that are as

extreme or more than the observed statistic. As with the frequency-based method, significance is reported at two levels: $p \leq 0.1$ signified by a horizontal dash $(-)$ (medium confidence), and $p \leq 0.01$ signified by a plus $(+)$ (high confidence).

For both the frequency- and magnitude-based methods, we apply a hypothesis test at every grid cell location simultaneously. This by definition falls into the class of testing known as multiple hypothesis testing. In testing multiple hypotheses, there will inevitably be some proportion of false discoveries, that is, falsely rejecting the null hypothesis that there is no change. These "false-positive" discoveries are known as type 1 errors and indicate a statistically significant result when in fact the result is not. To control for false-positive discoveries (type 1 errors) in both the frequency- and magnitude-based methods, we apply the false discovery rate (FDR) control method of Benjamini and Hochberg (1995). This procedure is equivalent the the family-wise error rate when all hypothesises are true, but smaller otherwise, thus increasing the degree of statistical power in hypothesis testing when the outcome is not known a priori. A caveat here is that this FDR method is designed for statistically independent tests; however, we apply the method to testing results at grid cells that within some domain have non negligible spatial correlations and thus, are not independent. The implication of this is the loss of added statistical power of results through spatial correlations, practically meaning, that some locations with a statistically significant result, will be treated as a false positive discovery, and hence not stippled. So in effect, the fact that the data are often not independent is not a detriment, and in this case, actually serves to make the results more robust and stippled locations more meaningful. For reference, we show versions of each figure

in the supplementary material that in terms of absolute changes rather than relative changes.

The approach used here of assessing the anthropogenic effects on the 100 year return levels using both frequency- and magnitude-based methods has a distinct advantage. While the two methods are measuring changes to the same quantity, i.e. the 100 year return level, the way in which it is being done is inherently different, thus making the methods related, yet independent. Because the two methods are distinctly different from each other, we can apply two independent methods of significance testing, that is, the binomial testing and the direct calculation of P-values from the null distribution. Thus, grid locations which show statistically significant changes (hatched locations) to the 100 year return level from both the frequency- and magnitude-based methods reinforce their respective results and the significance of the alternative hypothesis: that human activities have altered the occurrence and magnitude of extreme events.

2.5 Results and Discussion

We present our results in order of increasing time-scale, that is, from 1-day maximums to season totals. Figure 2.1 panels (a),(c),(e) show the results for the estimated anthropogenic effect on 1-day maximum precipitation for the NDJFM period spanning 1960-2018. Figure 2.1(a) shows a largely coherent signal of an increased risk ratio across most of CONUS. Along the Pacific west coast, statistically significant locations have a spatial structure which is predominantly oriented along the

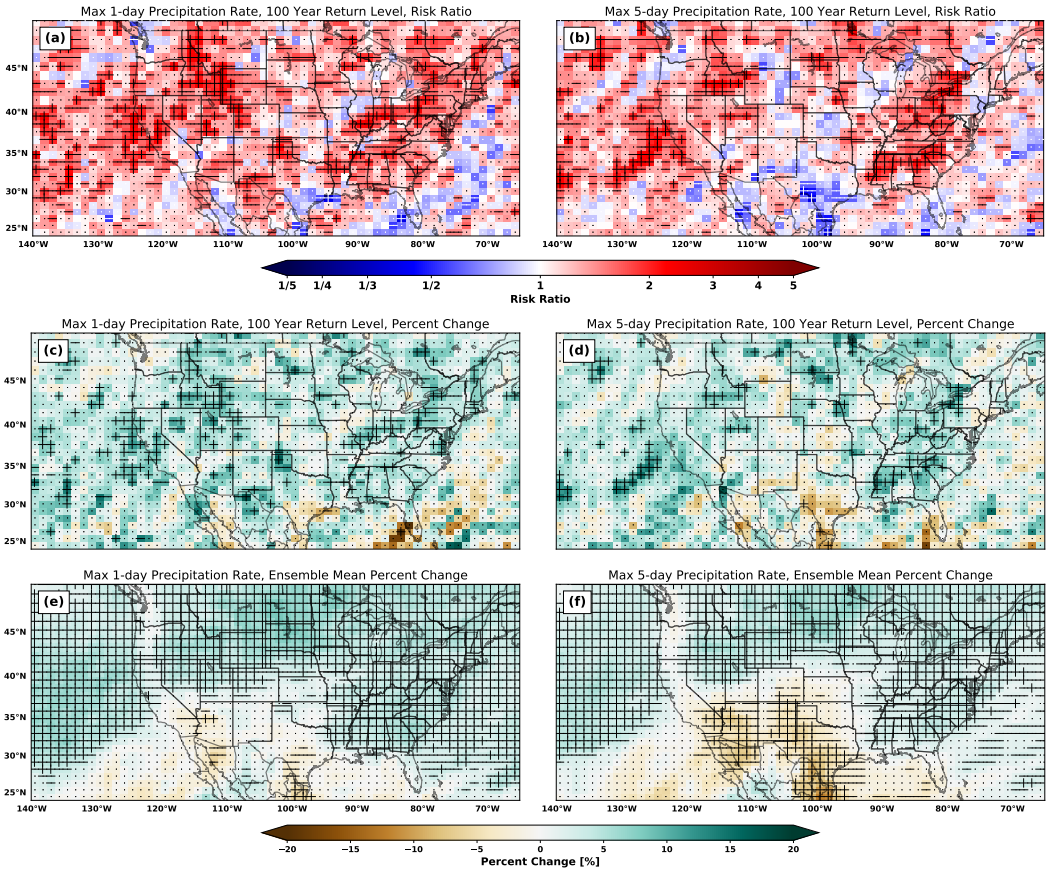

Figure 2.1: Panels (a) and (c) display the 100 year return level risk ratio, and the percent change in the magnitude of the 100 year return level, respectively, for maximum NDJFM 1-day precipitation. Panels (b) and (d) as in panels (a),(c) but for maximum 5-day total precipitation. Panels (e) and (f) show the ensemble mean difference in maximum 1-day precipitation and maximum 5-day total precipitation respectively. In all panels, statistical significance is denoted with a $(-)$ for medium confidence ($p \leq 0.1$), and a $(+)$ for high confidence ($p \leq 0.01$). For clarity of viewing, in panels (a) and (b), stippling is colored either black or white for positive/negative changes in the risk ratio.

southwest-northeast axis suggesting that wintertime daily extreme rainfall has likely been most closely associated with atmospheric rivers (ARs) (Rutz et al., 2014). As the risk ratio is a frequency-based metric, it shows that probability of occurrence of extreme daily rainfall along the U.S. west coast, and in particular, California was made roughly twice as likely due to anthropogenic forcing. This is also true of the inter-mountain west as well as the Appalachia region in the Eastern U.S. Figure

2.1(c), shows the change in the magnitude of 100 year return level for maximum 1-day precipitation. Overall many of the same coherent structures are observed, with the overall direction of change toward larger 1-day rainfall rates. Areas which show statistically significant changes in both Figure 2.1(a) and (c) together imply that these areas experienced extreme daily rainfall rates more frequently and of a larger magnitude than would have occurred without anthropogenic forcing. In the case of California, where the spatial structure of the changes are suggestive of AR activity, then this would imply a greater number of AR days occurred, which were associated with heavier precipitation than would have occurred in a climate without human interference.

Figure 2.1 panels (b) and (d) show the results for maximum 5-day precipitation. In many ways, some of the same spatial structure is present as in panels (a) and (c), but with some loss of signal across the central plains and southwest desert regions. However, at this time-scale, along the west coast, the spatial structure of the changes are arguably more coherent and filamentary-like, again suggestive that the primary driver of the signal in this region is AR activity. A broad feature of risk ratio maps versus the percent change maps, at both the 1- and 5-day time scales, is a higher occurrence of statistically significant results (i.e. stippled grid cells). This could potentially be due to several reasons. First, it could be that anthropogenic forcing has a larger effect on the frequency of occurrence of extreme rainfall rather than the its magnitude. Second, it may be rooted in the nature of the statistical testing itself, that is, using a parametric distribution in testing for the risk ratio versus the calculated nonparametric distribution in testing the change in the magnitude. Al-

ternatively, this could be due to the changes in magnitude of the 100 year return level being below the threshold for detection given the signal-to-noise in the large ensembles.

Figure 2.1 panels (e) and (f) show the ensemble mean change for 1- and 5-day max precipitation rates respectively. At both time scales there is a broad coherent spatial pattern exhibiting a north-south dipole. Over the greater portion of CONUS, there is a statistically robust signal positive changes in both 1- and 5-day maximum rainfall. This practically implies that, on average, the heaviest daily rainfall rates experienced over the NDJFM period spanning 1960-2018 were approximately 7-10% heavier than they would have been had they occurred in a natural climate setting. However, the southwest shows a different mean pattern, namely that anthropogenic forcing has had the effect of, on average, reducing the heaviest rainfall rates, and in particular for the 5-day time scale. The broad, large-scale structure of the pattern is suggestive of an environment of increased stability and descending air motion. This would be consistent with, and thus perhaps caused by, the finding that the response of the Hadley circulation to anthropogenic forcing is to expand northward from the sub-tropics (Held and Soden, 2006, Medeiros et al., 2015).

The difference in wintertime global mean temperature between the All- and Nat-hist simulations is 0.75/°K. Thus for the 100-year max 1-day precipitation (Figure 2.1 panel c), which shows a change of 8% at statistically significant locations, the scaling with temperature is 11%/°K. This then suggests that 1-day extreme precipitation scales at a super Clausius-Clapeyron (CC) rate. The ensemble mean scaling of 1-day max precipitation (Figure 2.1 panel (e)) at statistically significant

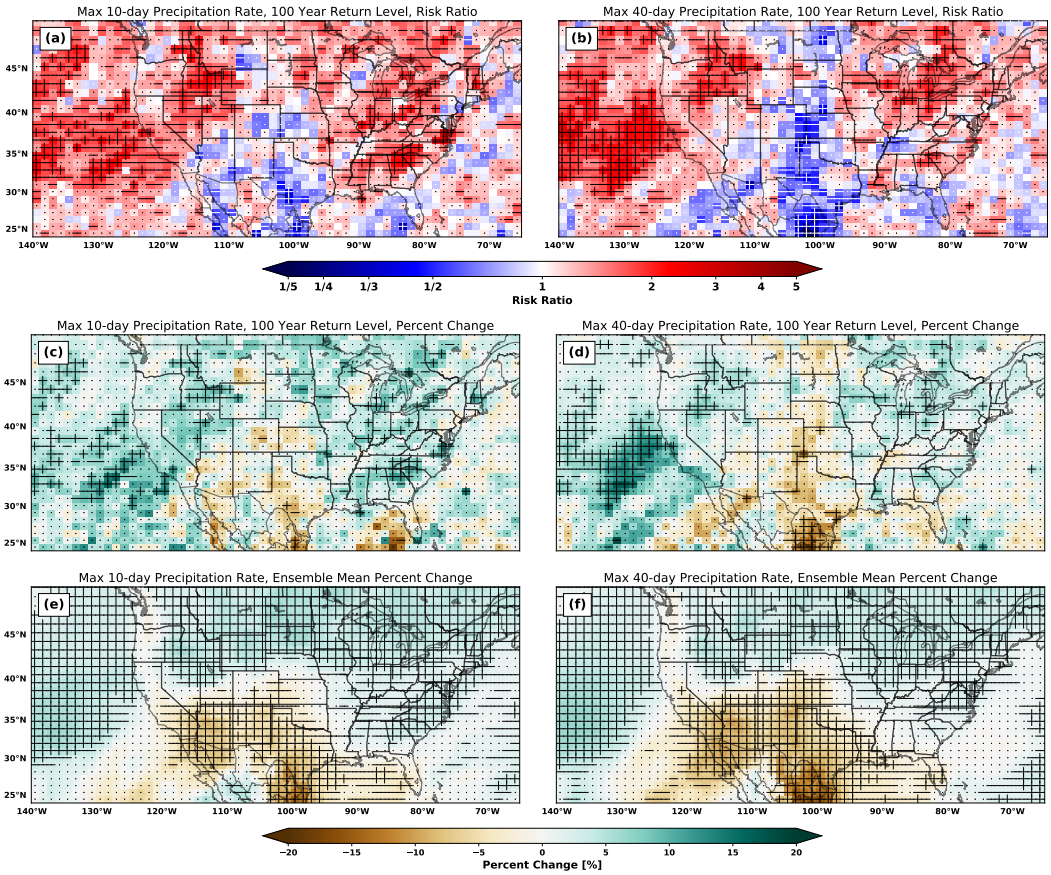

Figure 2.2: As in Figure 2.1, but for maximum 10-day total precipitation (panels (a),(c),(e)), and maximum 40-day total precipitation (panels (b),(d),(f)).

locations is 6%/°K meaning that, on average, max 1-day precipitation scales at a rate commensurate with CC scaling.

At the 10 and 40-day time scales shown in Figure 2.2, many of the same distinguishing spatial structures can be seen as in the 1- and 5-day time scales. Perhaps most striking is the more pronounced pattern of what appears to be signatures of AR activity off the west coast. Seen in risk ratios of Figure 2.2 panels (a) and (c), the AR signature shows a strong development from the 10- to the 40-day time scale. Because the risk ratio is a frequency-based metric, panels 2.2(a) and 2.2(b) reflect changes in the number of occurrences of events exceeding the Nat-hist 100 year re-

turn level for cumulative precipitation within the respective time frames. This then suggests an increase in the cumulative occurrence of AR days in those time spans, practically meaning that anthropogenic forcing has increased the frequency of sequential (back-to-back) AR events. ARs can be highly beneficial "drought busters" bringing precipitation to the west coast and filling reservoirs for human and agricultural use (Dettinger, 2013). However, occurrences of consecutive ARs can quickly waterlog the ground, causing copious runoff, which in turn can overwhelm and damage roads, infrastructure, and water management systems. A recent example of an instance like this was the 2016/17 water year, where California received near record annual precipitation, 90% of which was received in only nine storms, four of which occurred sequentially within a time frame of approximately 40 days (OBrien et al., 2019, Vano et al., 2019). One of the most notable consequences of this was the rapid filling of Oroville reservoir and the subsequent over-topping, which severely damaged the dam spillway causing over $200 million in damages and the evacuation of over 200,000 down stream residents (Vahedifard et al., 2017, OBrien et al., 2019, Vano et al., 2019). Figure 2.2 panels (a) and (b) show over a twofold increase in the probability of 10/40-day cumulative precipitation exceeding the 100 year return level as a result of anthropogenic forcing. OBrien et al. (2019) used observational data spanning 1900-2017 and found an increasing trend in maximum 40-day total precipitation within the Oroville reservoir watershed. Similarly, Swain et al. (2018) used a coupled model large ensemble forced by RCP8.5 and found approximately a 400% increase at end of century in the relative change of 40-day wet extremes at the 200 year return level. So the result here suggests that anthropogenic forcing may

likely be responsible for driving the trend in 40-day cumulative precipitation found by OBrien et al. (2019), and that this trend may continue, and perhaps amplify, into the future (Swain et al., 2018).

Seen in Figure 2.2 panels (c) and (d), not only has the probability for the occurrence of days exceeding the 100 year return level increased as a result of anthropogenic forcing, but the magnitude of such events has increased as well. For 10-day, but more so 40-day total precipitation, this increase is mostly limited to the west coast. Taken together with the risk ratio results, this suggests that the extreme periods of extreme rainfall experienced across the west coast were made both more probable and of a greater magnitude than would have occurred in an unforced climate. Figure 2.2 panels (e) and (f) show the ensemble means of the 10- and 40-day metrics. As in Figure 2.1 panels (e) and (f), the spatial signal is organized as an approximate north-south dipole and is remarkably coherent and more pronounced at these longer time scales. For the southwest, this implies a persistent inhibition of daily rainfall causing the 10- and 40-day accumulations to fall 3-6% below what they would have in an climate without human forcing. While for the northern half of the country, average maximum accumulations and the 10- and 40-day time scales have been made 3-7% larger due to human activities.

Figure 2.3 shows in the left column the mean precipitation rate on days when it is raining, taken to be when model precipitation is greater than or equal to 1 mm/day. This measure is equivalent to the simple daily intensity index (SDII) discussed in Zhang et al. (2011) and henceforth will be abbreviated as such for coherence in the literature. In the right column of Figure 2.3 is the max continuous wet period, de-

fined to be the longest continuous stretch of days during the NDJFM period where model precipitation is equal to or exceeds 1 mm/day, denoted CWD (consecutive wet days) as in Zhang et al. (2011). Figure 2.3 panels (a) and (c) show a pronounced anthropogenic effect on SDII with largely ubiquitous positive changes for both the risk ratio and the change in the magnitude of the 100 year return level. Figure 2.3 (a) shows that when it rains, the probability of experiencing a rain rate equal to or exceeding the 100 year Nat-hist return level has been approximately doubled across nearly all of CONUS. Similarly, Figure 2.3 (c) shows that when it does rain, the most extreme rainfall rates at the 100 year return level are greater by about 3-9% at statistically significant locations. The ensemble mean change in SDII, Figure 2.3 panel (e), shows a coherent and uniform pattern of increase across nearly all of CONUS averaging 3.5% at stippled locations. This then implies that the average rain rate across CONUS scales at approximately 5%/°K, slightly less than CC scaling. Contrasting that with Figure 2.3 panel (c), which shows the change in the 100 year return level, or equivalently, the 99$^{\text{th}}$ percentile of SDII, shows an increase of 6-7% averaged across all statistically significant locations, suggesting then that extreme precipitation, on average, scales at super CC rate of 8%/°K.

The right column of Figure 2.3 shows the maximum continuous wet period (CWD). Panel (b) shows spatially coherent marked decreases across the southwest and along the eastern seaboard, albeit mostly lacking statistical significance in the latter. Locations across the southwest region show decreases in the probability of exceeding the 100 year return level of maximum CWD of 0.3 and 0.4 averaged at locations statistically significant at $p \leq 0.01$ $(+)$, and $p \leq 0.1$ $(-)$, respectively. Note

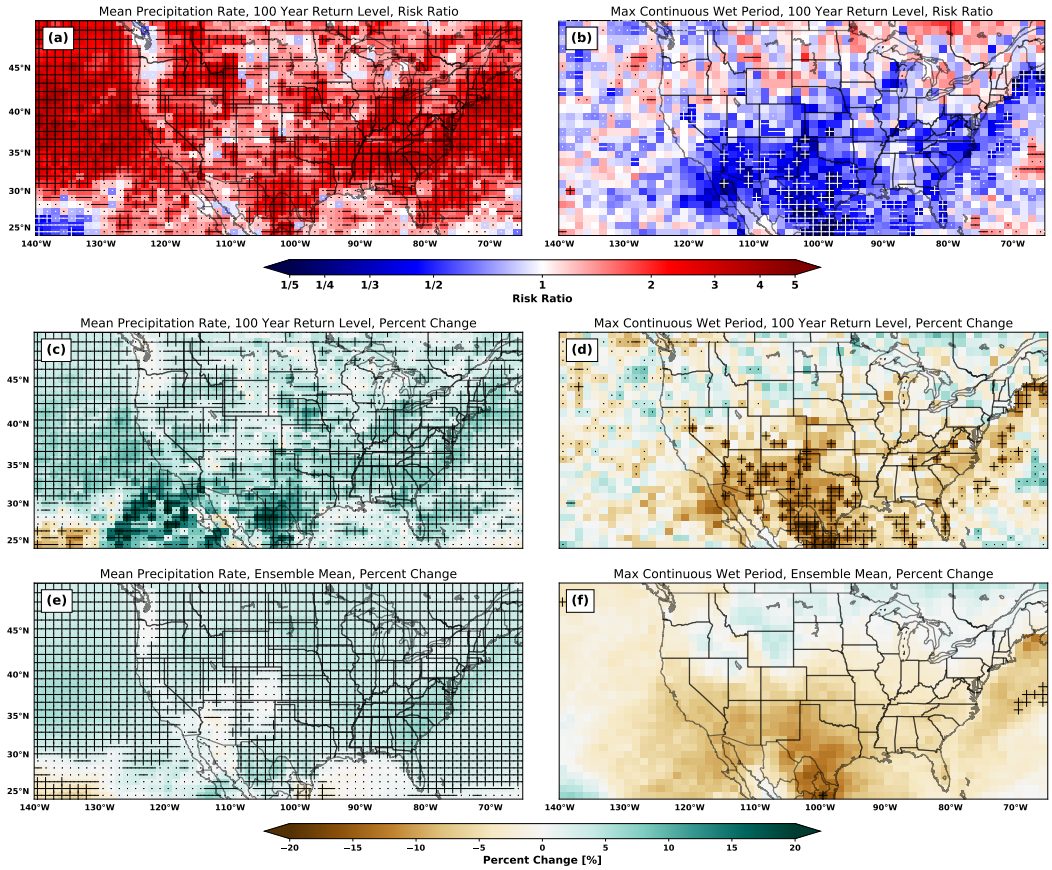

Figure 2.3: As in Figure 2.1, but for the mean precipitation rate on rainy days (precipitation $\geq$ 1 mm/day) (panels (a),(c),(e)), and the maximum continuous wet period (panels (b),(d),(f)).

that for decreases in the risk ratio, a change of 0.3 is larger than a change of 0.4, since on this scale, 1.0 represents the point of no change. Thus, for the statistically significant locations across CONUS, which are predominantly found in the southwest, the probability of exceeding the simulated maximum CWD length at the 100 year return level has decreased by approximately 70% as a result of anthropogenic forcing. The ensemble mean change in maximum CWD shown in Figure 2.3 panel (f) shows no statistically significant locations over CONUS. Given the changes observed at the 100 year return level shown in panels (b) and (d), this implies that for CWD, the mean of the distribution is left relatively unchanged, and that the effects

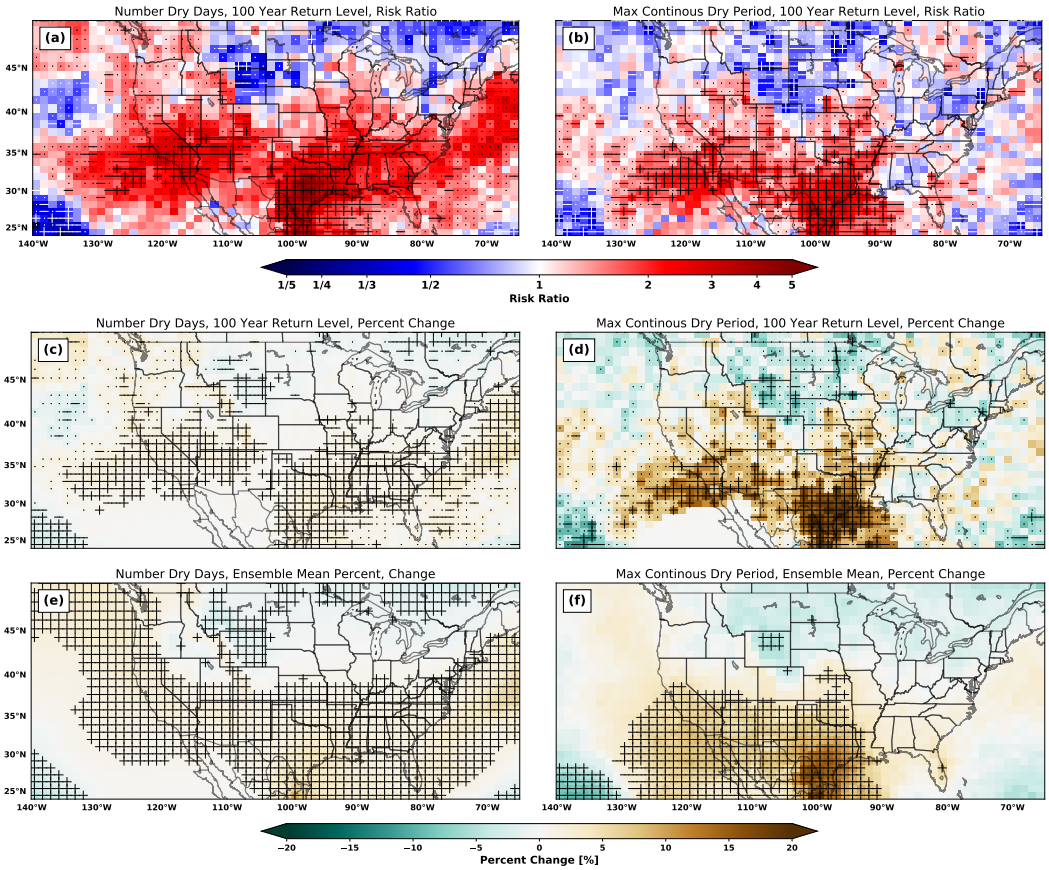

Figure 2.4: As in Figure 2.1, but for total number of dry days (panels (a),(c),(e)), and the maximum continuous dry day period (panels (b),(d),(f)). Note that the colorbar has been flipped here to indicate that increases in the index are associated with drying.

of anthropogenic forcing are concentrated in the tail of the distribution, manifest only in the extremes of maximum CWD.

Figure 2.4 shows results for the total number of dry days over the NDJFM period (NDD) and the maximum continuous dry day (CDD) period over the same time frame in the left and right columns respectively. Note that the colorbar has been reversed here to indicate increases in the metrics corresponding to drier conditions. Panel (a) shows an overall increased risk, with statistically significant locations centered over southern California and Texas. In particular, over Texas, the risk of an

increased occurrence of dry day frequency over the winter period is elevated by a factor of 4 due to anthropogenic forcing. Panel (b) shows that the risk of exceeding the 100 year return level for the maximum continuous dry period is elevated as well. Contrasting panels (c) and (d) shows a different picture however, such that there is only a modest increase in the change in the number of dry days at the 100 year return level but a relatively strong signal in the length of the maximum CDD period. This suggests that for the most part, dry days have been made to become more likely to group together, with longer periods of time between being punctuated by a rainy day. Indeed, taking this result, and that of Figure 2.3 panels (c) and (e) suggest that, in particular for the southwest, an overall increased risk that dry periods last longer and when they end, they end on average with a more extreme rain event than would have occurred in an unforced climate. This reflects an overall amplification of the hydrologic cycle, that is, longer deeper dry spells, punctuated by shorter more intense rainfall. Supplementary Figure B.4 panel (d) shows the difference in the length of the CDD period, and over Texas, there is an increase upwards of 10 days in the length of extreme CDD spells relative to an natural climate.

The ensemble mean change in the number of dry days, Figure 2.4 panel (e), shows a large spatially coherent swath of statistically significant signal from the eastern seaboard, stretching across the south and southwest and up through California and along the Pacific Coast. This uniform signal represents an increase in NDD of approximately 2%. The ensemble mean for CDD, Figure 2.4 panel (f), on the other hand show a substantial increase across the stippled locations averaging 12-13%. The difference in the strength of these two metric could be reflective of

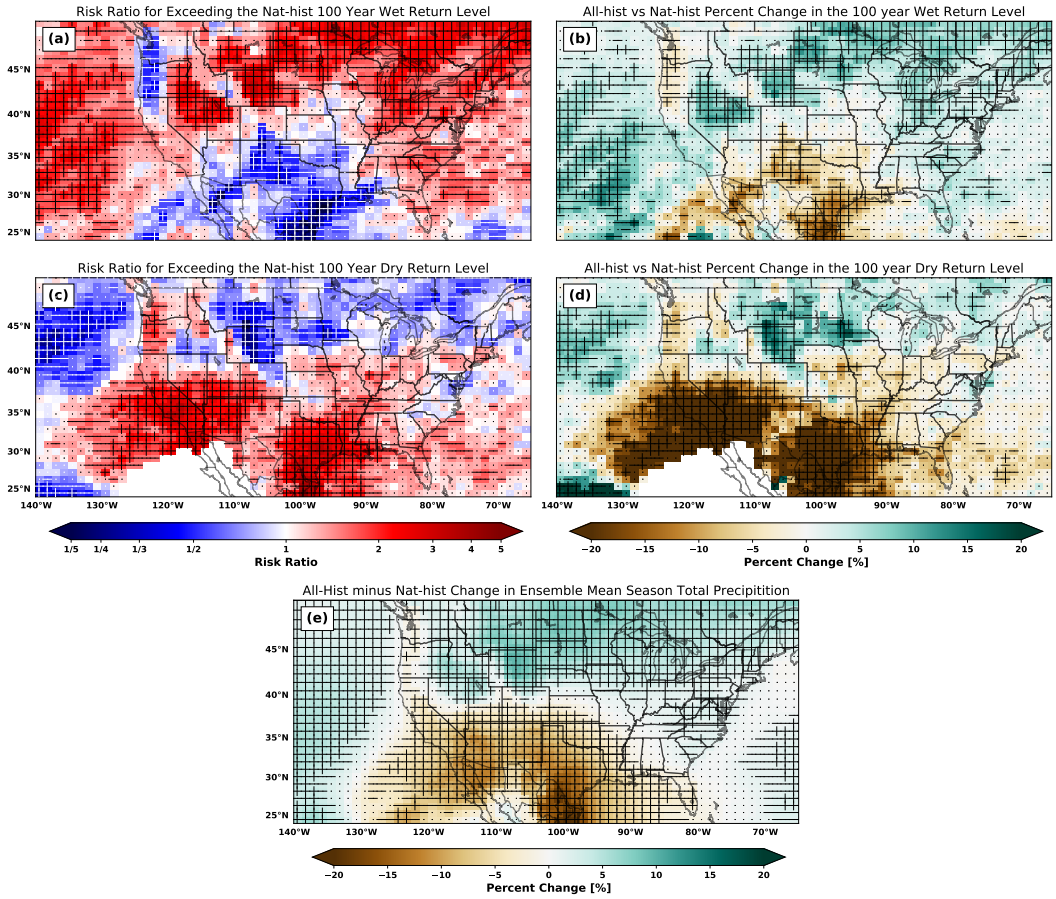

Figure 2.5: Panels (a),(b) show the risk ratio and the percent change in the 100 year return level for wet season precipitation totals. Panels (c),(d) as in panels (a),(b) but for dry seasons precipitation totals. Panel (e) shows the percent change in the ensemble mean season total precipitation. Statistical significance stippling is as in Figure 2.1

.

the persistence of large-scale patterns having been amplified, that is, large-scale patterns which inhibit rainfall in the southwest tend to last longer in an anthropogenically forced climate. This type of behavior in large-scale wave patterns is an area of very active research has been documented by a number of studies (Barnes et al., 2014, Mann et al., 2018, Francis and Skific, 2015). However, it should be noted that this type of large-scale behavior also has the ability to drive persistent precipitation extremes as well (Hoskins and Woollings, 2015, Du et al., 2019).

Figure 2.5 shows the anthropogenically forced changes to season total precipitation across CONUS. Panel (a) shows the risk ratio for exceeding the 100 year Nat-hist wet season return level. Several notable features stand out, in particular over the southwest and the Pacific northwest, which both show a marked decrease in the risk ratio. This implies that the probability for experiencing extremely wet winter seasons has decreased in these regions due to climate change. Panel (b) shows the change in the magnitude of the 100 year wet season return level and shows an overall similar spatial pattern of change, with drier extremely wet seasons corresponding with the decreases frequency. This implies that wettest winter seasons in the Pacific northwest and the southwest, would likely have been wetter in a climate without human interference. On the other hand, a large portion of the northern great plains and eastern regions of CONUS sees the opposite effect, an increase in the probability and magnitude of extremely wet winters.

Panels (c) and (d) of Figure 2.5 shows the anthropogenic effect on the 100 year return level for dry season totals. To a large extent, the spatial patterns and directions of change mimic those shown in panels (a) and (b). This is because they are reflecting changes to the same distribution but on opposite tails, however the changes are not always symmetric. For example, in the Pacific northwest, panel (a) shows a decrease in risk for extremely wet winters and in panel (c), a commensurate increase in the risk for very dry winters, suggesting a uniform shifting of the precipitation distribution to overall dryer conditions. In southern California there is an increased risk for both extreme wet and dry winters, indicating a widening of the distribution. However, the increase in the risk of dry winters is greater, suggesting

the extension of the dry tail of the distribution is greater than the wet tails extension into wetter conditions. Panel (d) shows the anthropogenic effect on the magnitude of very dry winters, and the most coherent signal is again across the southwest extending into southern and central California [1]. This shows that in Texas for example, extreme dry winters, like that experienced in 2011, would have likely been exacerbated by anthropogenic forcing. Numerous studies have sought to assess the role human activities played in driving that particular event, and while there is a strong anthropogenically forced fingerprint on temperature, the degree to which human activities altered precipitation that year is largely uncertain due to the high degree of internal variability and apparent ocean forcing (Deser et al., 2014, Seager and Hoerling, 2014, Hoerling et al., 2013). Recall that in this study variability arising from the ocean has largely been removed in the differencing process as both the All- and Nat-hist experiments share much of the same ocean variability. Therefore it is possible that the anthropogenic signal observed in this study may still be below the detectable limits in observations given natural variability.

Panel (e) shows the ensemble mean change for the anthropogenic effects on season total precipitation. The two spatially coherent signals are that of a predominately north-south dipole with an extension of the drying signal extending up along the west coast. This shows that for the southwest and for the west coast, that the net anthropogenic effect is to favor drier winters overall despite increased rainfall at shorter timescales, especially for California. Figure 2.3 shows that for both Cali-

[1] Note that the area of missing data centered over Baja California in Figure 2.5 panels (c) and (d) is due to the 100 year dry season Nat-hist return level in this region equaling zero, that is, no precipitation falls during the winter season, thus the relative change is undefined.

fornia and Texas, that anthropogenic forcing drives more intense rain rates on days it does rain. However, the increase in precipitation intensities are not enough to offset the increased occurrence of dry days (Figure 2.4). For the northern half of the CONUS and the northeast/Appalachia regions, anthropogenic forcing favors wetter winters overall. Across the range of timescales, the anthropogenic effect is to largely favor increased rain rates in these regions (Figures 2.1, 2.2, 2.3). However, unlike the southwest and the west coast, the increase in dry day occurrence does not offset the increase in precipitation intensities across timescales. Thus the cumulative effect of anthropogenic forcing in the north/northeast regions of CONUS is to favor overall wetter winters, with higher rain rates, across all timescales.

2.6 Conclusions

The goal of this study is not to do event attribution on any single event, but to attempt to assess, understand, and quantify the cumulative effects of anthropogenic forcing on the observed winter hydrometeorology, using a number of different societally relevant metrics, across the U.S. from 1960-2018. Whether the anthropogenic effects observed in this study are detectable in the observations is not the focus here, however, as documented in Section 2.2, changes in both observed mean and extreme precipitation, across a range of time scales, have been documented in many studies and thus it is plausible that the aggregated anthropogenic effects documented here could be playing a role in driving changes in the observations. Another way to think about the results here is that the relative changes found do not have to necessarily

agree with observed trends, rather these results would indicate in which direction anthropogenic forcing is "nudging" the observed trends. For example, for the south climate region, which encompasses Texas and the southern plains, the data show NDJFM total precipitation increasing at a rate of 3 mm per decade (NOAA National Centers for Environmental information, 2019). Thus given the findings here, its possible that due to anthropogenic forcing that that trend may be suppressed relative to what it may have been in a climate without human interference. Also, clearly evident the time series for the south region is significant decadal-scale variability, which could potentially be masking anthropogenic nudging to the observed precipitation trend (NOAA National Centers for Environmental information, 2019).

The main findings of this study are as follows:

- Extreme daily rainfall counts above the 100 year return level were twice as likely in the the All-hist simulations than in the Nat-hist simulations across a large portion of CONUS (Figure 2.1(a)). Additionally, the simulated magnitudes of those events were 7-10% larger than in naturally forced simulations (Figure 2.1(b)).

- Along the west coast, increases in the frequency and magnitude of extreme rainfall at timescales ranging from 1- to 40-day appear to be related to an increase in AR activity and strength. At the 10- and 40-day timescales, the spatial structure of change and the risk ratio suggest that the change in magnitude of the 100 year return levels appears to likely be the result of a greater number of AR days, thus implying an increase in the probability in the occurrence of sequential AR events (2.2).

- The ensemble mean change in SSDI (average rain rate on days it rains), shows a broad and coherent signal across nearly all of CONUS implying that due to anthropogenic forcing, when it rains it rains harder. The simulated increase in the mean precipitation rate is 3.5% implying that mean precipitation scales at a rate commensurate with Clausius-Clapeyron.

- Given that there is approximately a 0.75°K difference in warming between the All- and Nat-hist simulations, the rate of increase of SDII per degree of warming is then roughly 6%, in line with the increase of atmospheric water vapor holding capacity of 7%/°K described by Clausius-Clapeyron.

- The changes at the 100 year return level (99^{th} percentile) of extreme precipitation across all timescales is observed to increase at a rate of 6-9%, suggesting that extreme precipitation scales at a super Clausius-Clapeyron rate.

- For the statistically significant locations across CONUS, which are predominantly found in the southwest, the probability of exceeding the length of the Nat-hist simulated maximum continuous wet period at the 100 year return level has decreased by approximately 70% as a result of anthropogenic forcing.

- The moderate increase in the number of dry days relative to the larger increase in the maximum continuous dry day length suggests that anthropogenic forcing increases the probability of dry day grouping. This suggests that anthropogenic forcing produces an aggregated effect such that on average, dry periods are longer and ended with more intense rainfall event.

- The ensemble mean change in NDJFM total precipitation is that of a north-south dipole over CONUS. In the southwest, as well as the Pacific northwest, the simulated aggregated effects of anthropogenic forcing has been to suppress winter precipitation resulting in, on average, drier winters than might have otherwise occurred in an unforced climate. In the northern half of CONUS, stretching from the inner-mountain west to the east coast, simulated total winter precipitation was on average 4-5% larger than in the naturally forced simulations.

Our results suggest there has been an appreciable anthropogenic effect on the observed hydrometeorology across CONUS from 1960-2018. These results are derived from two large ensembles of simulations each totaling 2950 simulated years and each sharing the same ocean variability. The combination of effectively controlling for ocean variability as a driver of precipitation change and the large number of simulated years giving a good sampling of non ocean-forced internal variability, together the two ensembles allow for a controlled estimation of the anthropogenic signal. That we only have one realization of the observed climate, imbued with high internal variability, detecting the anthropogenic signals found here in the observations may be not be possible, however, in the future with improved signal-to-noise, these changes should become detectable. Our results show that anthropogenic forcing had about a twice as large effect on the extremes, at all timescales, than on the mean of any of the fields considered here. This suggests that if an anthropogenic signal were to be detected in precipitation observations, it would likely first be observed in the extremes. This implies that the documented trends in observed precip-

itation extremes, which have been attributed to human activities, are unlikely to be an artefact or a result of ocean forcing or internal variability.

Our findings on the anthropogenic effects for the various different metrics studied here are broadly consistent with the observed changes to date and with the expected anthropogenic effects found in future climate projections. The figures in Alexander et al. (2006) provide a comprehensive view of the observed changes to date of the ETCCDMI indices used in this study. Likewise, Sillmann et al. (2013) provide the same comprehenseve analysis for the same indices, but for model output making up the CMIP experiments. For example, SSDI daily intensity shown in Figure 2.3 shows a remarkably consistent spatial signature compared with the Figure 6 in Alexander et al. (2006). Additionally, considering the max 5-day precipitation rate and the CCD, both Alexander et al. (2006) and Sillmann et al. (2013) good correspondence meaning that the changes found here are indeed being documented in observational record and that they are consistent with anthropogenic forcing.

We have found that for most of the precipitation-based indices, that the extremes at the 100-year return level appear to be scaling at a super CC rate of approximately 10-12%. While the ensemble mean fields of the of these variables tend to scale at or below CC scaling 3-6%. This result is in line with the idea that the heaviest rainfall events occur when nearly all of the moisture in a volume of air is precipitated out. Therefore, the intensity of these events would scale at minimum with the availability of moisture and hence events occupying the uppermost quantiles to be constrained to increase with Clausius-Clapeyron. Change of this type would represent a lower-bound on extreme precipitation as enhanced convergence driven

by latent heating would serve only drive higher precipitation rates leading to super Clausius-Clapeyron scaling (Pall et al., 2007). Overall our results show that many of the changes documented to various types of meteorological extremes are consistent with and most likely due to anthropogenic forcing.

This page left intentionally blank.

Chapter 3

The Anthropogenic Contribution to Observed Hydrometeorological Variation and Predictability

3.1 Introduction

The U.S. west coast, and in particular California, is a region well-known to exhibit high wintertime precipitation variability (Dettinger, 2011). In California, this was recently exemplified by the rapid reversal of a deep and extended drought lasting from 2011-2015 (Wang et al., 2014, Seager et al., 2015). The following winter of 2015/16 featured one of the strongest El Niño events in the observed record where the tropical east Pacific sea surface temperature anomaly (SSTA) in the Niño 3.4 region reached its reached the highest value ever recorded (NOAA National Centers for Environmental information, L'Heureux et al., 2017). Historically, California has

had a strong perceived relationship with strong El Niño events and extremely wet winters, this notion is primarily validated by the extremely wet El Niño winters of 1983 and 1998, despite over the observed record El Niño only accounting for about 7% of the precipitation variability in California (Savtchenko et al., 2015, O'Brien et al., 2019). However, the extreme El Niño of 2015/16 failed to deliver much more than California's historical average precipitation that year (Paek et al., 2017, Lee et al., 2018). The following winter of 2016/17, tropical east Pacific SSTAs returned to neutral conditions thus giving little expectation of receiving the much needed precipitation that would relieve the extreme drought conditions that persisted throughout the previous winter. In spite of any obvious strong oceanic or atmospheric forcing, the California winter of 2016/17 ended to be one of the wettest winters on observational record, and in many locations, far surpassing rainfall accumulations recorded during the strong El Niño years of 1983 and 1998 (Wang et al., 2017, OBrien et al., 2019, Vano et al., 2019). The occurrence of back-to-back years where the wintertime precipitation outcome was counter to what was expected challenged the long-held view of the El Niño - California precipitation relationship and what large-scale circulation patterns were capable of producing extremely wet winters in California.

The winter rains of 2016/17 ended California's long standing drought conditions and filled nearly every reservoir to capacity for the summer months to come. However, along with that came severe flooding, mudslides, and critical infrastructure damage, most notably, the Oroville dam spillway which resulted in over $200 million in damage and the evacuation of over 200,000 down stream residents (Vano

et al., 2019, OBrien et al., 2019). Water management officials rely on accurate and informative seasonal forecasts to properly manage reservoir levels and prepare for the possibility of extreme rainfall in order to mitigate flood risks and downstream property damage. Winters such as those of 2015/16 and 2016/17 not only present a major challenge to water resource managers, but also agricultural, municipal, and humanitarian sectors as well (Kunkel et al., 1999). Extreme rainfall, or lack thereof, stresses human and environmental systems and can either be a boon or a detriment depending on how and when rainfall is received (California Department of Water Resources, 2017). For example, extreme rain following multiple years of drought falls on parched earth, where the ground has developed hydrophobic tendencies, can cause rapid runoff leading to flash flooding (Burch et al., 1989). Similarly, persistent rains, or sequentially occurring events, can lead to soil that exhausts its infiltration capacity, generating more runoff than would be expected for the equivalent event occurring isolated from antecedent conditions (Burch et al., 1989). On the opposite extreme, multiple seasons of below average rainfall can deplete groundwater storage, causing a non-recoverable loss of primary porosity, thereby exacerbating amplifying agricultural and hydrological drought in future meteorological droughts (California Department of Water Resources, 2017). Thus, it is not so much trends in mean precipitation that are particularly stressful, it is more the variability about those trends, present or not, that cause the greatest impacts to human and environmental systems.

Despite the vast body of literature on trends in mean precipitation and extremes across a range of time-scales (e.g. Trenberth (2011) and references therein), precip-

itation variability has been less thoroughly studied. Seager et al. (2012) undertake a comprehensive study using precipitation minus evaporation (P-E) variability as a proxy for hydroclimate variability. They use the CMIP3 archive to quantify warming induced changes to P-E variability and find that globally and on the annual time scale, P-E variability does increase nearly everywhere, in some regions by as much as 40%. In addition, they isolate the δP-E signal due to the El Niño Southern Oscillation (ENSO), the largest source of global circulation variability, and find that ENSO driven P-E variability generally increases over the tropics with mixed sign changes elsewhere. However, notably, their results indicate a decrease in ENSO driven P-E variability over most of the continental Unites States (CONUS). However, because the authors consider ENSO driven P-E changes by assessing the difference between the cold and warm ENSO phases, La Niña and El Niño respectively, their respective contributions to P-E variance are conflated, and thus it is unclear which phase has the greater contribution to future changes in ENSO driven P-E variance. Considering ENSO phase differences is useful for comparing their relative impacts and remote circulation responses; however, because La Niña and El Niño are not symmetric phenomena and are controlled by very different ocean and atmospheric dynamics, assessing their differences for quantifying future changes in P-E variability assumes that a warming climate will affect their respective dynamics equally. While fundamentally they are both part of the same large-scale circulation, their associated individual dynamics and remote responses are highly asymmetric (Philander, 1985, Hoerling et al., 1997, Burgers and Stephenson, 1999), and because of this, future changes to ENSO will likely be highly asymmetric as well.

Another interesting aspect to this study is the individual treatments of the dynamic and thermodynamic components to changes in P-E variability. While a large fraction of the Earth experiences an increase in P-E variability in response to warming, there are also regions that do not. Precipitation variability scales with changes in specific humidity since equivalent circulation anomalies in a warmed climate will create larger moisture convergence owing to the increase atmospheric water vapor content. However, despite a uniform global increase in specific humidity in a warmed climate, there are regions that show decreases in P-E variability. To first order, precipitation is the product of specific humidity and vertical velocity (Emori and Brown, 2005, O'Gorman and Schneider, 2009, Rauscher et al., 2016, O'Brien et al., 2016), hence a change in vertical velocity variance will manifest as a change in precipitation variance. Concomitant with a largely uniform increase in global specific humidity in a warmed climate is also a largely uniform decrease in 700-hPa vertical velocity variance. Areas which show decreasing P-E variability yet increasing specific humidity are regions where the decrease in vertical velocity variance outweighs the increase in specific humidity. A notable region that exhibits this behavior is the U.S. southwest. Perhaps most interestingly though is the opposite case, where both specific humidity and vertical velocity variance increase. In a future warmed climate, these regions would be characterized by a climatology which exhibits large interannual fluctuations in both storm intensity and frequency, in other words, a climatology displaying high interannual precipitation volatility. Outside the polar regions, only two regions display concomitant increases in both specific humidity and interannual vertical velocity variance: the tropical east Pacific

and the U.S. west coast. This suggests then that it is possible that human induced climate change thus far may be playing a role in fueling the high interannual precipitation variability and volatility experienced in the western U.S. (Swain et al., 2018, Gershunov et al., 2019).

Pendergrass et al. (2017) undertake a similarly ambitious study of future changes in global precipitation variability and find robust increases on the order of 4-5%K^{-1}. Here they use the CMIP5 archive as well as two initial condition large ensembles which show that the largest changes in precipitation variance occur over extratropical land during the boreal winter. They show that the increase in precipitation variability for all regions and all seasons is at least as greater or greater than the increase of the mean precipitation rate. In other words, it appears as if the change in the mean precipitation rate sets a lower bound on the rate of change of variability. Similar to Seager et al. (2012), they attribute this to the combined effect of increasing atmospheric moisture and weakened circulation. Additionally, they find that the increase in precipitation variability with warming is robust and remarkably consistent across timescales ranging from the daily to the 3-year timescale. This shows that the underlying processes responsible for the increase in variability operate at all time scales and thus cannot be attributed solely to longer timescale processes such as ENSO. Finally, they use station observations to show that from 1960-2000, the increase in daily precipitation variability per degree of warming is consistent with the model projected results.

In another study of global station observations, Tsonis (1996) used monthly precipitation records over a 90 year period, modeled with parametric gamma distribu-

tion, and 40-year binning to reveal low-frequency trends in precipitation variability. She found using maximum likelihood estimates of the scale and shape parameters, large positive trends in low frequency (40-year) global precipitation variability. This suggests that precipitation variability is sensitive to variations in global mean temperature. In a similar study, Svoma and Balling (2010) used monthly precipitation data from stations across CONUS which contained at least 40 years of quality controlled data pre- and post- 1950. They parsed out the data by winter and summer seasons and assessed the change in interannual precipitation variability between the two time periods. Overall, the winter season (taken there to be Oct-Mar) showed the greatest change in interannual precipitation variability. Interestingly, the largest changes were observed along the U.S. west coast and in Florida, both regions which show a strong sensitivity to ENSO variability. Because of the different time scales used in the studies of Pendergrass et al. (2017), Tsonis (1996), and Svoma and Balling (2010), together they show that precipitation variability is sensitive to temperature variability across a range of temporal scales with strong expression of modulation by ENSO at the interannual time scale.

Given the findings thus far of changes in precipitation variability documented in the present climate, and those projected for the future climate under continued greenhouse gas forcing, there is strong reason to suspect that anthropogenic forcing is playing a role in driving changes in precipitation variability. However, to the best of the author's knowledge, no study has yet been under taken to assess the anthropogenic contribution to the observed precipitation variability in the present day climate. As such, we address three main questions:

1. How has the observed modification of the global climate system by human activities affected, and to what extent, the observed hydroclimate variability on intra- and inter-annual time-scales?

2. On the global scale, has anthropogenic forcing altered the fraction of total precipitation variance resulting from ocean forced variance?

3. How and where are changes in precipitation variability due to anthropogenic forcing expressed?

3.2 Data and Methods

3.2.1 Data

The data used in this study consist primarily of two large ensembles of climate model simulations. These simulations are a subset of the Climate of the 20th Century and Detection and Attribution project (C20C+) (Folland et al., 2014). Each ensemble member is generated using the CAM5.1 atmospheric model (Neale et al., 2012), initialized with initial condition perturbations and forced with identical boundary conditions. The first ensemble is forced with the observed sea surface temperatures (SSTs) and all historical radiative forcings (the All-hist ensemble), while the second is forced with the observed SSTs with the estimated component of ocean warming and radiative forcing removed (the Nat-hist ensemble). Thus each ensemble shares the same ocean variability, however the Nat-hist ensemble is a best estimate of what the observed climate would have looked like in the absence of hu-

man interference. Each ensemble spans from 1960-2018 and contains 50 members each totaling 2950 simulated years for each ensemble. For a complete description of the C20C+ dataset used here, refer to Chapter 2.4.2. We consider the December through February the following calendar year period (DJF), where northern hemisphere circulations that drive precipitation anomalies largely result from resolved large-scale motions. In places where appropriate, we include the use of ERA5 reanalysis for comparisons of our model-based results to observations (Copernicus Climate Change Service Climate Data Store (CDS), 2017).

3.2.2 Methods

Anthropogenic contributions to the observed precipitation variability are calculated as the residual between the All-hist ensemble, representing the climate as it currently is, and the Nat-hist ensemble, representing the best estimate of the climate as it would have been without human interference. Because both sets of ensembles share the same large-scale ocean variability, that is, El Niños, La Niñas, and ENSO neutral years all occur in the years in which they occurred in reality, changes in precipitation variability cannot be ascribed to differences in ocean variability between the sets of simulations. That said, it is still possible to study the effects of, say, El Niño on precipitation variability within the simulations by isolating the years in which El Niño events occur, which again, are the same between the All- and Nat-hist ensembles.

Statistical significance is ascribed for all fields at the 90% confidence level. For differences in variability between ensemble mean fields, the two-tailed students t-

test is used. For differences in the variability of fields where the ensemble mean has not been taken, the Bartlett test for equal variances is used. The Bartlett test is sensitive to distributions whose shape deviate significantly from that of the normal distribution. In order to test the robustness of the results using the Bartlett test, we also employed the Levine test for equal variances, which is robust to distributions that deviate from normality. The significance results between the two test were qualitatively similar suggesting that overall, the data are close to normally distributed. This was further verified with a Wilks-Shapiro test for normality. All significance test are subjected to the false discovery control rate (FDR) described in Benjamini and Hochberg (1995). This procedure controls for false discoveries, i.e. type 1 statistical errors, in multiple hypothesis testing. For all figures, locations that are statistically significant at the 90% confidence level and have passed FDR control are stippled.

In a large ensemble variability can be defined in one of two dimensions: across time and/or across ensemble members. Variability across time, referred to here as climatological variability, reflects interannual variability, that is, year-to-year variation in the average DJF rain rates calculated locally at each grid cell. On the other hand, ensemble variability refers to the variability across ensemble members within a given year specified by a prescribed ocean state. As such, with respect to the data used in this study, we have 50 ensemble members, which simulate individually 59 years from 1960-2018 at every grid cell of the 1-degree model domain. This then results in an array of shape (50,59,192,288) the sizes of which represent the dimensions of (ensemble member, year, latitude, longitude). From this discrete array we

can now define the various computations used in this analysis, where $P(k,t)$ is the average DJF precipitation for ensemble member k and year t, where T and K are the total number of years and ensemble members respectively. Subscripts indicate operators with respect the indicated variable where overlines and tildes indicate time and ensemble means respectively. Let the ensemble mean of DJF precipitation be then defined as,

$$\widetilde{P}(t) = E_k[P(k,t)] = \frac{1}{K}\sum_{k=1}^{K} P(k,t), \tag{3.1}$$

and the temporal mean as,

$$\overline{P}(k) = E_t[P(k,t)] = \frac{1}{T}\sum_{t=1}^{T} P(k,t). \tag{3.2}$$

Thus the total ocean forced variance, that is, the variance of the ensemble mean is calculated as,

$$\sigma_t^2[\widetilde{P}(t)], \tag{3.3}$$

and the fraction of ocean forced variance as,

$$\frac{\sigma_t^2[\widetilde{P}(t)]}{E_k[\overline{P}(k)]}. \tag{3.4}$$

The climatological variability is then defined as,

$$\overline{\sigma}^2(k) = \frac{1}{T}\sum_{t=1}^{T}(P(k,t) - \overline{P}(k)])^2 \tag{3.5}$$

and ensemble variability as,

$$\widetilde{\sigma}^2(t) = \frac{1}{K}\sum_{k=1}^{K}(P(k,t) - \widetilde{P}(t))^2 \tag{3.6}$$

Thus the average of each ensemble members climatological variability (ensemble mean climatological variability) is defined as,

$$E_k[\overline{\sigma}^2(k)] \tag{3.7}$$

and the temporal mean of ensemble variability as,

$$E_t[\widetilde{\sigma}^2(t)]. \tag{3.8}$$

3.3 Results

3.3.1 Global Changes to Observed Precipitation Variability

On the global scale, precipitation variability arises from two primary sources: ocean variability and internal atmospheric variability. Ocean variability evolves on long timescales, from months to years, and is thus regarded as potentially predictable variability (Koster et al., 2000, Westra and Sharma, 2010). Internal atmospheric variability arises from the inherently nonlinear chaotic dynamics of large-scale fluid motions and thus are not predictable beyond about 10 days (Lorenz, 1969, Deser et al., 2012). However, despite the inherently chaotic nature of atmospheric flows,

there do exist recurrent aspects within the chaotic flows, which are to a greater or lesser extent controlled by the stationary components of the global climate system, such as the relative locations of warm tropical ocean waters to cold polar waters, or the locations of the continents and ocean basins, and mountain ranges like the Himalayas in Tibet and the Rockies in Colorado. Recurrent low-frequency atmospheric variability such as the Pacific/North American Pattern (PNA) and the North Atlantic Pattern (NAO) are expressions of this type of atmospheric behavior. These aspects of the climate system alter the probabilities for the potential downstream outcomes of the atmospheric flow, such that some outcomes are more likely than others. The range of potential outcomes describes the internal variability of the system. To understand the internal variability, or the potential range of outcomes, one must use a large ensemble of simulations that sufficiently characterize the distribution of probabilities associated with each outcome. Thus the mean of a large ensemble represents the response with the highest probability of occurring, known as the forced response, while the trajectory of any individual ensemble member only represents one possible outcome from an infinite number of outcomes. The forced response in any ensemble of simulations is the outcome associated with the forcings and boundary conditions common to all ensemble members. In this study the common boundary condition to all ensemble members (All- and Nat-hist) is the ocean variability, so the variability of the ensemble mean represents ocean forced variability. Thus it is the ocean which is primarily responsible determining the mean of the distribution of outcomes. The width of that distribution, that is, the variability about the mean, is largely controlled by the random component of climate, i.e. the range

of outcomes simulated by any single ensemble member. Thus the greater range of outcomes about the mean implies a lower probability of any one outcome occurring, practically meaning, a decrease in predictability.

Figure 3.1 shows the total variance in average DJF precipitation rate resulting from ocean forcing given by the variance of the ensemble mean calculated as Eq. 3.3. Not surprisingly, the equatorial tropics show the greatest response to ocean forcing. The band of tropical precipitation variance represents the inter-tropical convergence zone (ITCZ), and is shifted north of the equator during the boreal winter. Along the U.S. west coast, in both the All- and Nat-hist simulations, panels (a) and (b), there exists a moderate amount of common variability indicating precipitation variance sensitivity to oceanic conditions. This variance connects to the tropics and highlights a region that is often the source of atmospheric rivers (ARs), specifically of the Pineapple Express variety, which tend to be sourced from regions near Hawaii (Zhou and Kim, 2018). To a lesser extent, in the north Atlantic basin, coastal regions of Portugal, France, and Great Britain show common precipitation variance, most likely stemming from trans-Atlantic ARs, which are responsible a disproportionate number of days with extreme rainfall in those regions (Ramos et al., 2015). Interior continental regions in the northern hemisphere, such as the central U.S., eastern Europe, and eastern Russia show little if any common variance. This indicates that the ocean state plays only a minor role, if any, in explaining precipitation variance in these regions. Interior regions which show common variance are predominately located in the tropics and in southern hemisphere, which is likely highlighting convective activity fueled by oceanic moisture convergence, as the DJF period is the

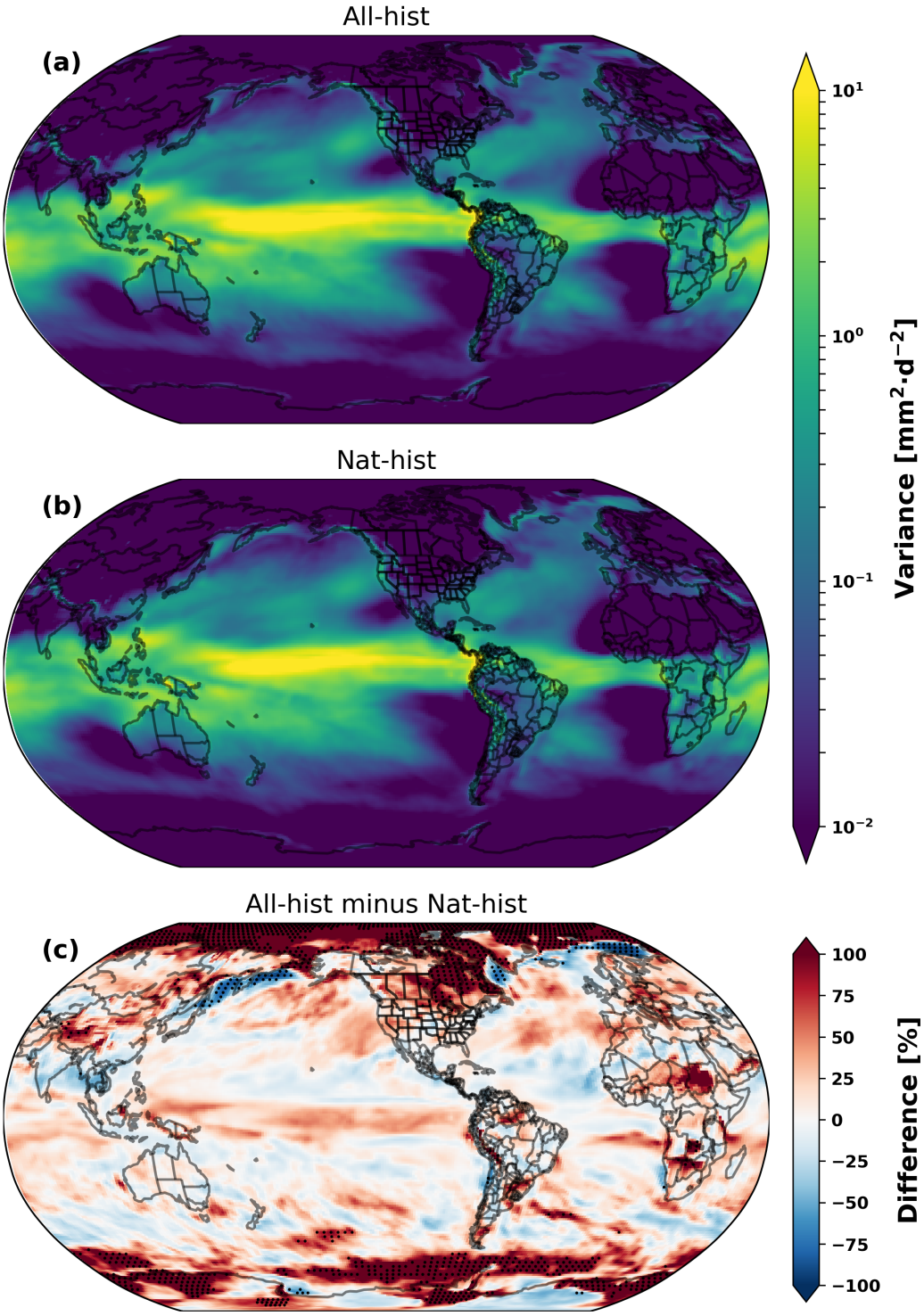

Figure 3.1: Absolute (total) DJF precipitation rate variance of the ensemble mean for the All-hist ensemble (a), the Nat-hist ensemble (b), and the difference All-hist minus Nat-hist (c). Locations statistically significant at the 90% confidence level are stippled. See methods Section 3.2.2 for details on the significance testing.

austral summer where deep convection is most active. Also highlighted in Figure 3.1, although of little importance to this study, are the world's arid regions, characterized by large-scale descending motion, which stabilize the atmosphere and inhibit precipitation, leading to effectively zero precipitation variability. Figure 3.1(c) shows the difference between the All- and Nat-hist simulations. Regions shaded red indicate areas where the common variance to the ocean have increased relative to the Nat-hist simulations. The regions which stand out the most are the polar regions, isolated regions in the extra-tropics, and the tropical rain belt. While the All-hist simulations show reasonably large increases in ocean forced precipitation variance, very few locations outside the polar regions are statistically significant. Given that the magnitude of the changes in the tropics and extra-tropics are relatively large, the only way they would fail to be significant in this framework is that if the total variability increase in those locations was greater than the increase in ocean forced variability. The statistically significant results in the polar regions may likely stem from the loss of sea ice in the All-hist simulations, thereby providing the polar atmosphere with direct source of moisture not present in the Nat-hist simulations.

To understand the contribution of ocean forced precipitation variability relative to total variability we calculate at the fraction of ocean forced variability shown in Figure 3.2. The fraction of ocean forced variability is calculated at each grid cell as the total ocean forced variability shown in Figure 3.1 divided by the variability representing the average variance of each ensemble member, shown symbolically by Eq. 3.4. This is the same methodology used by Dittus et al. (2018) who considered the role of observed ocean variability over land in the in driving temperature

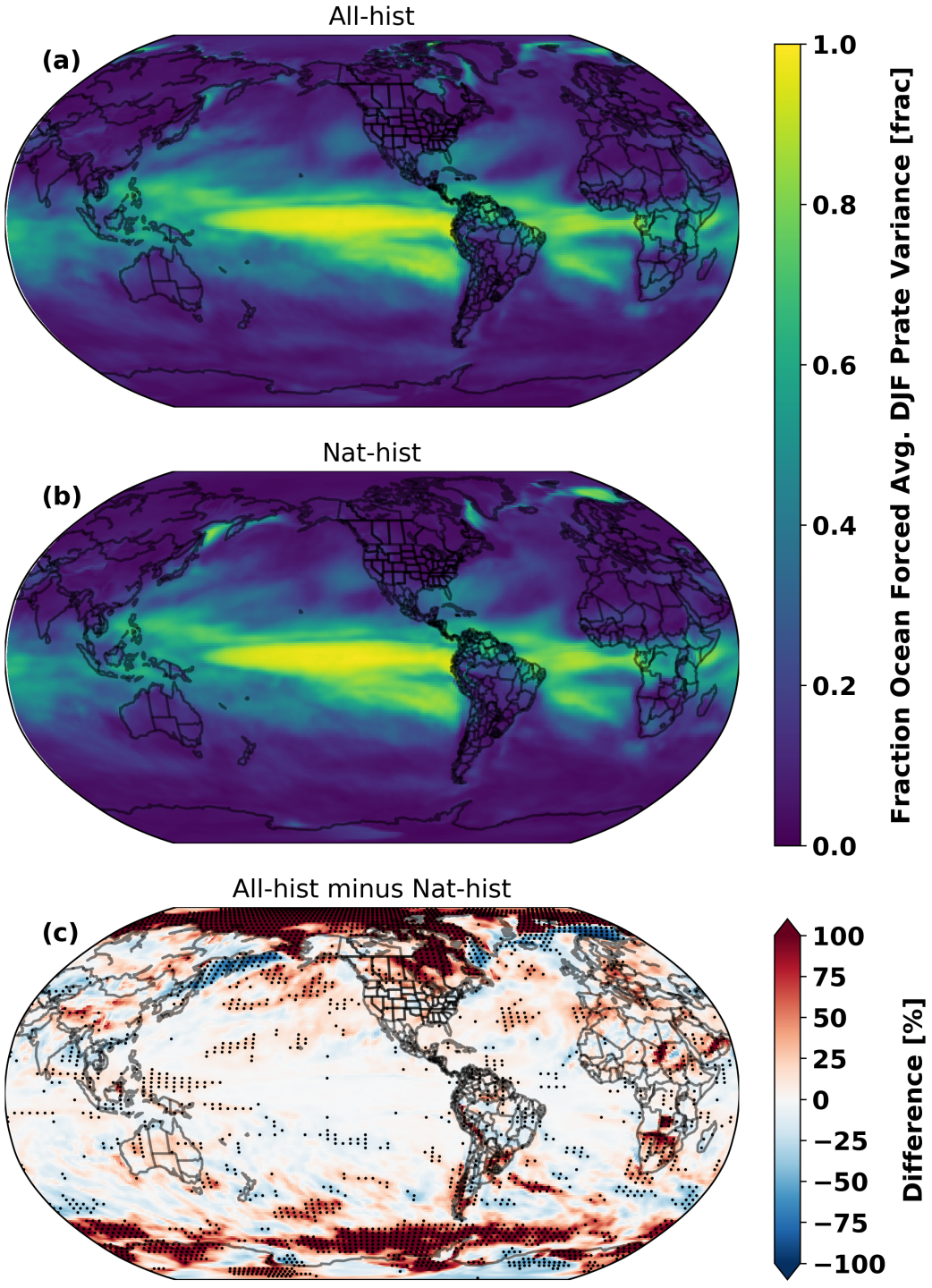

Figure 3.2: The fraction of common variance (ocean forced variance) relative to the average variance exhibited by each individual ensemble member for the All-hist simulations (a), the Nat-hist simulations (b), and their difference, All-hist minus Nat-hist (c).

and precipitation extremes. However, in their study, they used the median variance as opposed to the average variance. As they note, and verified here, the choice makes little difference to the results. The most notable feature of Figure 3.2 is the distinct El Niño pattern that emerges. This suggests that precipitation variability in this region is dominated by El Niño variability as the fraction is near one indicating that the proportion of ocean forced variability accounts for nearly 100% of the total variability. On the interannual time scale, El Niño events are associated with strong deep convection in the cold tongue region where anomalous warm ocean water makes its way into the tropical east Pacific, increasing the local SSTs above the threshold for deep convection in a region with climatologically cool SSTs. This in turn creates sharp zonal and meridional temperature gradients, which can then sustain intense and long-lived convective activity through strong moisture convergence fueled by the steep SST gradients that do not get easily exhausted due to the close proximity of an essentially infinite source of cold waters, which are capable of maintaining the sharp gradients. Figure 3.2 panel (c) shows the difference in the fraction of ocean forced variance between the All- and Nat-hist simulations. The regions that showed large changes in total ocean forced variance in Figure 3.1 have been largely suppressed here, indicating that the average relative contribution to precipitation variability by ocean forcing has not been appreciably altered by anthropogenic forcing.

Figure 3.2 represents the average relative contribution to precipitation variability resulting from ocean forcing. However, changes in the average are not always representative of changes that may be happening in other parts of the distribution.

For example, the mean can be left unchanged if the distribution spreads equally in both directions, which represents an important change that is not reflected by looking at average values. Therefore, to consider the possibility that changes may be occurring to the relative fraction of ocean forced precipitation variability that are not captured by changes in the mean, we construct a distribution of the possible contributions of relative ocean forcings and assess whether the distribution is sensitive to anthropogenic forcing by considering changes to the standard deviation of that distribution.

This distribution can be constructed by dividing the total ocean forced variance (the variance of the ensemble mean), not by the average of the ensemble variance as in Figure 3.2, but by the variance of each individual ensemble member. This results in 50 estimations of the fraction of ocean forced precipitation variance and we characterize that distribution not by the mean, which is what is shown in Figure 3.2, but by its standard deviation. Figure 3.3 shows the standard deviation of the distribution of the fractions of ocean forced precipitation variance. This is calculated as in Figure 3.2, but the denominator represents the variability associated with all 50 ensemble members rather than just the mean variability as in Eq. 3.4. A practical way to interpret Figure 3.3 is to imagine the bright colors representing a wide spread about the mean value of fraction of ocean forced variance shown in Figure 3.2 and cool colors representing a narrow distribution about that mean. Supplementary Figure C.1 is provided in order to aid in the interpretation of Figure 3.3. Overwhelmingly, the tropical band stretching from approximately 20°N to 20°S shows the greatest variability in the relative ocean forced precipitation variance. What this indicates is

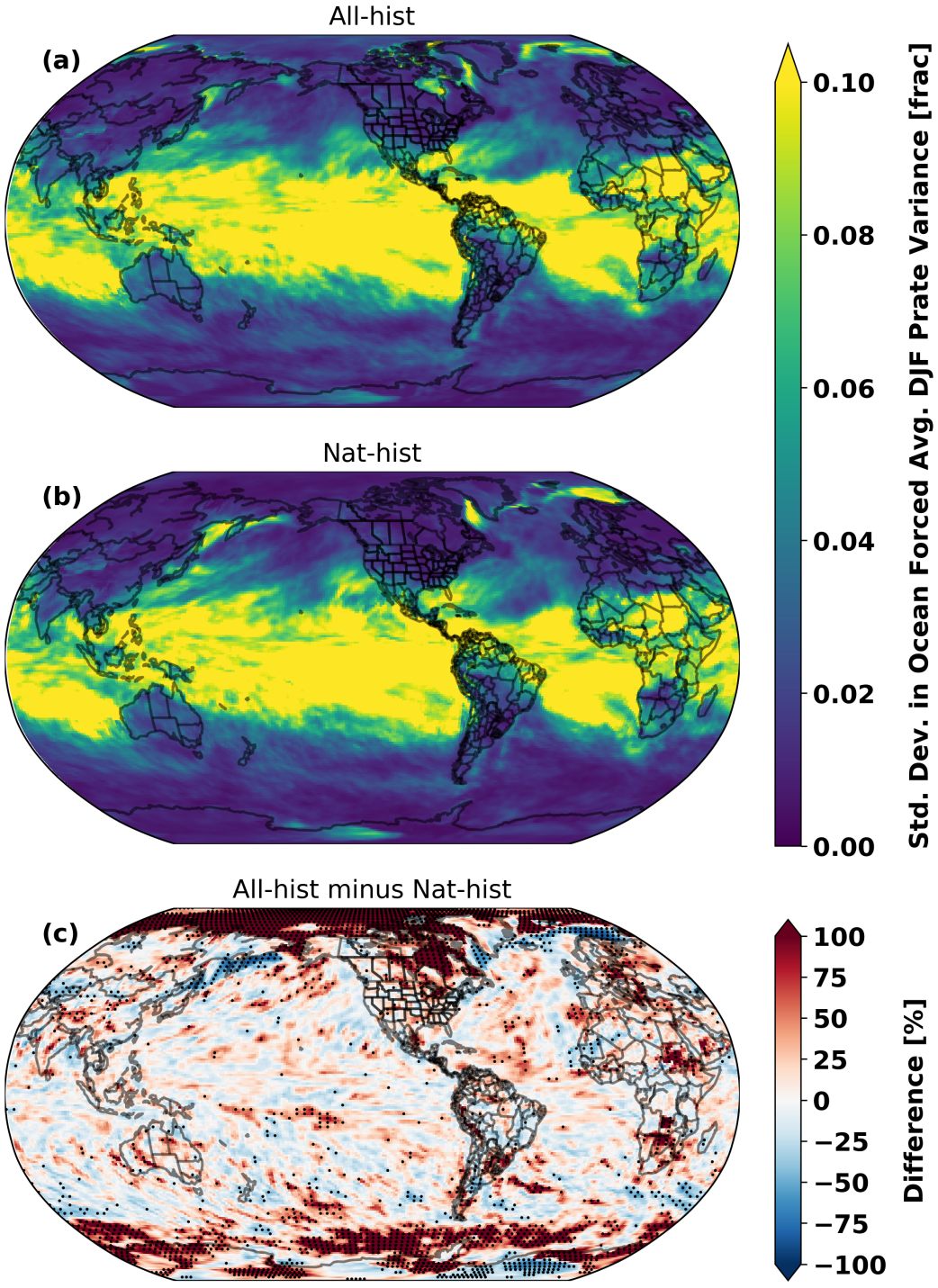

Figure 3.3: The standard deviation of the distribution of fractional ocean forced precipitation variance for the All-hist simulations (a), the Nat-hist simulations (b), and their difference, All-hist minus Nat-hist (c).

that within this band, there is high variability in the role ocean variability plays in forcing precipitation variability. As precipitation in the tropical band is primarily received through deep convection, this could be indicative of the complex relationship between SSTs and deep convection, whereby the ensemble members simulate a greater range of precipitation variability during the DJF season. Similarly, this result could also be reflective of known model short-comings in representing deep convective processes (O'Brien et al., 2016). Outside the tropical band, Figure 3.3 shows that there is little variation in the role ocean forcing plays in driving precipitation variability. Together, Figures 3.2 and 3.3 show that overall, the extra-tropics exhibit little sensitively to ocean forcing in that the average contribution is small and that there is little deviation about that contribution. Moreover, Figure 3.3 panel (c) shows that overwhelmingly, anthropogenic forcing has not appreciably altered the possible relative contributions ocean forcing can play in driving precipitation variability.

The results thus far have shown that total ocean forced precipitation variability showed relatively large increases in the All-hist simulations over the Nat-hist simulations, but were not statistically significant (Figure 3.1). However, the fraction of ocean forced variability remained constant between the All- and Nat-hist simulations, as well as the variability about that fraction (Figures 3.2 and 3.3). This then implies that there must be increase in variability between the All-hist and Nat-hist simulations occurring else where in the system. This would then be reflected as an increase in internal atmospheric variability between the All-hist and Nat-hist simulations, indicating that anthropogenic forcing has the effect of increasing internal

atmospheric variability and thus consequently, decreasing predictability.

In a SST forced large ensemble, an increase in internal atmospheric variability can show up in two ways, 1) an increase in interannual variability, or 2) an increase in ensemble variability for a given years ocean forcing. Figure 3.4 shows the average ensemble variance across all years. That is, it is the average spread of the ensemble predictions for average DJF rain rate for all years. Regions which show low values, such as the world's arid regions, indicate that there is in general good model agreement for the predictions of average DJF rain rate. Areas which show larger values indicate that the models on average simulate a greater range of outcomes for the equivalent ocean forcing in any given year. Practically speaking, these would be areas which exhibit on average lower year-to-year predictability due to a lower signal to noise ratio. Regions which display this high variability in model predictions reside primarily in the tropics and midlatitudes. The areas that display this relatively high uncertainty in outcomes are the deep convective regions such as the ITCZ and the midlatitude storm tracks. In particular, in both panels (a) and (b), the Pacific storm track appears split into two source regions, one, slightly weaker, stems the far west Pacific warm pool region and the other, from the Hawaiian Islands region. They merge off the western U.S. coast, which displays some of the highest values in model spread. Figure 3.4 panel (c) shows the difference in ensemble member spread between the All-hist and the Nat-hist simulations. Spatially coherent differences emerge between the All- and Nat-hist simulations, most prominent being the polar regions and across eastern Russia and Siberia. Two other notable spatially coherent regions stand out, the first being that off the western U.S.

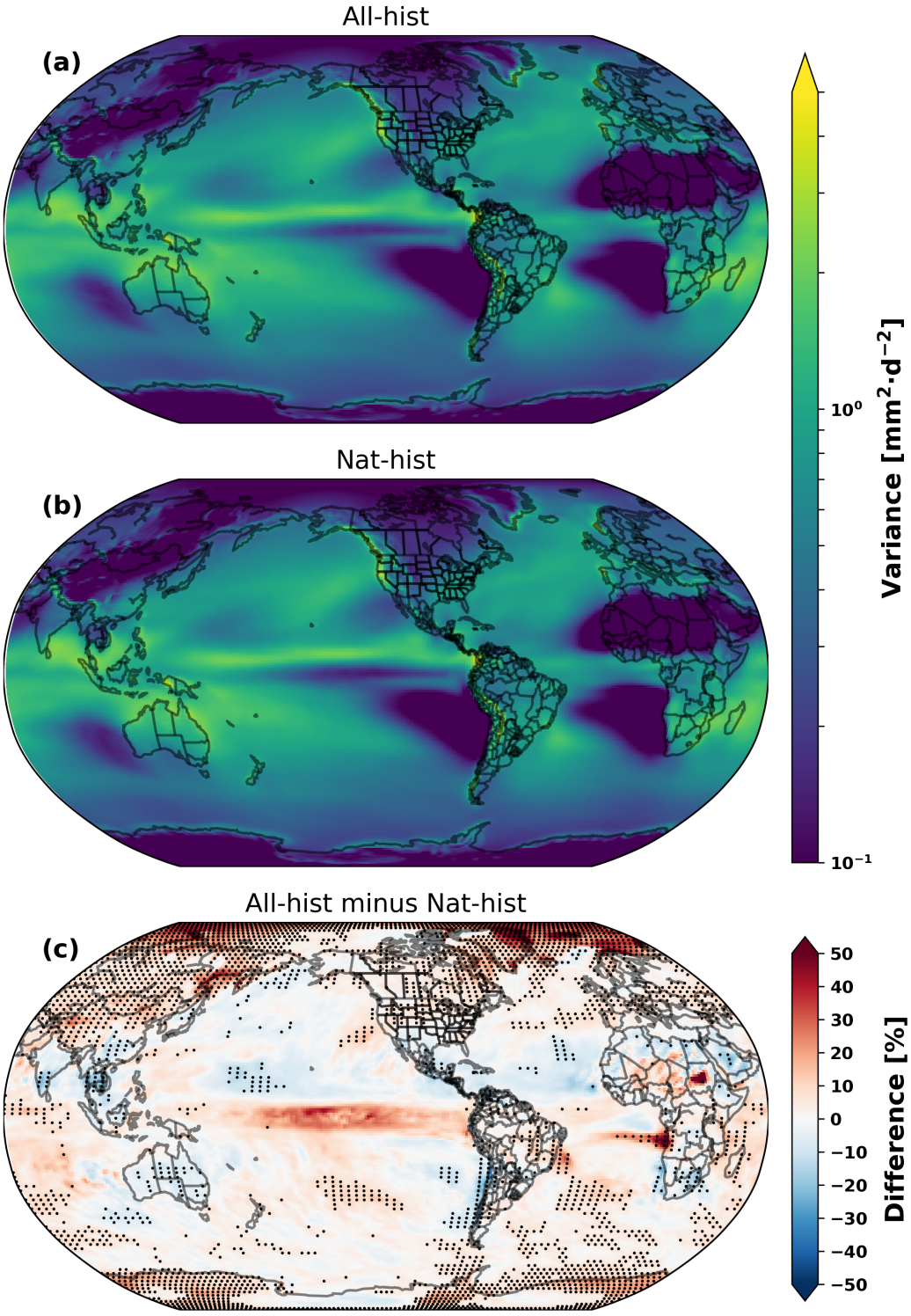

Figure 3.4: The average of the variance exhibited in each year by the individual ensemble members across all simulated years for the All-hist simulations. This is calculated as Eq. 3.7 for (a), the Nat-hist simulations (b), and their difference, All-hist minus Nat-hist (c).

coast stretching across the northern U.S. up into northeast Canada. The second being a swath stretching across the north Atlantic, intersecting France, and continuing across Europe. An interesting feature there appears in how the stippled region beginning in the northwest Atlantic near Newfoundland diverges, with one spatially coherent path extending north up to Iceland and the greater polar region, and the other extend east to Europe. This could potentially indicate a greater fraction of Atlantic storms making their way to the polar regions via this path thereby advecting warmer are to these regions than would have occurred in an unforced climate. Off the western U.S. coast a spatially coherent regions overlies the typically path traversed by ARs originating from the Hawaiian Islands. This is suggestive then that increased variability simulated by the models in the anthropogenically scenario may be tied variability in AR occurrence. This would be consistent with the results of Gershunov et al. (2019), who found in an analysis of CMIP5 simulations, that west coast hydroclimate variability increases in a future warmed climate and that the increase was primarily driven by an increase in AR strength and occurrence at the expense of lesser precipitation events. Overall, for the U.S. west coast, Figure 3.4(c) indicates that for any given year, the models simulate a greater range of possible outcomes for average DJF rainfall in an anthropogenically forced climate than they do in an unforced climate. This means that for any given ocean state the models simulate a greater range of possible outcomes thereby implying a loss of predictability as a result of anthropogenic forcing.

In addition to the possibility that the ensemble members together simulate a greater range of possible outcomes to the equivalent ocean forcing in the same year,

internal atmospheric variability can also manifest itself in each ensemble member individually, that is, within its own transient run, as in increase in year-to-year variability. This variability across time, i.e. climatological variability encapsulates what is perceived as year-to-year volatility, dubbed "whiplash" in the recent literature (Swain et al., 2018), and is exemplified by dramatic changes in precipitation from one year to another. The two expressions of internal variability, that is ensemble variability and climatological variability, are related but not necessarily the same. For example, each individual ensemble member could simulate greater climatological variability, while at the same time, together, all predicting the same outcome for each individual year. This would be an example of high climatological variability and low ensemble variability. On the other hand, each ensemble member could simulate low year-to-year variability, i.e. the ensemble mean being similar from one year to the next, but have high uncertainty about the outcome of any individual year (large ensemble spread in each year). So while separate in nature, as well as being computationally different calculations, they can be related in that an increase in ensemble variability can amplify, or be the main driving cause of increased climatological variability.

Figure 3.5 panels (a) and (b) show the average variance of each ensemble member across time in their respective transient runs calculated following Eq. 3.8. Compared to Figure 3.4 panels (a) and (b) the amplitudes of the year-to-year variance are much larger. This is a result of the ensemble variance positively contributing to the climatological variance and indicates that there is an increase year-to-year variability that is independent of the increase in ensemble variability. For a rela-

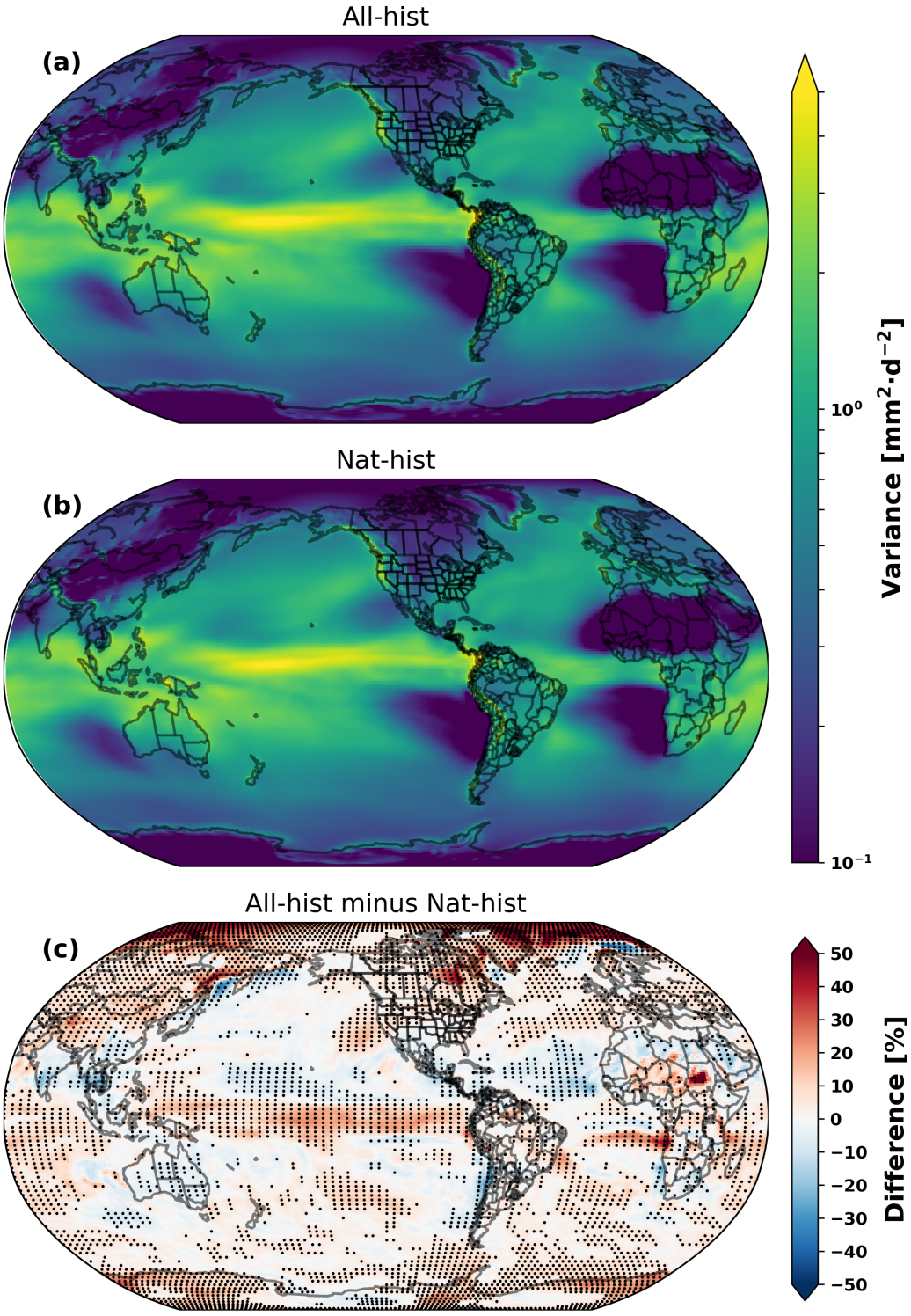

Figure 3.5: The average climatological (year-to-year) interannual precipitation variability associated with each ensemble member calculated as Eq. 3.8 for the All-hist simulations (a), the Nat-hist simulations (b), and their difference, All-hist minus Nat-hist (c).

tive comparison of the magnitudes of the climatological variance and the ensemble variance, supplemental Figure C.2 shows the ratio of the two. 3.5 panel (c) shows that the difference between the All-hist and Nat-hist climates has been amplified. The majority of the polar regions as well as midlatitude regions, especially over land, show a substantial increase in DJF hydroclimate variability. Notable areas that show decreases in variability relative to the Nat-hist simulations are the subtropical zones in the descending branch of the Hadley cell, India and southeast China, and Australia. The decrease in variability in the subtropical zones possibly reflects the theorized expansion of the Hadley cell under warming. However, concomitant with the expansion of the Hadley cell under warming is also weakening of its overturning strength (Lu et al., 2007, Levine and Schneider, 2011). Recent studies of reanalysis generally indicate there has been a strengthening of the Hadley cell over the last 50 years, although there is some disagreement in the results depending on which dataset is used (Mitas, 2005, Mitas and Clement, 2006). The decreases in precipitation variability over China and India may potentially stem from the difference in aerosol forcing between the All- and Nat-hist simulations. Over Australia, there is a fairly spatially coherent statistically significant decrease in interannual precipitation variability. However, DJF is the austral summer and precipitation in this region is dominated by convection that time of year, which is not directly resolved by a 1-degree model, and therefore may not be accurate. Along the U.S. west coast shows a well-defined increase in interannual DJF precipitation variability as does the west coast of Europe. Relative to the Nat-hist simulations, these regions would be characterized by winters showing large and variable year-to-year excursions in rainfall.

Therefore, in comparing Figures 3.4(c) and 3.5(c), for regions which show statistically significant increases, the results indicate that not only is the climate more variable on a year-to-year basis that it would have been in the absence of anthropogenic forcing, but the potential range of outcomes for any given year, regardless of the ocean state, are greater as well. Taken as a whole, the apparent anthropogenic effect is to make wintertime precipitation both more volatile from year-to-year and less predictable in any given year.

3.3.2 A Focus on Western U.S. DJF Precipitation Variability

We now turn our attention to the western U.S. for a focused analysis, where one of the largest and most spatially coherent changes in winter precipitation variability is observed (Figure 3.5). The western U.S. is aptly characterized by a large diversity of hydroclimates. The southern California climate is largely dominated by large-scale subsidence, which results in predominantly stable conditions and a Mediterranean-like climate. However, from roughly the San Francisco Bay Area northward, the climate is characterized by more temperate conditions, with typically wet winters as a result of consistent interaction with the southern edge of the Pacific storm track. Among all the regions along the west coast, California in particular is highly vulnerable to a changing climate. Because of its unique geographical location spanning the divide of regions dominated by wintertime subsidence and convergence, California is highly sensitive to potential changes in the storm track. Most models indicate that with continued warming, the Pacific storm track will shift northward and weaken; however, there is large model disagreement on that result

(e.g. Salathé (2006), Langenbrunner et al. (2015), Shaw et al. (2016) and references therein). A northward shift of the storm track will leave regions further north such as Oregon and Washington largely unaffected, as they will still be solidly in the storm track, although changes to the strength, either weakening or strengthening would be felt there. Baja California south of California will similarly be left unaffected by a shifting storm track as that region will still be dominated by large-scale subsidence. Thus because of its unique geographical location, California, even in a climate unaffected by human activities, is subject to high wintertime hydroclimate variability.

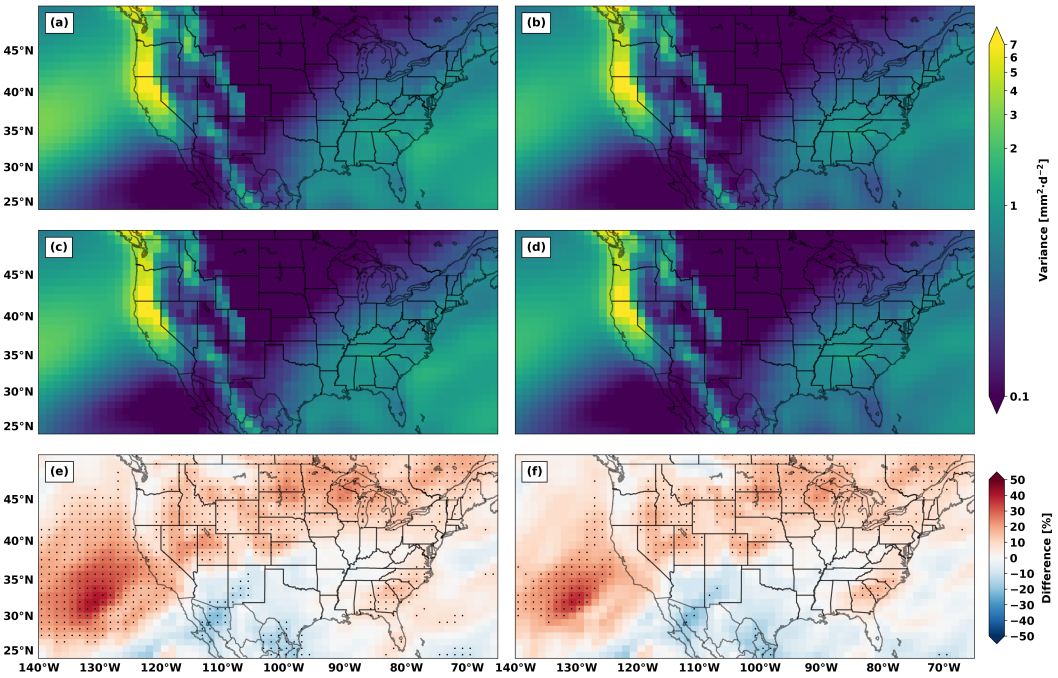

Figure 3.6: The All-hist climatological/ensemble variability (a)/(b), the Nat-hist climatological/ensemble variability (c)/(d), calculated as Eqs. 3.8/3.7, and their respective differences, All-hist minus Nat-hist climatological/ensemble variability (e)/(f).

Recent studies, most notably Swain et al. (2018) and Gershunov et al. (2019), have found that under continued global warming, California will be subject to even

greater hydroclimate variability than is already is currently experiencing. Here we ask instead, what role has the warming planet played thus far in contribution to the hydroclimate variability we experience today? Figure 3.6 shows the climatological variability in the left column and the ensemble variability in the right column. Panels (a-d) highlight that whether in an anthropogeniclly forced climate, panels (a,b), or in a climate unaffected by human activities, panels (c,d), the Pacific northwest is a region characterized by large winter hydroclimate variability. Also well-captured by the model is the precipitation variability associated with the Rocky mountains and the Sierra Madre of Mexico. Panels (e) and (f) highlight the large changes in winter hydroclimate variability induced by anthropogenic forcing. While the largest changes are centered off the California coast, the results here also indicate that a vast majority of the U.S. has also been subject to increased hydroclimate variability as a result of anthropogenic forcing. A notable exception to that is the U.S. southwest, which our results would suggest has experience an overall decrease in DJF precipitation variability. This is consistent with the findings of Seager et al. (2012) who noted that the U.S. southwest was one of the few regions not subject to an increase in P-E variability with warming. Off the the California coast, the changes in variability decrease moving both to the north and the south. This is likely the result of dominant and unchanged large-scale features that characterize those environments respectively, persistent convergence to the north and persistent subsidence to the south. Together Figure 3.6 panels (e) and (f) indicate that anthropogenic forcing has very likely played a role in the extremely unpredictable and volatile winters California has recently experienced. The results indicate that in-

ternal atmospheric variability plays a disproportionate larger role in driving winter hydroclimate variability in an anthropogenically forced climate by inducing larger year-to-year swings in accumulated precipitation and permitting a greater range of outcomes in any given year, regardless of the that years particular ocean state. These qualities are poignantly demonstrated by the recent 2015/16 strong El Niño event, which failed to deliver litte more than average precipitation. The following year, in the absence of any ocean forcing, California received one of its wettest winters on observational record. These events exemplify the kind of outcomes that Figure 3.6 indicates anthropogenic forcing has made more likely.

Given that the results thus far indicate that there has been a significant increase in hydroclimate variability due to anthropogenic forcing from 1960-2018, we assess whether the excess variability is evenly distributed across time. That is, does the excess anthropogenic component of internal atmospheric variability expressed equally in all years or are there some years where it is expressed more than others? Figure 3.7 the differences between the All- and Nat-hist simulations grouped by years of ENSO phase. ENSO phases are defined according to the ENSO longitude index (Williams and Patricola, 2018) in the left column, and the Nino 3.4 index in the right column. The El Niño phase is displayed along the top row, ENSO neutral across the middle row, and La Niña along the bottom row. For each index respectively, only the strongest years according to each phase are used, and the phase which has the fewest samples limits the number of years used for the other phases so each phase has an equal number of years in each composite. The years are selected from the classification provided in Table 1 of Patricola et al. (2019).

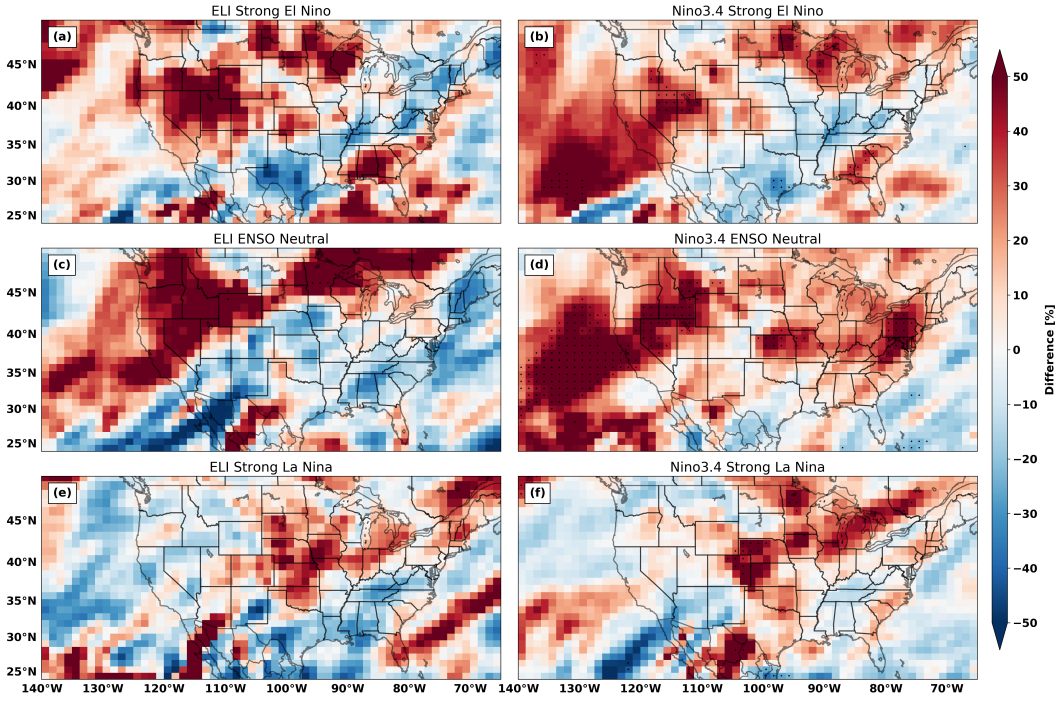

Figure 3.7: The differences between the All-hist simulations and the Nat-hist simulations grouped by the respective ENSO indices, the ENSO longitude index (ELI) in the left column, and Niño 3.4 in the right column. The rows show the results for years of strong El Niños, top row; ENSO neutral conditions, middle row; and Strong La Niña conditions, bottom row. Each are defined according to the respective indices and the ENSO phase with the fewest number of samples in each column limits the number of samples for all other phases. The events most characteristic of each ENSO are used, i.e. the strongest El Niño/La Niña events for top/bottom rows, and the most neutral ENSO years for the middle row. The years for each ENSO phase are selected from the categorization in Table 1 of Patricola et al. (2019).

Specifically, for ELI, strong El Niño has the fewest samples, 1983 and 1998. Therefore, for ENSO neutral conditions only 1991 and 1968 are used, and for strong La Niña only 1974 and 2009 are used. For the Nino 3.4 index, La Niña has the fewest samples totalling 5, therefore for the El Niño composite 2016, 1998, 1983, 1973, and 1992 are used, for the ENSO neutral composite 1970, 1980, 1991, 2004, and 1994, and for the La Niña composite 2008, 2000, 1976, 1989, and 1974 are used. Figure 3.7 shows that indeed, the anthropogenically forced component of variability is not expressed equally in all years. Overwhelmingly the increased variability

due to anthropogenic forcing is most strongly expressed during ENSO neutral and El Niño years. The lack of statistical significance in the ELI column most likely stems from the small sample size of two years representing each ENSO phase. The difference in amplitude for changes to El Niño forced variability between ELI (Figure 3.7(a)) and Nino 3.4 (Figure 3.7(b)) are likey due to the different sample sizes as well. However, it could also be because ELI is a physically-based metric and thus perhaps selects a more pure El Niño signal, as three of the years categorized as strong El Niño were not ranked as such by ELI. Thus the additional three years in the Nino 3.4 strong El Niño composite could be drawing bringing in variability, which may perhaps more appropriately belong in another category. That said, even in response to strong ocean forcing like El Niño, the increase in ensemble variability still suggests a more variable response than would be expected in an unforced climate. Therefore, as the climate continues to warm it may be that the hydroclimate response to strong El Niño becomes less constrained and therefore a less reliable source of hydroclimate predictability. Additionally, the extremely wet California winter of 2016/17 occurred at a time when the SSTAs would be best characterized as weak La Niña to ENSO neutral conditions. Thus, 3.7 panels (c) and (d) provide even stronger evidence that anthropogenic forcing played a role in the extremely wet and unexpected winter of 2016/17, not by directly causing it, but by allowing for a greater probability that it could happen. Furthermore, in the present warmed climate relative to the preindustrial, every storm that does occur has larger amount of atmospheric water vapor to draw on, about 7% more following Clausius Clapeyron (Allen and Ingram, 2002, Trenberth et al., 2003). Thus, to first order, each

storm that does occur has the thermodynamic potential to be at least 7% stronger, and potentially more depending on the dynamic contributions.

To further assess the role anthropogenic forcing may have played in altering the outcome of the 2015/16 strong El Niño, we compare the observed 2015/16 SST anomalies to those of 1983 and 1998 El Niños, which drove the "canonical" hydroclimate response in California. Figure 3.8 shows the respective SST anomalies for each of the three strong El Niño years beginning with 1983 on the left to 2016 on the right. The top two rows correspond to the observed DJF average SSTAs for the All-hist simulations in the top row and the Nat-hist SSTAs in the top-middle row. As described in Section 3.2.1, the Nat-hist SSTs have been cooled to the best estimate of what temperature they might have been in the absence of human interference with the global climate system. All SST anomalies are calculated with respect to the full 1960-2018 climatology. The bottom-middle row shows the difference between the All-hist and the Nat-hist SSTAs for each respective El Niño year. Along the bottom row are probability density functions for average DJF rain rate, spatially averaged over the state of California. The opaque red curves represent the All-hist distribution of outcomes from each ensemble member, for each El Niño year. Similarly, the opaque blue curves correspond to the distribution of outcomes from the Nat-hist simulations. The transparent PDFs in the background of each plot correspond to the respective climatologies, All-hist in red, Nat-hist in blue, both spanning 1960-2018, and the climatology from ERA5, spatio-temporally averaged in the identical manner and spanning 1979-2019, all the years for which data is available. The vertical dashed represent distribution means for All-hist (red

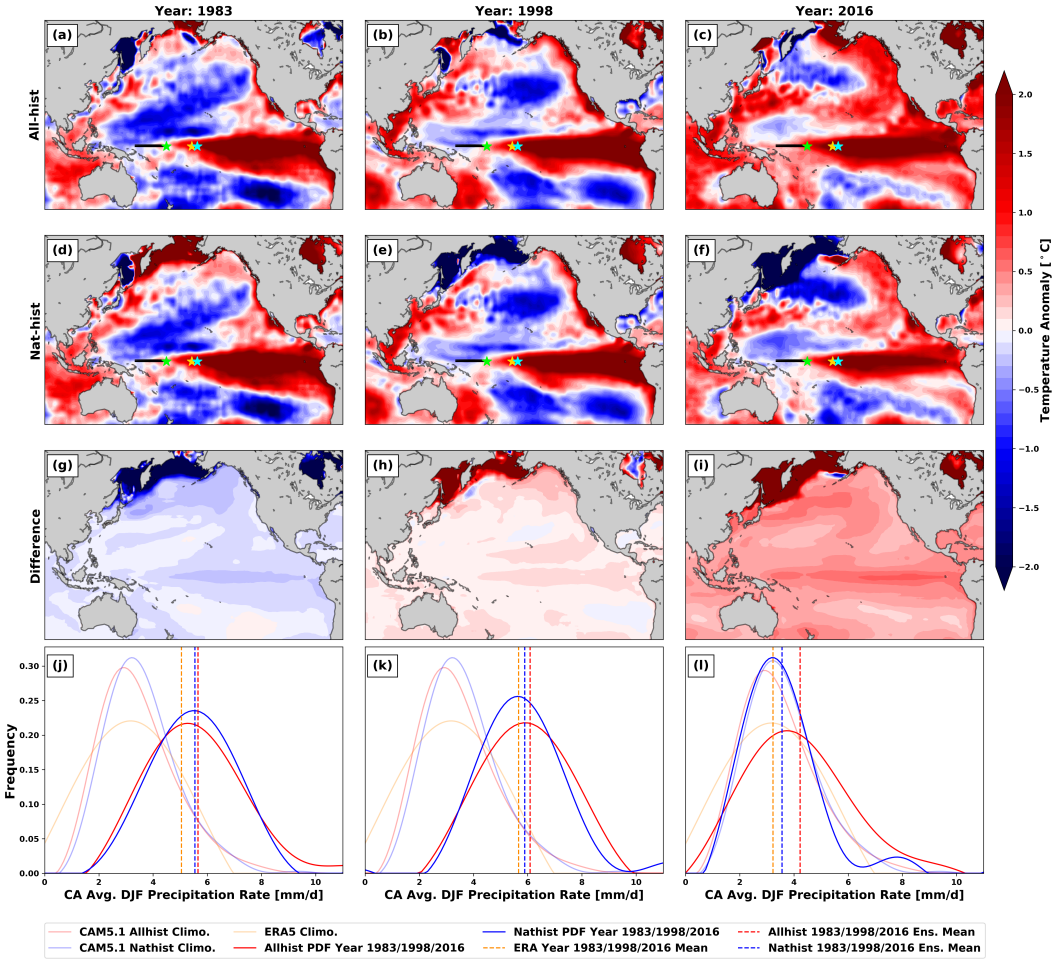

Figure 3.8: The comparisons of the differences between the strong El Niño years of 1983 in the left column, 1998 in the middle column, and 2016 in the right column. Across the top row the observed DJF average SSTAs corresponding the the All-hist simulations are shown. In the top-middle row, the DJF average SSTAs corresponding to the Nat-hist simulations, which have been cooled to the best estimate of what they might have been in the absence of human interference (see Section 3.2.1 for further details). All the SST anomalies are calculated with respect to their full 1960-2018 climatologies. Along the bottom-middle row is the difference between the All- and Nat-hist SST anomalies for the respective year in each column. Along the bottom row the PDFs of California statewide average DJF precipitation rate are shown for All-hist in red, Nat-hist in blue, and the observations according to ERA5 in gold. The transparent PDFS plotted in the background correspond the DFJ climatology. In the top two rows, the ELI values for each year are plotted in each panel for ease of comparison. The cyan star corresponds to the ELI value for 1998, the gold star for the ELI of 1983, and the green star for the ELI value of 2016. The horizontal black bar plotted along the equator in each panel in the top two rows corresponds to the range of the ELI seasonal cycle derived from data spanning 1900-2019.

dashed line), Nat-hist (blue-dashed line) and ERA5 observed value corresponding to the year in each column. In each panel of the top two rows, the ELI value corresponding to the individual El Niño years are plotted for ease of comparison. The cyan star corresponds to the ELI value for 1998, the gold star for the ELI of 1983, and the green star for the ELI value of 2016. The horizontal black bar plotted along the equator in each panel in the top two rows corresponds to the range of the ELI seasonal cycle derived from data spanning 1900-2019. Along the top row, the 1983 and 1998 share many of the same features, most prominently of which is the strong east Pacific SST anomaly. Relative to 1983, 1998 shows more coastal warming and a less spatially coherent north Pacific cool anomaly. However, arguably both feature a well developed tri-pole pattern from the southern hemisphere to the northern hemisphere, with the 1983 pattern showing the most coherent organization. In stark difference, is the pattern exhibited by 2016 anomaly. There exist significant and uniform ocean warming relative to both 1983 and 1998. The main east Pacific anomaly most commonly associated with driving a hydroclimate response is significantly less well-developed along the coast of Peru relative to 1983 and 1998. The anomaly is more closely situated toward the central Pacific where Modoki events are most commonly located (Capotondi et al., 2015).

Panels (g-i) show the estimated anthropogenically forced ocean warming for 1983, 1998, and 2016 El Niño SST anomalies. Panel (i) indicates that there was a significant component of the 2016 SST anomaly that was a result of human induced warming. The magnitude of the differenced anomaly in 2016 (panel (i)) is significantly larger than that of 1998 (panel (h)) or 1983 (panel (g)), suggesting the 2016

anomaly from a SSTA perspective, appeared much larger than it actually was.

The ELI values for each year are also extremely revealing as well, as both 1983 and 1998 lie far out into the east Pacific while the ELI of 2016 lies nearly 2000 km west of those of 1983 and 1998. Since ELI represents the average location of tropical deep convection, that is, it is generally taken to mark the center of deep convective activity. Note that the ELI values are the same for each year between the All- and Nat-hist simulations as part of the process of calculating an ELI value is a removal of the tropical mean state (see Williams and Patricola (2018) and Patricola et al. (2019) for further details). The proximal cause of the El Niño teleconnection to California is the atmospheric response to the anomalous deep convection associated with the unseasonably warm central Pacific waters that have migrated eastward in response to a weakened Walker circulation. The anomalous east Pacific convection generates a quasi-stationary Rossby wave that stretches north across the Pacific basin, deepening the Aleutian low, strengthening the Pacific storm track, and shifting it to the south of its climatological mean position thereby allowing more storms to make landfall in California (Philander, 1985, Alexander et al., 2002). Thus, since the 2016 ELI location is so far west of the ELI values for 1983,1998, they should not be expected to generate the same atmospheric response. As previously described, it is the proximity to the climatologically cool east Pacific waters that generates sharp zonal and meridional SST gradients, which are able to sustain strong moisture convergence fueling intense and long-lived deep convection. The further west, away from the cool east Pacific waters convection occurs, the less energy it has to draw upon thus the weaker it will be. The ELI location for 2016 places in much

climatologically warmer waters, thus the convective strength would be weakened relative to 1983 and 1998. Even more telling is that the ELI value for 2016 doesn't even place it outside the range of ELI seasonal cycle indicated by the horizontal black bar. This then would suggest that the atmospheric response would fall with in the range of natural variability. That said, the ELI location for 2016 is somewhat anomalous even though it lies within the range of the seasonal cycle. The 2016 average DJF ELI location is ≈175°, however, the climatological DJF value for that period is closer to ≈161°. The ELI seasonal cycle places it at its most eastward extent of ≈170° in July and August and its most westward extent of ≈157° in April. So relative to the ELI climatology for that time of year, the actual eastward anomaly is closer to ≈18° for 2016, versus ≈33° and ≈38° for 1983 and 1998 respectively.

Supplementary Figure C.5 shows the map view of the change in variability across CONUS specifically for the 2016 El Niño. It shows that the largest change in variability that winter occurred over southern California, which was the part of California that was left particularly dry that year (Paek et al., 2017, Singh et al., 2018).

Panels (j)-(l) show the probability density functions for estimated average DJF precipitation rate spatially averaged over California. The 50 simulations of 1983 and 1998 for both the All- and Nat-hist simulations show a remarkably consistent response to the ocean forcing in each of those years. The distributions themselves powerfully illustrate why an ensemble of simulations is required for estimating the most likely outcome for a given ocean forcing. In 1983 and 1998, both the All- and Nat-hist ensembles contained members which greatly exceeded and fell far below

the observed response shown by the vertical gold dashed line. Despite that, in both 1983 and 1998, the ensemble means of both the All- and Nat-hist simulations accurately predict the observed response. Moreover, the All- and Nat-hist climatological PDFs, plotted in the background in transparent red and blue respectively, accurately describe the observed California climatology given by the ERA5 reanalysis plotted in transparent gold. For a temporal portrayal of the changes in both climatological and ensemble variability noted thus far, supplementary Figures C.3 and C.4 show two representative time series for Bodega Bay, California and Houston, Texas respectively. These locations are specifically chosen to highlight the differences in the types of change these two climatologically distinct regions experience. Both supplementary figures are an alternate view/representation of the data in the main text figures.

Both the All- and Nat-hist climatological PDFs display much more well-defined tails than the ERA climatological PDF owing to the larger sampling of internal variability. The ERA PDF is informed by 40 years of observations spanning 1979-2019, while both the All- and Nat-hist ensembles contain 60 years of data from 1960-2018 with each year being simulated 50 times resulting in 2950 simulated years informing the PDF, thus giving a much richer sampling of the internal variability of the system. The PDFs for 2016 show that the observed response fall directly in the middle of the ERA5 distribution indicating the 2016 El Niño delivered just average precipitation that year. Most interestingly, the All-hist PDF for 2016 displays a significant widening relative to the Nat-hist simulations, and the widening predominately is driven by an increased probability for higher rain rates that year. The Nat-hist

distribution shows that the Nat-hist simulations accurately predicted the California hydroclimate response to the 2016 SST forcing. Moreover, the Nat-hist PDF displays much more certainty about the outcome of the 2016 hydroclimate response through the relatively small range of potential outcomes, showing little probability for a wet California winter as well. The 2016 All-hist distribution is wider than both the 1983 and 1998 distributions indicating internal atmospheric variability playing a relatively larger role in 2016. This then suggests that anthropogenic forcing artificially amplified the magnitude of the 2016 SST anomaly thereby allowing for a greater range of possible outcomes to the ocean forcing manifesting as an increase in internal variability evidenced by the widening of the 2016 All-hist PDF relative to the Nat-hist PDF.

Aside from the increased variability seen in the All-hist PDF of 2016, the climatological PDFs display an interesting change as well. The All- and Nat-hist PDFs shown respectively in transparent red and blue in panels (j)-(l) are shifted relative to each other. The mode of the All-hist PDF is shifted down and to the left of the Nat-hist PDF. This shift results in an increased probability for drier than average winters in California, seen as the All-hist distribution being above the Nat-hist distribution for low average DJF rain rates. This comes at the expense rain rates near the mean as the All-hist PDF is below the Nat-hist PDF for average DJF rain rates. Additionally, it can be observed that at the very highest climatological rain rates, the All-hist PDF again crosses over the Nat-hist PDF resulting in larger probabilities for extreme DJF rain rates. In the Nat-hist simulations, the probability for a DJF rain rate of 8 mm/d was effectively zero, however, in the All-hist simulations a DJF

rain rate of 8 mm/d is definitively non-zero. This rain rate is over 2 mm/d larger than the average rain rate that occurred during the extreme El Niño year of 1998, which resulted in extensive damages and loss all across California (Corringham and Cayan, 2019). An increased rain rate of 2 mm/d over the course of the 90 day DJF period translates to on average over 7 more inches of rain across all of California than fell during the 1998 extreme El Niño. If this were to happen, and the All-hist simulations suggest that in an anthropogeniclly forced climate it is possible, then the damages sustained in California would likely be devastating and more severe than anything that has occurred within the observational record. However, that said, the total change in probability from the Nat-hist simulations to the All-hist simulations is in total larger for smaller DJF rain rates, suggesting that overall, the change in variability due to anthropogenic forcing has, on average, favored drier winters on average rather than wetter ones. This then suggests that in California, climate change has had the effect to increase the probability for both droughts and floods and further highlights the particularly changeling nature of adapting to changes in variability. Because the All-hist climatological PDF is widened, reflecting the increase in variability in an anthopogenically forced climate, it allows simultaneously for both lower and higher rain rates, in any given year, across all of California.

As shown in Figure 3.7, the increased variability in the All-hist simulations are not expressed equally in all years. Similarly, the All-hist climatological PDF shown in Figure 3.8 indicate that the change in variability not be being expressed equally in all percentiles of the precipitation distribution. This then motivates decomposing average DJF rain rate by percentile and assessing changes in the variability of each

percentile individually. We do this for every year by selecting the daily DJF rain rate corresponding to the percentile under consideration. We then compute the standard deviation of those data for all years. We do that for every ensemble member then compute the ensemble mean. We choose the 10^{th}, 25^{th}, 50^{th}, 75^{th}, 90^{th}, and 99^{th} percentiles of DJF rain rate for consideration.

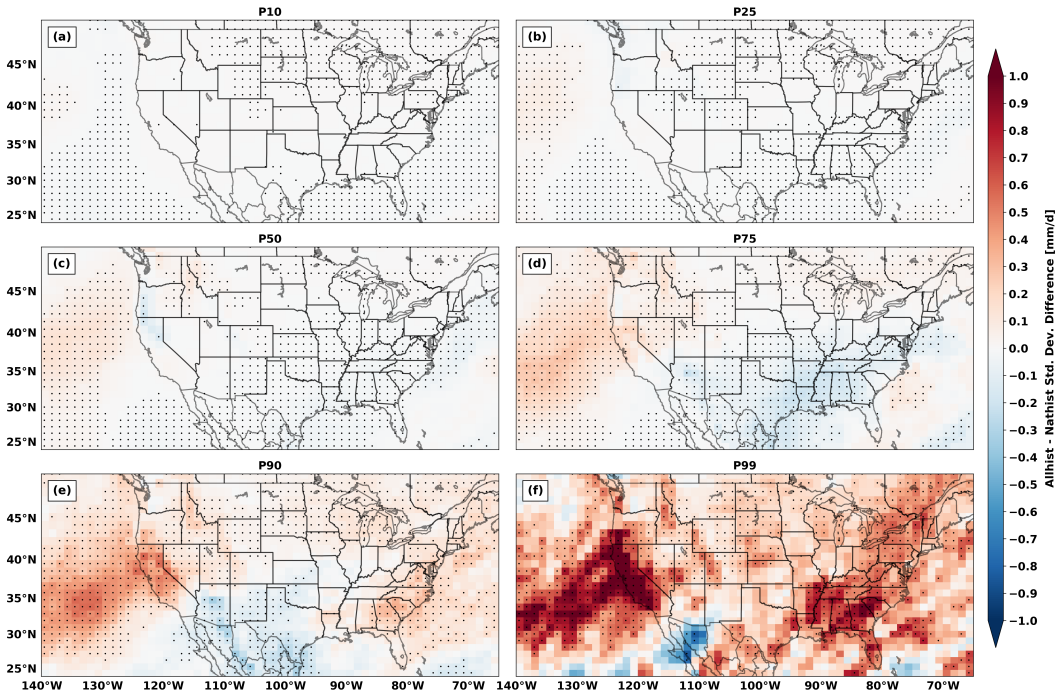

Figure 3.9: Panels (a-f) show the All-hist minus Nat-hist difference in standard deviation for the 10^{th}, 25^{th}, 50^{th}, 75^{th}, 90^{th}, and 99^{th} percentiles of DJF rain rate respectively. For both the All- and Nat-hist simulations, the percentiles for daily rain rate are calculated for each DJF period, and the standard deviation is taken across all years. This is done for every ensemble member and then the ensemble means are taken. The differences in the ensemble mean variances between the All- and Nat-hist simulations for each percentile are shown above.

Figure 3.9 shows the stark differences in how the excess anthropogenic variability is expressed across the percentiles of the average DJF rain rate distribution. The lowest rain rate percentiles, the 10^{th} and and 25^{th} shown in panels (a) and (b) respectively, show little to no change in variability across California between the

All- and the Nat-hist ensembles. The P50 percentile shown in panel (c) shows a slight decrease across northern most California, suggesting that the "average" DJF rain rate has become less likely. This can also be inferred, and is in line with, the changes to the climatological distributions of the spatially aggregated data for California shown in the bottom row of Figure 3.8. Both the 50^{th} and the 75^{th} percentiles shown in panels (d) and (e) and show progressive strengthening and a progressively larger footprint over California. At the 99^{th} percentile shown in panel (f), there is a highly nonlinear shift in the expression of anthropogeniclly forced variability from the 90^{th} to the 99^{th} percentiles. This indicates that the variability in the most extreme winter rainfall has been increased as a result of human activities. In other words, that due to human forcing, from year-to-year there can be large differences in the most extreme rain rates experienced. As panel (f) indicates, this is particularly true for California, but it is also a noticeable, and statistically significant change across most of CONUS. This even true for the U.S. southwest which showed, averaged across all percentiles, a decrease in the variability of average DJF rain rate (Figure 3.6). This implies that, that on the whole, DJF precipitation is less variable across the southwest, that is, pushed toward more consistent lower rain rates. However, the exception to this is seems to be, while not statistically significant, there is an elevated potential for experiencing daily rain rain rates that are more extreme than what they would have been in an unforced climate. But more so than anywhere across CONUS, this is particularly true for California and the Deep South. For California, the spatially coherent change in variability at the 99^{th} percentile has a southwest-northeast orientation suggesting that change in variability is likely related to either

difference in AR frequency, AR strength, or both between the All- and Nat-hist simulations. Gershunov et al. (2019) found a similar result for future California hydroclimate which was characterized by increased interannual variability that could largely be attributed to variability in AR occurrence. Similarly, they also found that while AR related precipitation increased in a future warmed climate, mean precipitation did not change due to a decrease in non-AR related precipitation. This then strongly suggests that the changes in California winter hydroclimate variability stem from an increase in both AR-frequency, related to the increase in interannual variability shown in Figure 3.6, and AR-strength, shown by the disproportionate increase in variability at the 99^{th} percentile in Figure 3.9.

3.4 Conclusions

Trends in mean in precipitation are not necessarily indicative of how precipitation variability behaves, that is, a null trend in the mean does not imply that other aspects of the distribution are not changing. For example, at the annual and decadal time scales large excursions in annual accumulated precipitation can be effectively negated by multiple years of below average precipitation. Thus despite extremely wet winters that may be suggestive of increasing winter precipitation, long term trends may remain negligible. The absence of precipitation observations not subject to the effects of the climate change that has occurred to date make it exceedingly difficult to distinguish natural variability from anthropogenically forced change. That, combined with a relatively short record of observations that limits the total sample

size, makes it even harder to draw statistically robust conclusions.

Observational studies have documented an increase in precipitation variability across a range of temporal and spatial scales (e.g. Karl et al. (1995), Tsonis (1996), Svoma and Balling (2010), and Pendergrass et al. (2017)). Yet, to what extent those trends may be the result of anthropogenic forcing has not been shown. Using two large ensembles of simulations that represent the observed climate over the last 60 years and what that climate might have looked like in the absence of human interference, we have shown that much of the observed precipitation variability is not a result of natural variability. In the anthropogenically forced simulations, we find a large increase in both interannual variability and the variability associated with extreme precipitation in any given year. While the fraction of variability attributable to the ocean has not changed in a meaningful way, the large increase in internal atmospheric variability in the anthropogenically forced simulations allows for a greater range of outcomes to the equivalent ocean variability than in the naturally forced simulations. Taken as a whole, our results indicate that the human interference with the global climate system has the net effect to make wintertime precipitation both more volatile from year-to-year and less predictable in any given year. Regions with naturally high hydroclimate variability appear to be affected the most, that is, to compound variability on top of already high hydroclimate variability. This is true for the western U.S., and in particular California, but is also true of other regions around the world including western Europe. A summary of our main findings are provided below.

1. In many regions around the world, we find a significant increase in the amount

of DJF (the boreal winter) precipitation variability attributable to anthropogenic forcing. Much of the increase in variability is the result of an increase in internal atmospheric variability, which allows for a greater number of seasonal hydroclimate outcomes in response to the equivalent ocean variability (Figures 3.4 and 3.5).

2. In the United States, the western U.S. and in particular California, has experienced the largest increase in average DJF precipitation variability and concomitant decrease in predictability as a result of anthropogenic forcing. However, the human forced increase in winter hydroclimate variability also appears across much of the northern half of the country stretching from the inner-mountain west to the Great Lakes region, as well as to a lesser extent the northeast and the eastern seaboard (Figure 3.6).

3. The increase in hydroclimate variability due to human forcing appears to not be evenly expressed in all years. Predominately, the increased variability is most strongly expressed during ENSO neutral years and to a slightly lesser degree El Niño years (Figure 3.7).

4. The increased variability due to human forcing appears to have played a role in altering the expected western U.S. hydroclimate response of the strong El Niño of 2015/16. Not only were the anthropogenic effects apparent in the variability of the precipitation response in California, but the magnitude of the tropical east Pacific SST anomaly appears to have been artificially enhanced due to a large increase in the temperature of the background ocean

state (Figure 3.8).

5. The probability density functions representing California average DJF precipitation climatology are shifted in the anthropogenically forced simulations relative to the naturally forced ones. The difference indicates a greater probability for years with below average precipitation, however, this also comes with a lesser, but increased probability for extreme flood years with potentially up to 33% more rainfall statewide than occurred during the extreme El Niño of 1998. Thus taken together, we find that anthropogenic forcing has made both drought and extreme flooding in California more likely (Figure 3.8).

6. The change in DJF precipitation variability is not reflected equally across all percentiles of the precipitation distribution. Overwhelmingly, the increase in variability is disproportionately expressed in the 99th percentile of DJF precipitation. Geographically, the largest change in the variability of the 99th percentile is in California. However, at that extreme precipitation rate, nearly everywhere across CONUS appears to have experienced an increase in variability due to human forcing. This is even true for the southwest U.S., which our results show on average, has seen a less variable DJF hydroclimate than would have occurred in a climate without human interference (Figure 3.9).

To summarize, in response to the same ocean variability the All-hist simulations produced on average more interannual variability than the Nat-hist simulations. In addition, the All-hist simulations also produced on average a wider range of out-

comes than the Nat-hist simulations for the same ocean forcing in any given year. The latter relates to a loss in predictability given a fixed ocean state, while the former relates to a climate characterized by greater year-to-year excursions in accumulated winter precipitation, i.e. higher highs and lower lows from year-to-year. In California, it is observed that to a large extent the increase in interannual variability is driven more by higher highs rather than lower lows. However, the lower lows have a greater probability of occurring in any given year than the higher highs. Both the ensemble variance for any given year and the interannual variance for any given ensemble member increased over that of the Nat-hist simulations. However, the average All-hist interannual variance increased more than the average All-hist ensemble variance. Together the anthropogenically forced simulations produce a climate that is both more variable year-to-year and with less predictable outcomes in any given year.

Closing Remarks

The impacts of meteorological and climatological extreme events are profound and far-reaching, causing disproportionate losses to human and environmental systems. The overarching focus of this dissertation is to understand, describe, and quantify a subset of extreme meteorological events occurring in a climate subject to a rapidly changing background state. Much of the work in this dissertation is specifically aimed at disentangling the naturally occurring variability of extreme events from the interwoven signal of anthropogenicllly driven change.

Chapter one introduced a novel approach to quantifying co-occurring meteorological extremes. Using a state-of-the-science multivariate nonparametric probability density estimation method, we used California wintertime temperature and precipitation and quantified their bivariate relationship as a function of third conditioning covariate describing various modes of natural variability and change. Using this methodology we were able to succinctly quantify nonlinear relationships that exist among the variables and explicitly account for statistical nonstationarity. Among the many revealing discoveries made, we found that, (1) the joint relationship of temperature and precipitation as a function of ENSO phase vary in such a way that in northern California, El Niño and La Niña winters tend to receive the same amount

of precipitation, however, La Niña winter tend to be much colder providing more favorable conditions for increased winter mountain snowpack and in turn a more stable water supply for the following dry summer months. (2) As a function of global mean temperature rise, the bivariate relationship of winter temperature and precipitation in California exhibit a highly complex and nonlinear relationship. Their joint dependence reveals that early in the 20th century, when global mean temperatures were $\approx$1°C cooler than they are today, warm winters were positively correlated with wet winters. However, around mid-century that relationship underwent a reversal such that presently, warm winters are now positively correlated with dry winters thereby elevating the risk for drought in California in the present climate. (3) Of all the modes of variability we considered, the dipole index, which describes the phase and magnitude of a circumpolar Rossby wavenumber 5, has the largest control of California wintertime temperature and precipitation. Of all the natural modes of variability studied, the dipole index was the only mode to favor simultaneous dry and warm winters. Because of the reversal in the temperature/precipitation relationship observed in the global temperature analysis, it remains an outstanding question whether global mean temperature rise has positively amplified the magnitude of control the dipole index has on California winter climatology or perhaps increased the frequency of expression of that particular wavenumber.

Chapter two focused on the detection and attribution of aggregated anthropogenic effect on wintertime hydrometeorology across the continental U.S. from 1960-2018. We considered a range of temporal scales to assess the potential nonuniform expression of an anthropogenic signal in time and in space. We use two sets of large

ensemble simulations, one which simulates the climate as it is today, and the other which simulates the our best estimate of what the climate might have been without human interference. Both ensembles share the same ocean variability therefore we calculate the anthropogenic effect as the residual between the two sets of simulations. We express changes to the types of events studied in forms: a magnitude-based form reflecting changes to the 100-year return level, and a frequency-based form, known as the risk ratio, which reflects changes in the number of occurrences of a particular type of event. By quantifying anthropogeniclly forced changes using these two methodologies, we are able to employ two independent methods for assessing the statistical significance of the results. This then in turn allows for independent statistical verification of the results to reinforce statistically significant findings where they exist. In addition, the large sample size the ensembles provide allow for the more nuanced detection of subtle signals. Using this framework we find that, (1) extreme daily rainfall above the 100-year return level are about twice as likely in an anthropogeniclly forced climate and about 7-10% larger in magnitude. (2) Along the U.S. west coast, anthropogenic changes on time-scales ranging from 1- to 40-days appear to be intimately related to atmospheric river activity. (3) Across nearly all of the continental U.S., the mean daily rain rate on days when it rained was about 3.5% larger in the anthropogenically forced simulation. This implies that the mean rate appears to scale at a rate commensurate with Clausius-Clapeyron. (4) At all time-scales considered, changes to the 100-year return level (extreme rainfall) was approximately 7% larger in the anthropogenically forced simulations implying that extremes appear to scale at a rate double that of Clausius-Clapeyron. (5) On

average, total winter precipitation increased over the northern half of the U.S. and in the northeast, but decreased over the U.S. southwest, California, and along the Pacific northwest coast.

Chapter three focused on detecting and identifying the anthropogenically forced contributions to changes in the observed temporal hydrometerlogical variability. Leveraging the same large ensembles employed in Chapter two, we quantified changes to the year-to-year variability in average December-February rain rate. We found that, (1) the anthropogenically forced simulations showed an increase in internal atmospheric variability, and correspondingly a decrease in seasonal predictability in any given year regardless of the ocean state. (2) The increase in hydroclimate variability associated with human forcing is not expressed evenly in all years. Years of ENSO neutral and El Niño tend to show the largest increase in anthropogeniclly induced precipitation variability. (3) The increase in precipitation variability due to human forcing appears to have played a role in the outcomes of both the failure of the strong El Niño of 2015/16 to drive the expected hydroclimate response in California and the 2016/17 extreme wet year occurring in the absence of any large-scale forcing. (4) The climatological probability density functions representing California DJF precipitation indicate that anthropogenic forcing has simultaneously increased the probability for both droughts and extreme flooding. The increase in the probability for below average rainfall is greater than the increase in the probability for extreme rainfall, but the changes are highly asymmetric. The increase in probability for flooding in the anthropogenically forced simulations indicates a nonzero probability of a DJF period with up to 33% more rainfall statewide than occurred during

the extreme El Niño of 1998. (5) The anthropogenically forced changes to inter-annual precipitation variability are not expressed equally across all percentiles of the precipitation distribution. Overwhelmingly, the excess variability is expressed in 90/99th percentiles of daily DJF precipitation rate, resulting in more extreme precipitation volatility from year-to-year. This change is observed across most of the continental U.S., but California in particular experiences the largest change in hydroclimate variability and volatility as a result of anthropogenic forcing.

In plain language, taken together the work contained in this dissertation shows that the climate change effects due to human activities, which has been predicted for many future scenarios, is already here, happening now, and affecting human and environmental systems. The observed changes to the global climate system are not consistent with natural variability alone and therefore the associated extreme events will become evermore disconnected from natural causal mechanisms in the future. As such, the effects documented here will only become more pronounced and severe if actions are not taken to limit global greenhouse gas emissions.

Appendix A

Supporting Material for Chapter 1: Metrics for Understanding Large-scale Controls of Multivariate Temperature and Precipitation Variability

Metrics for Understanding Large-scale Controls of Multivariate Temperature and Precipitation Variability

Supplementary Material

Authors

John P. O'Brien, Travis A. O'Brien, Christina M. Patricola, Simon S.Y. Wang

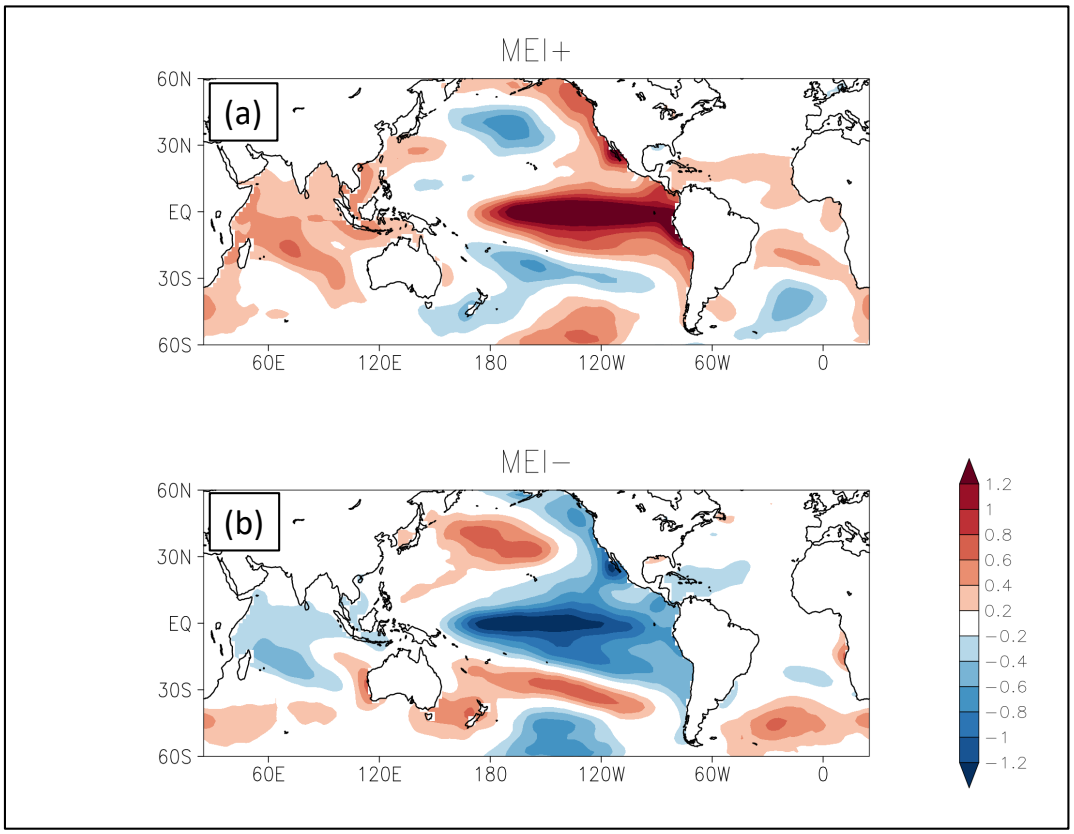

Figure S1. Composited sea surface temperature anomalies based on, (a) the highest 10 percent (P90) winter values of MEI and, (b) the lowest 10 percent (P10) of winter MEI values. These SSTA patterns represent, (a) El Nino and, (b) La Nina and correspond to the cPDFs in Figure 1 panels (d),(e) and (i),(j).

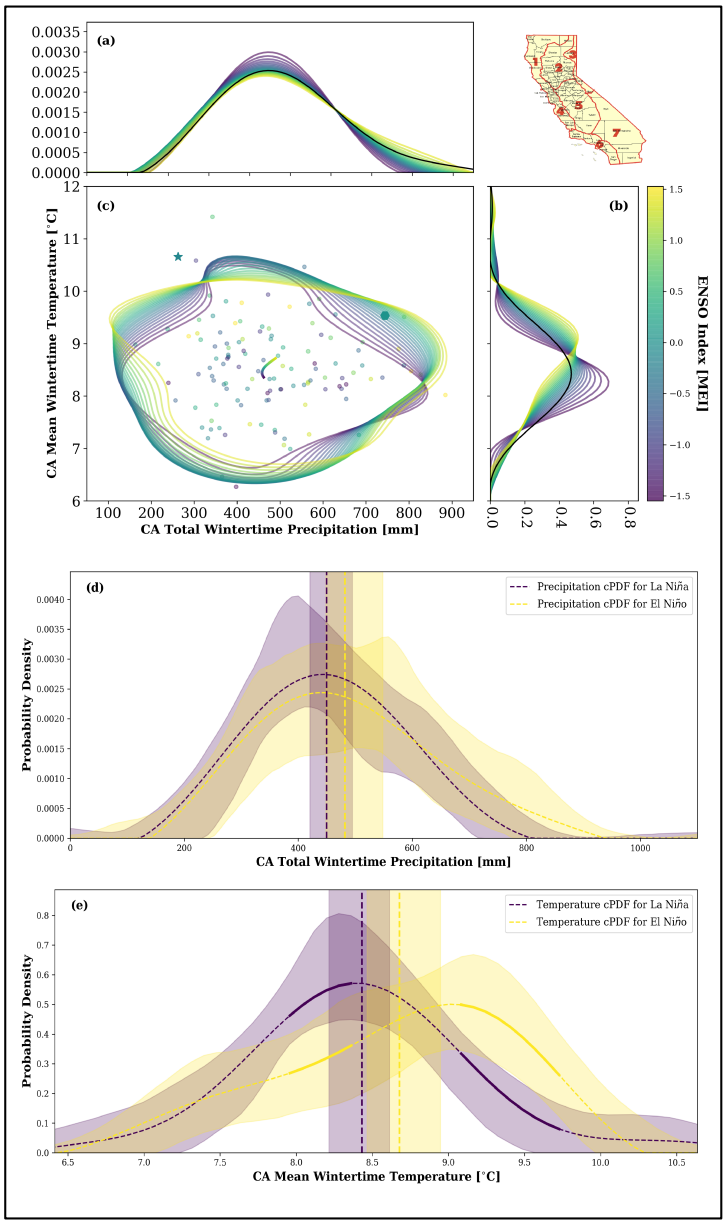

Figure S2. Figure as in the main manuscript, however, all temperature and precipitation data are statewide wintertime averages conditional on MEI.

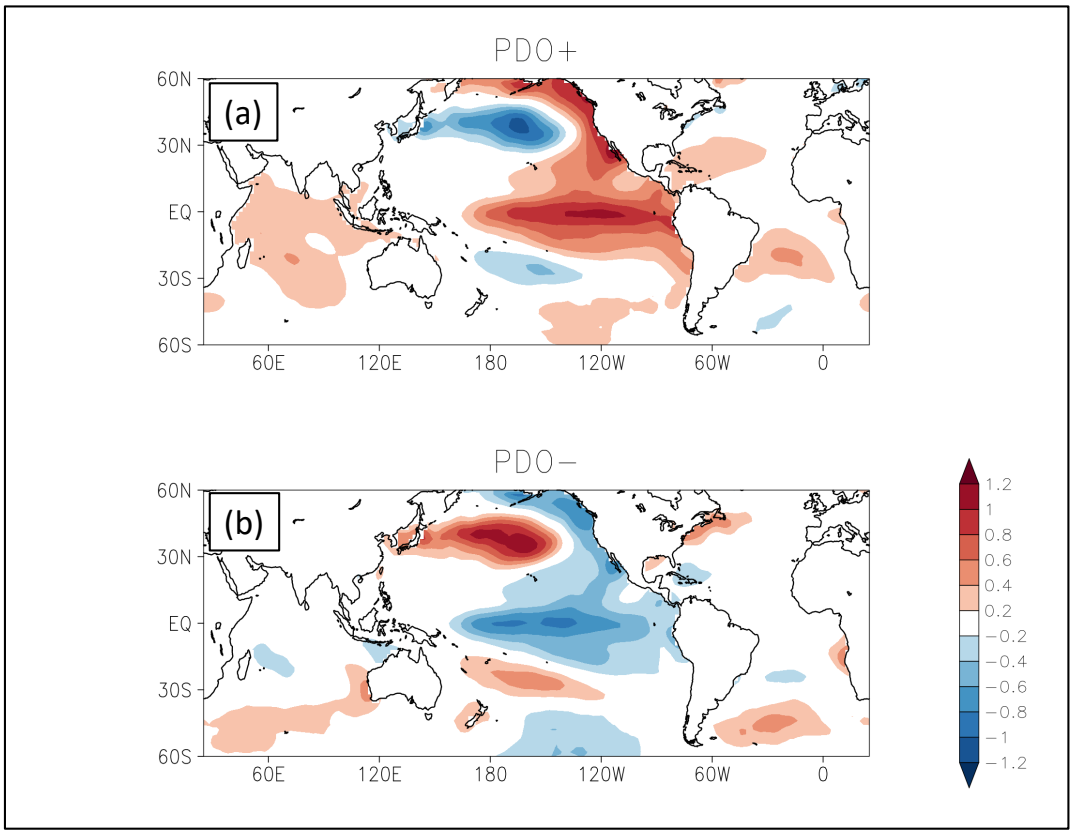

Figure S3. Composited sea surface temperature anomalies based on, (a) the highest 10 percent (P90) winter values of PDO and, (b) the lowest 10 percent (P10) of winter PDO values. These SSTA patterns represent, (a) the PDO warm phase, (b) the PDO cool phase and correspond to the cPDFs in Figure 2 panels (d),(e) and (i),(j).

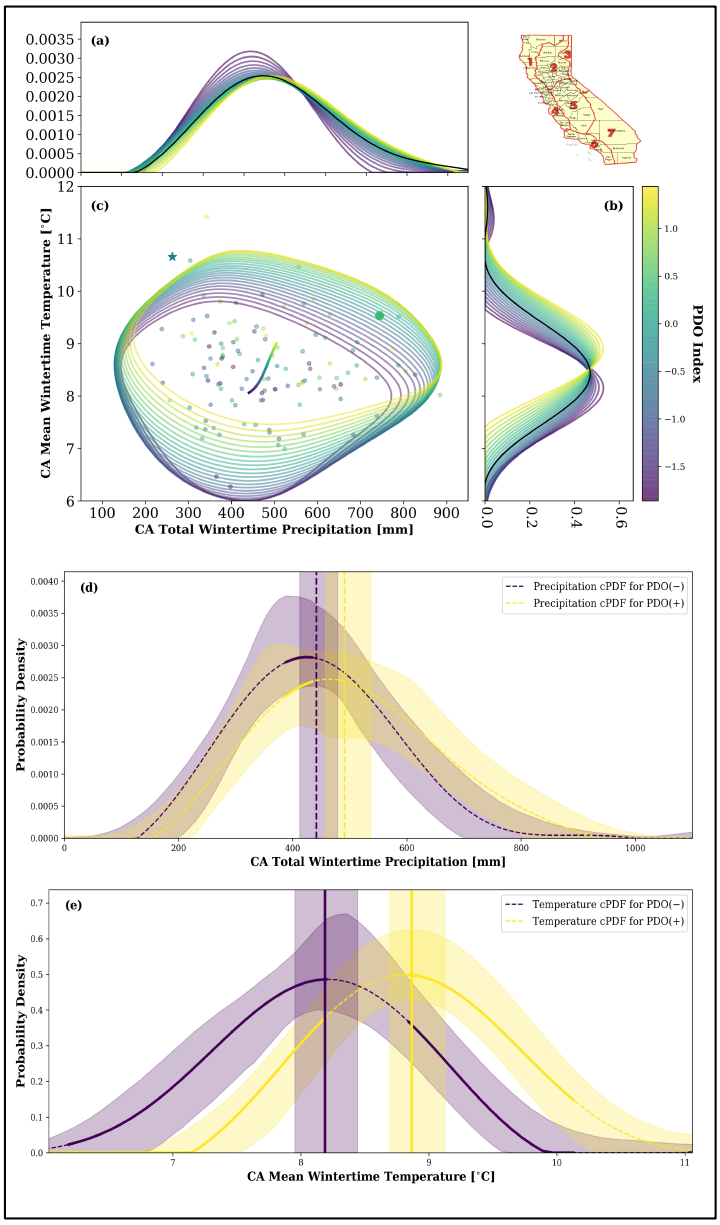

Figure S4. Figure as in the main manuscript, however, all temperature and precipitation data are statewide wintertime averages conditional on PDO.

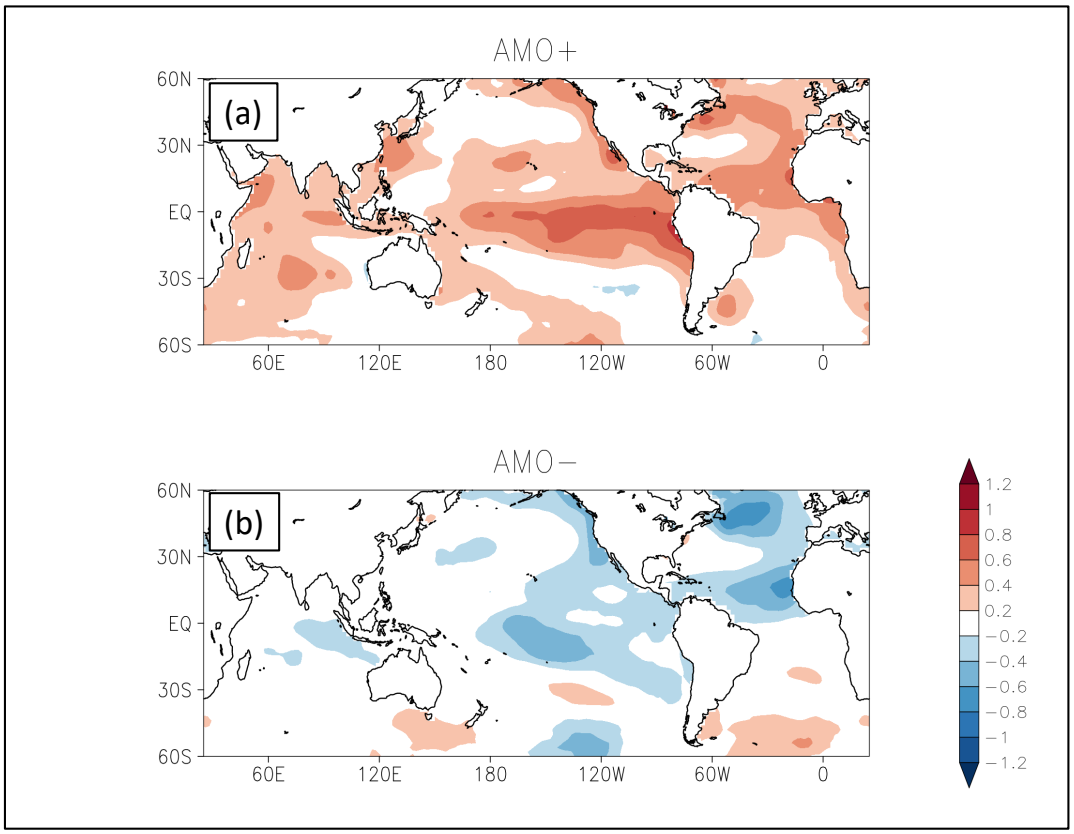

Figure S5. Composited sea surface temperature anomalies based on, (a) the highest 10 percent (P90) winter values of AMO and, (b) the lowest 10 percent (P10) of winter AMO values. These SSTA patterns represent, (a) the AMO warm phase, (b) the AMO cool phase and correspond to the cPDFs in Figure 3 panels (d),(e) and (i),(j).

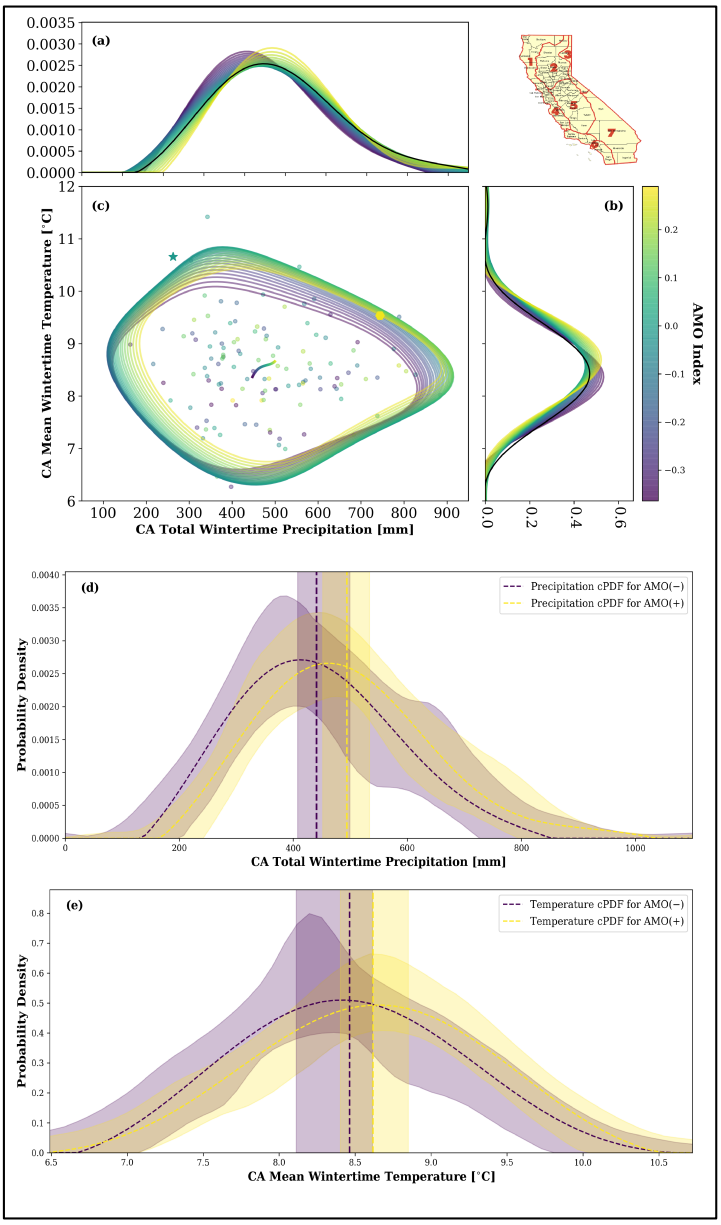

Figure S6. Figure as in the main manuscript, however, all temperature and precipitation data are statewide wintertime averages conditional on AMO.

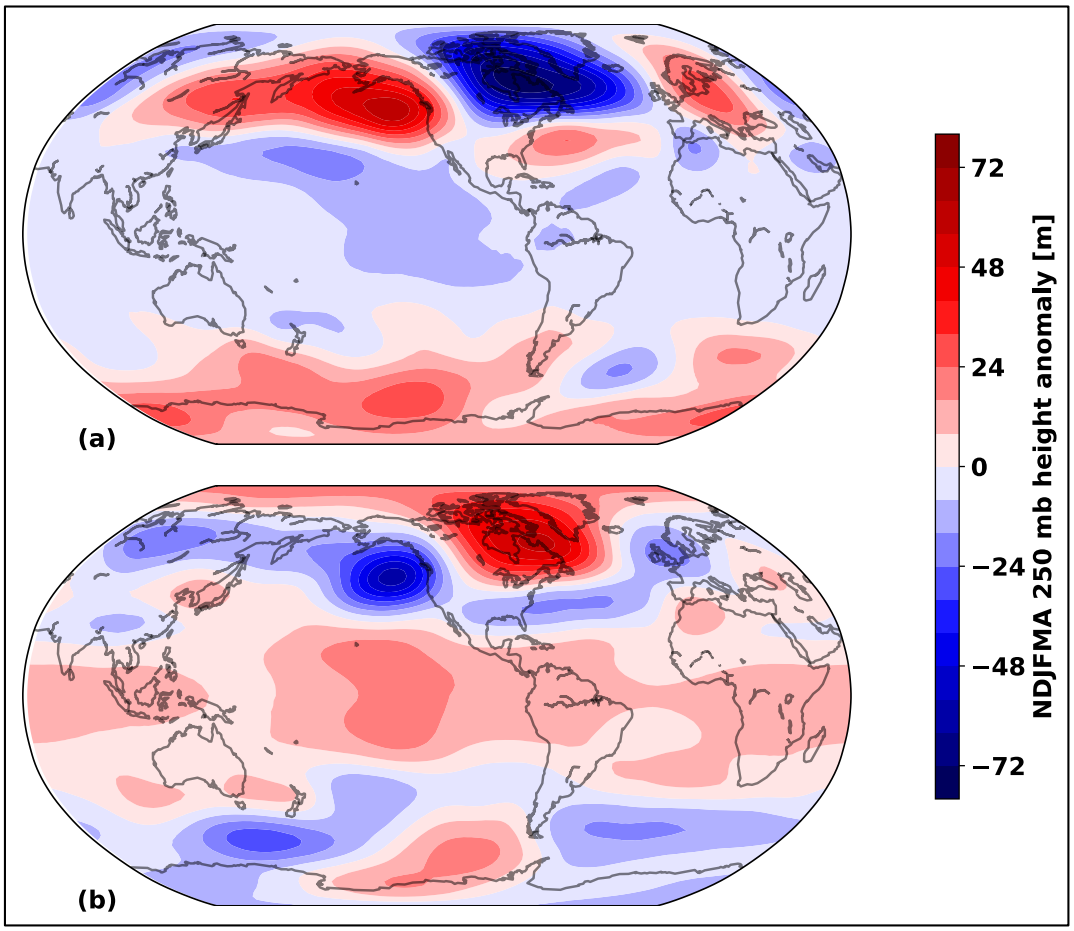

Figure S7. Composited geopotential height anomalies based on, (a) the highest 10 percent (P90) winter values of DPI and, (b) the lowest 10 percent (P10) of winter DPI values. These atmospheric patterns represent, (a) the DPI positive phase, (b) the DPI negative phase and correspond to the cPDFs in Figure 4 panels (d),(e) and (i),(j).

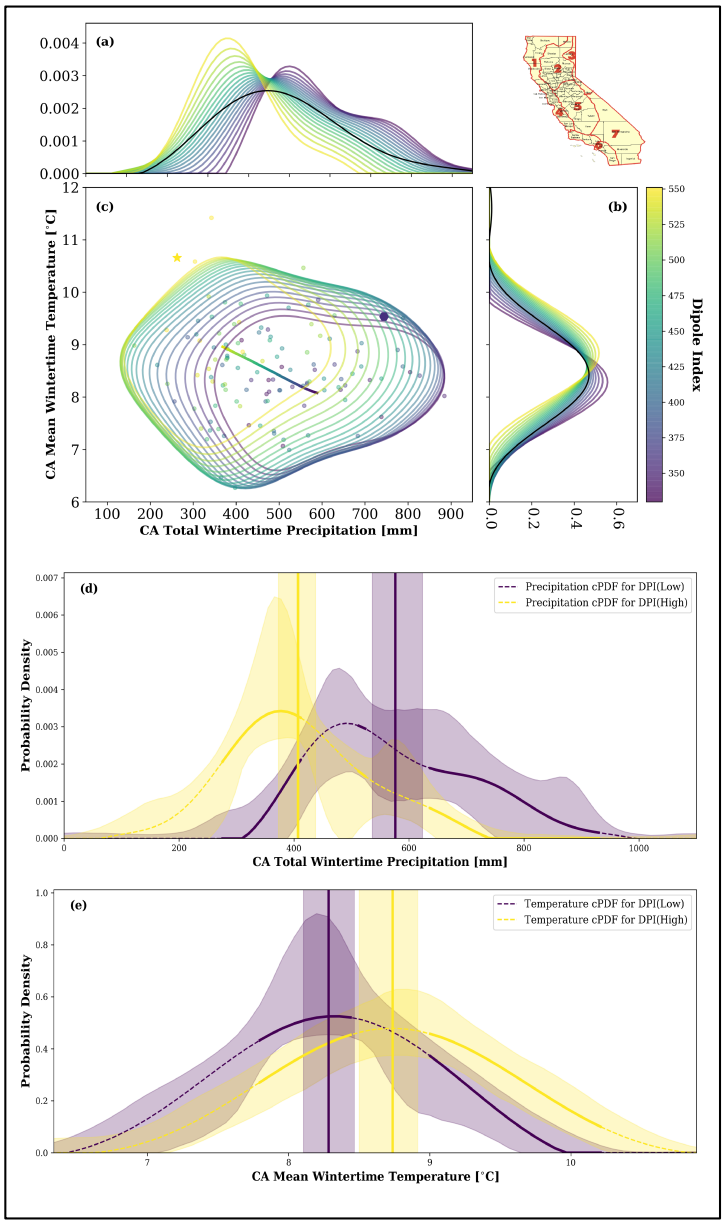

Figure S8. Figure as in the main manuscript, however, all temperature and precipitation data are statewide wintertime averages conditional on DPI.

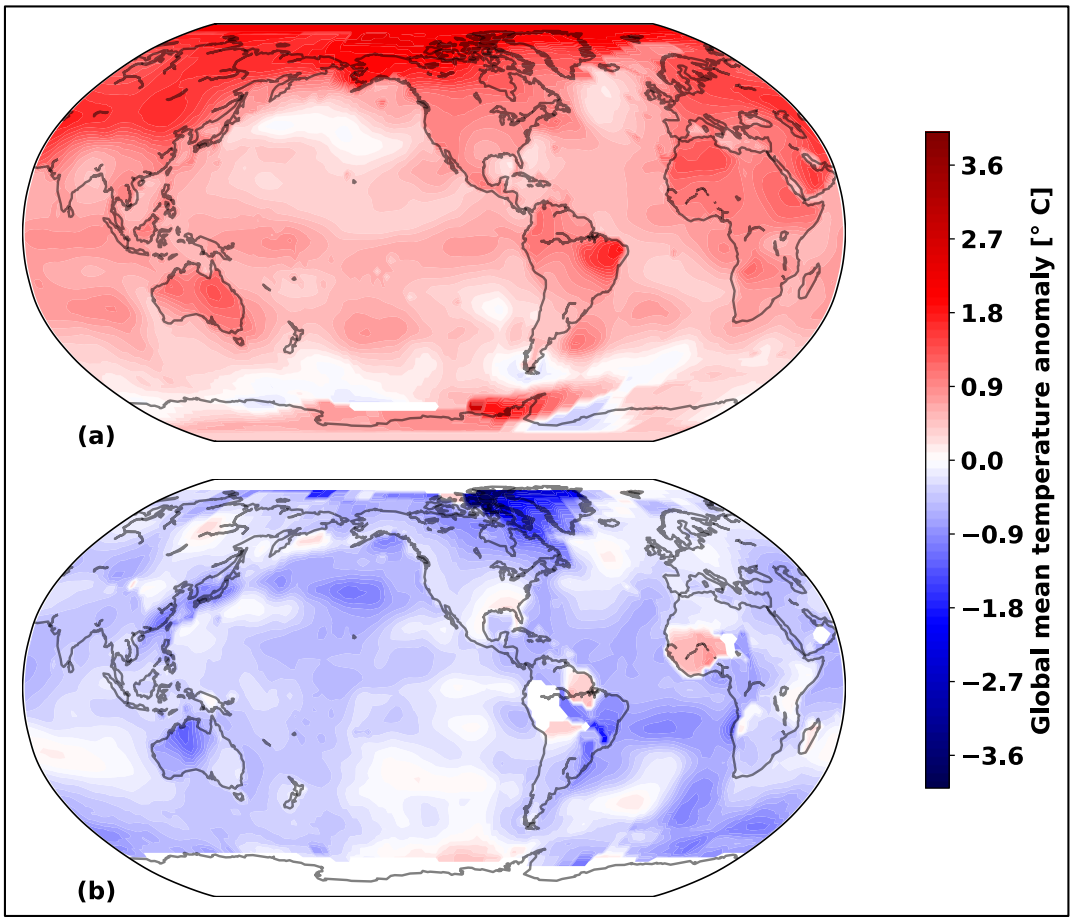

Figure S9. Composited global mean temperature anomalies based on, (a) the highest 10 percent (P90) winter values of GMTA and, (b) the lowest 10 percent (P10) of winter GMTA values. These temperature patterns represent, (a) the late 20th/early 21st century , (b) the late 19th/early 20th century and correspond to the cPDFs in Figure 5 panels (d),(e) and (i),(j).

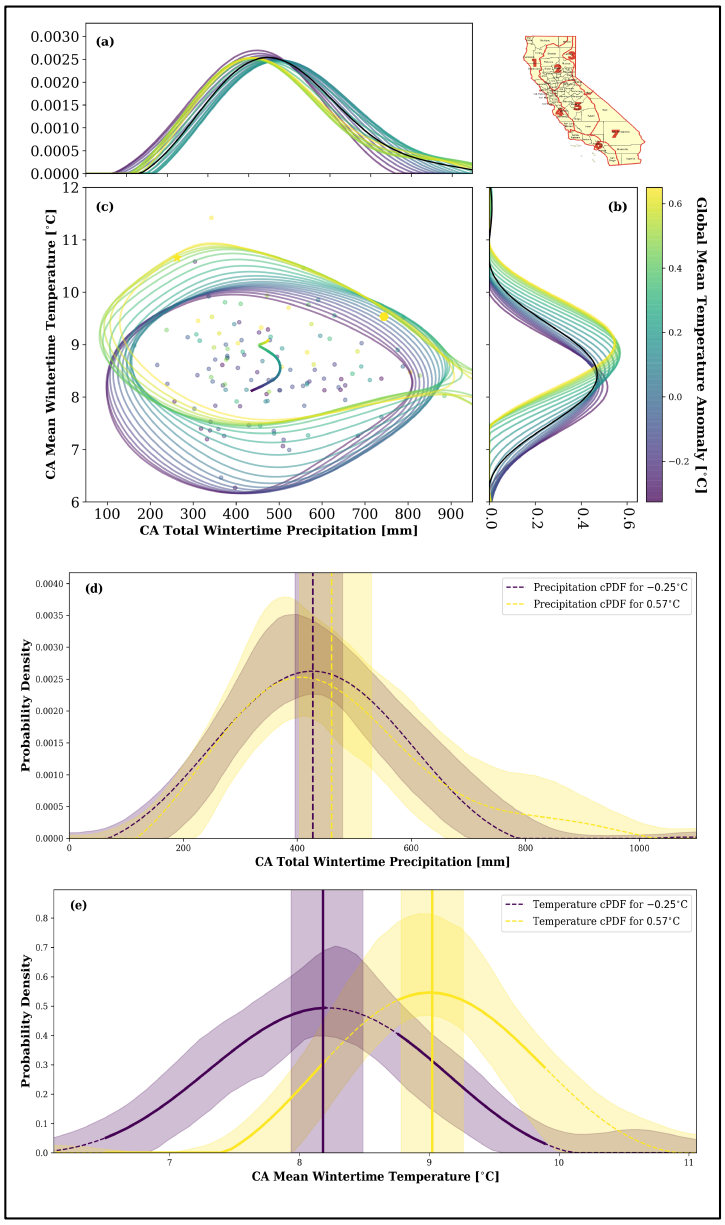

Figure S10. Figure as in the main manuscript, however, all temperature and precipitation data are statewide wintertime averages conditional on GMTA.

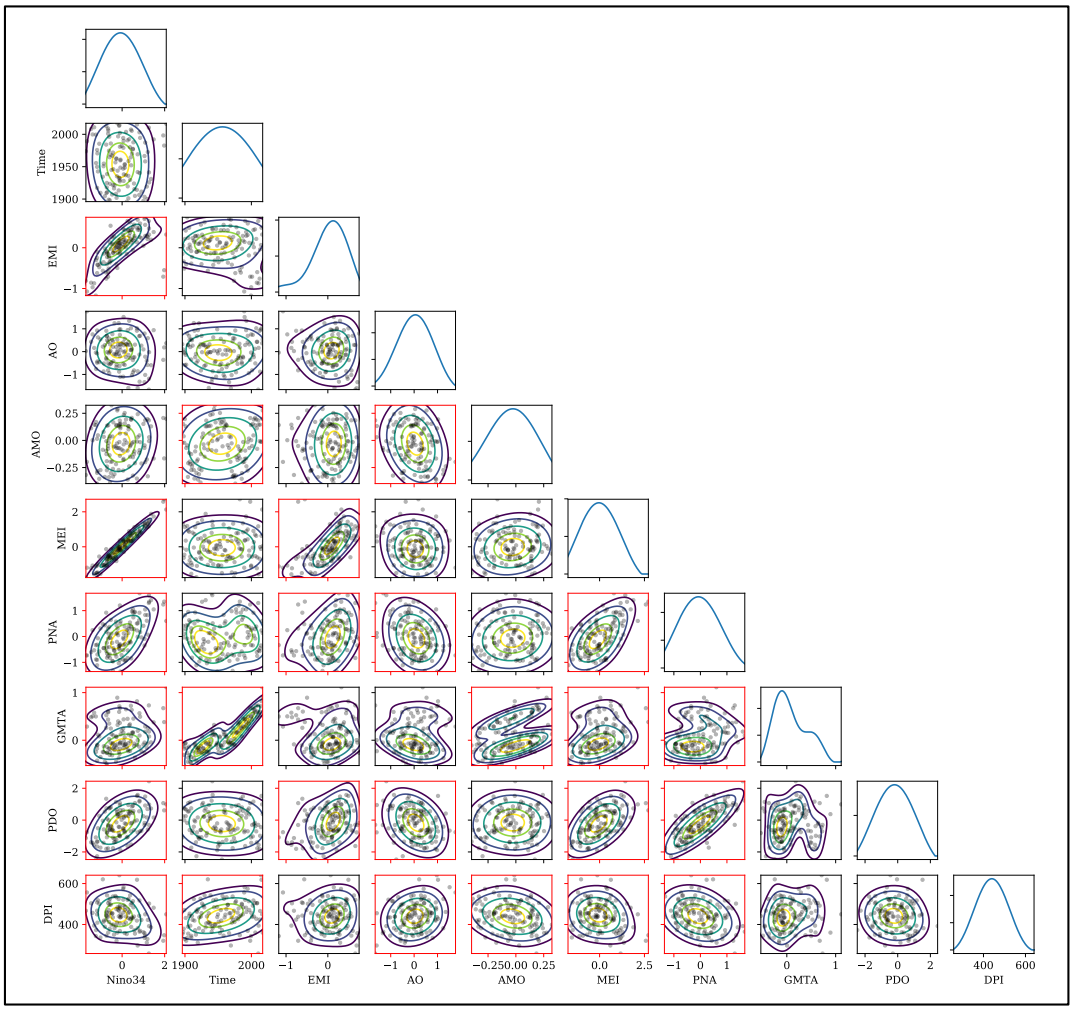

Figure S11. Pairplot showing the inter-relationships between all variables considered for this study. Subplots boxed in red represent statistically significant correlations (p<=0.1).

MEI P10	MEI P90	PDO P10	PDO P90	AMO P10	AMO P90	DPI P10	DPI P90	GMTA P10	GMTA P90
1910	1897	1910	1905	1904	1900	1900	1923	1898	1998
1917	1919	1917	1908	1914	1938	1902	1930	1903	2002
1918	1926	1949	1926	1920	1942	1903	1934	1904	2004
1950	1931	1950	1927	1921	1944	1909	1939	1905	2005
1955	1941	1951	1940	1923	1945	1910	1957	1907	2006
1956	1942	1952	1941	1972	1952	1916	1959	1908	2007
1971	1958	1956	1942	1973	1953	1919	1963	1909	2009
1974	1973	1972	1984	1974	1998	1958	1972	1910	2010
1976	1983	1991	1987	1975	2004	1969	1989	1911	2013
1989	1987	2000	1998	1976	2005	1983	1990	1913	2014
1999	1992	2009	2003	1977	2007	1998	1994	1917	2015
2008	1998	2011	2015	1985	2016	1999	2014	1918	2016
2011	2016	2012	2016	1986	2017	2010	2015	1929	2017

Table S1. Table documenting the years which correspond to winter averages that are less than (greater than) the P10 (P90) values for each mode of variability (conditioning variable) used in this study.

Appendix B

Supporting Material for Chapter 2: The Anthropogenic Contribution to the Observed Hydrometeorology over the Continental U.S. from 1960-2018

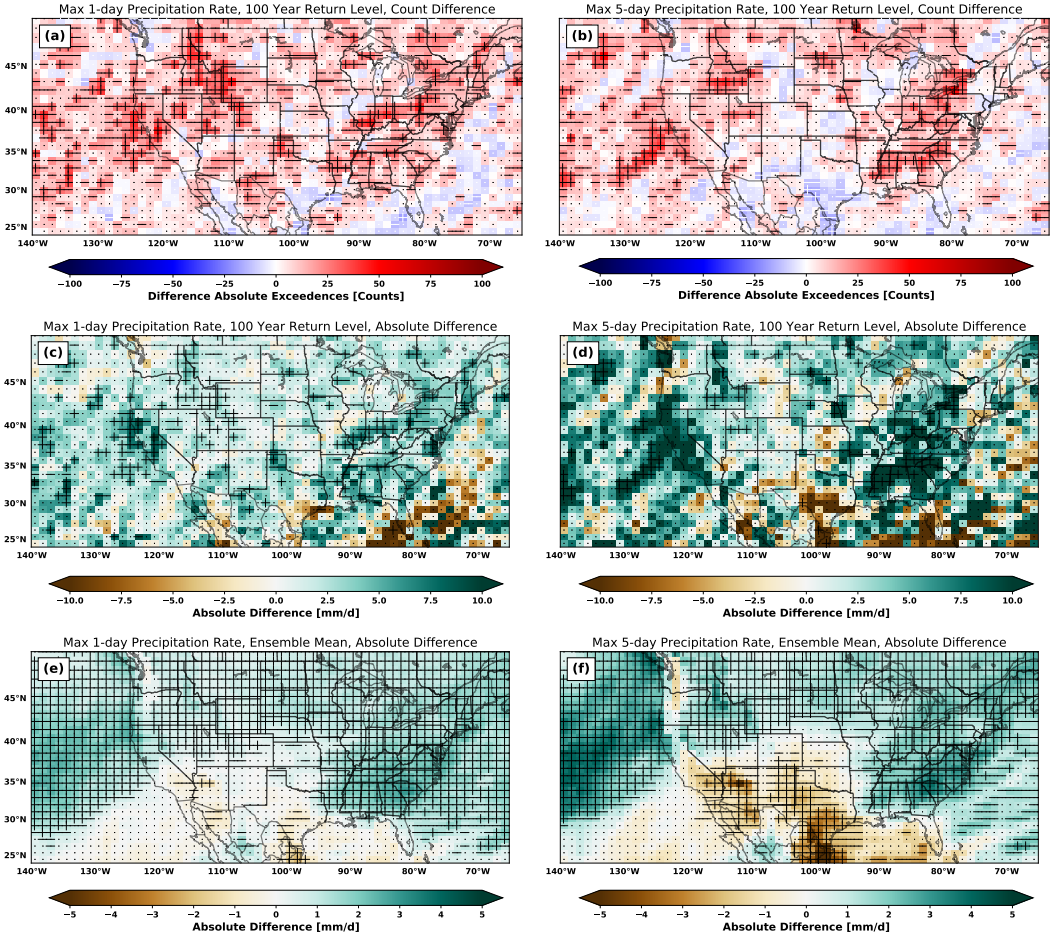

Figure B.1: As in Figure 2.1, but expressed in absolute differences.

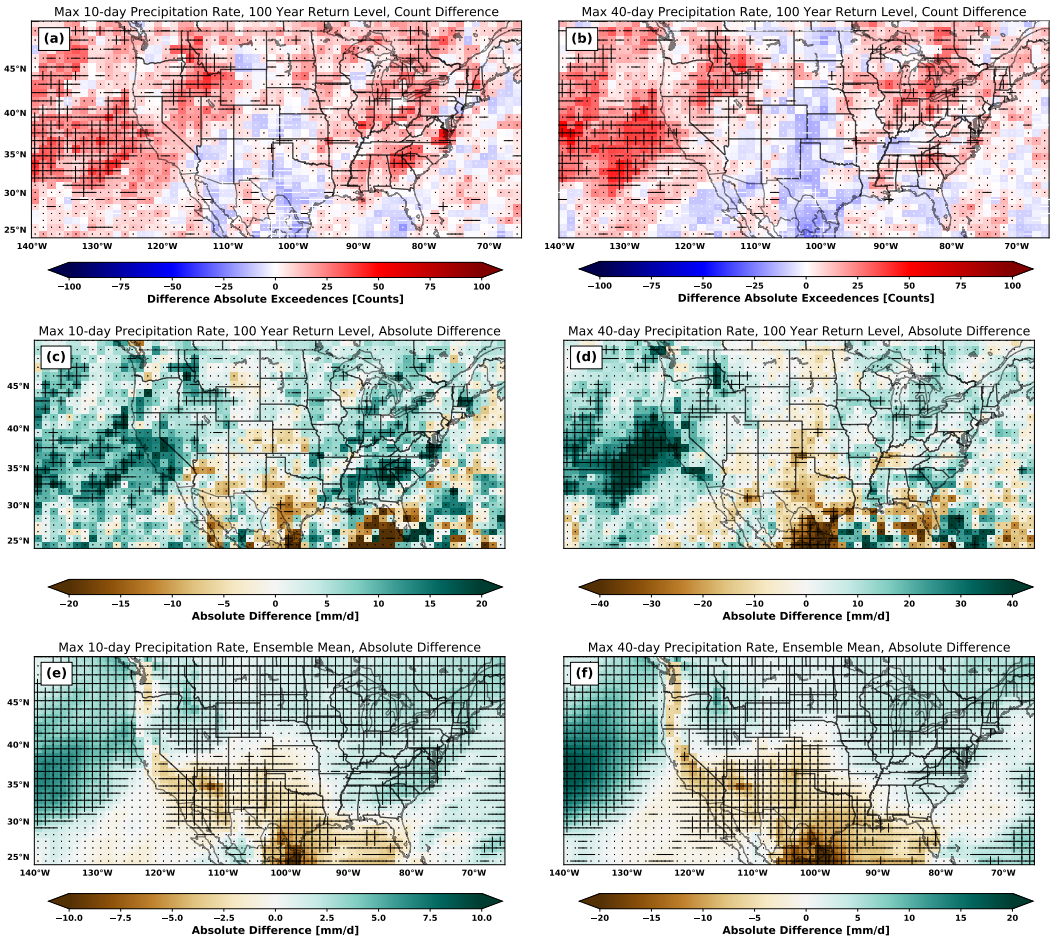

Figure B.2: As in Figure 2.2, but expressed in absolute differences.

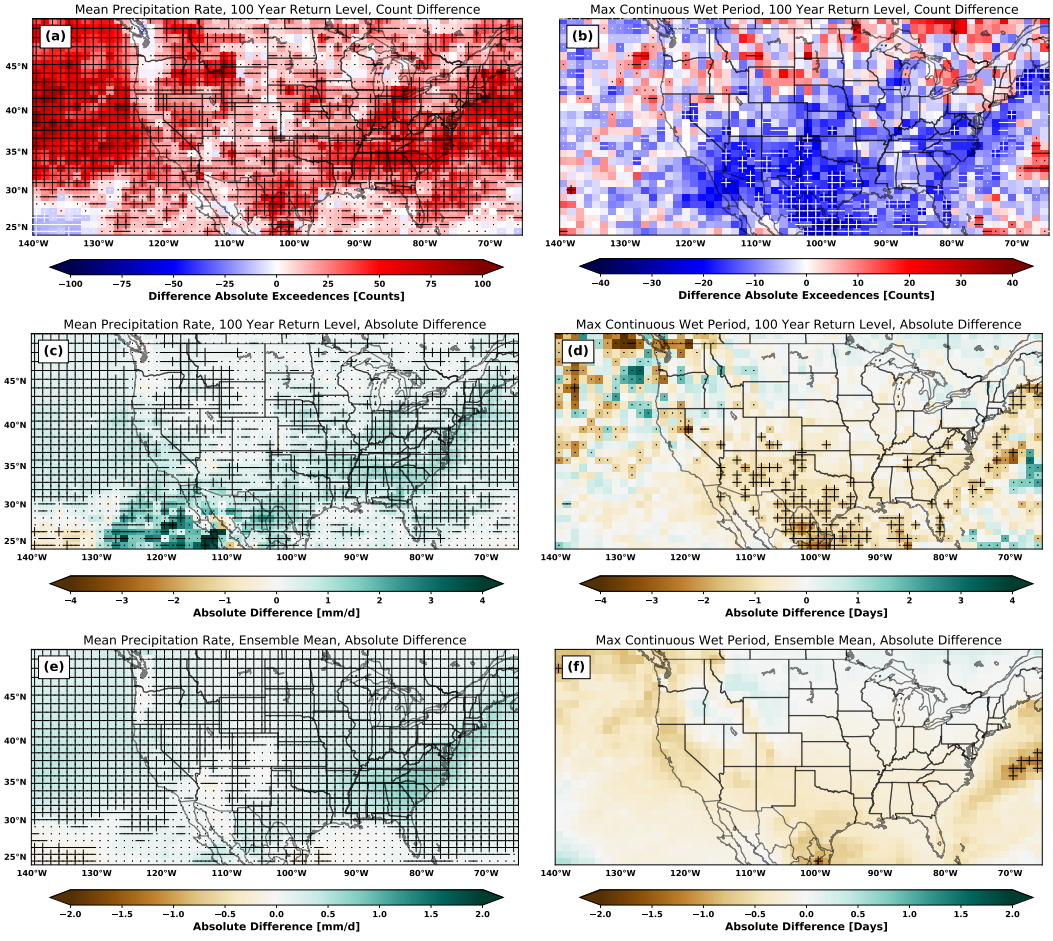

Figure B.3: As in Figure 2.3, but expressed in absolute differences.

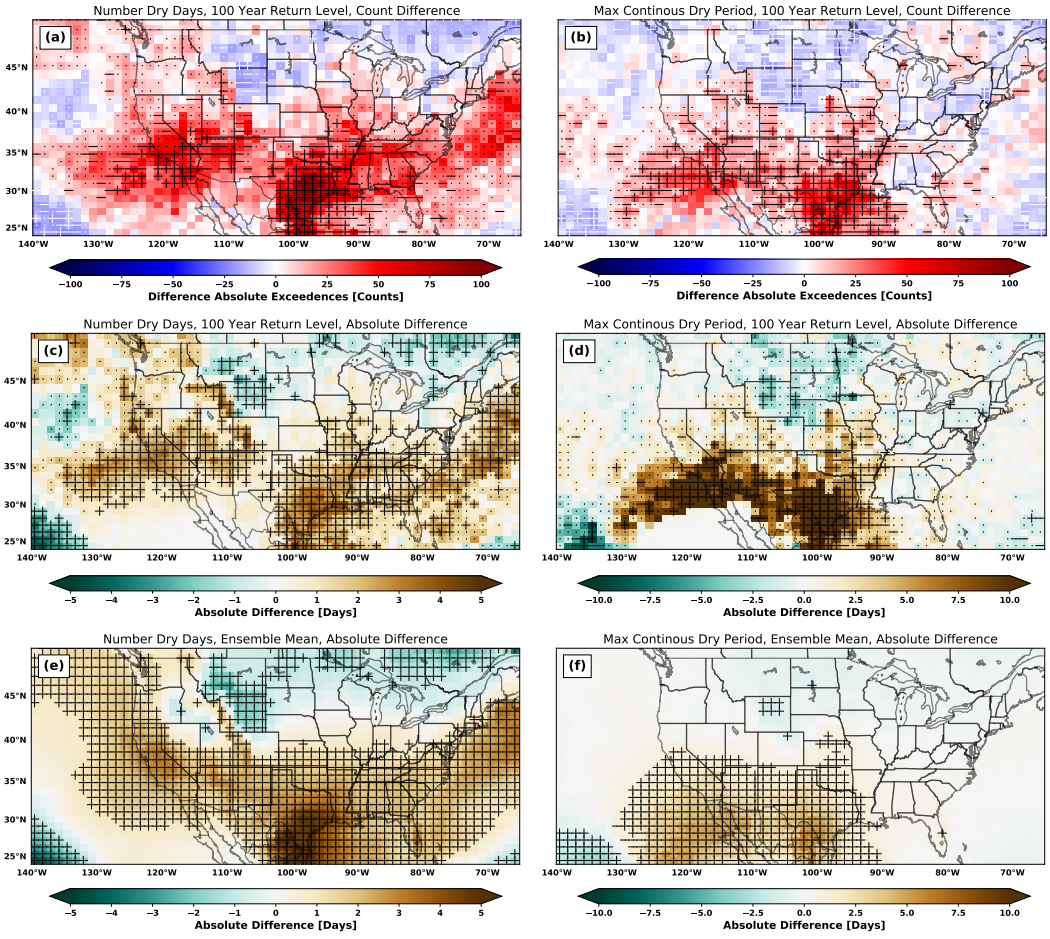

Figure B.4: As in Figure 2.4, but expressed in absolute differences.

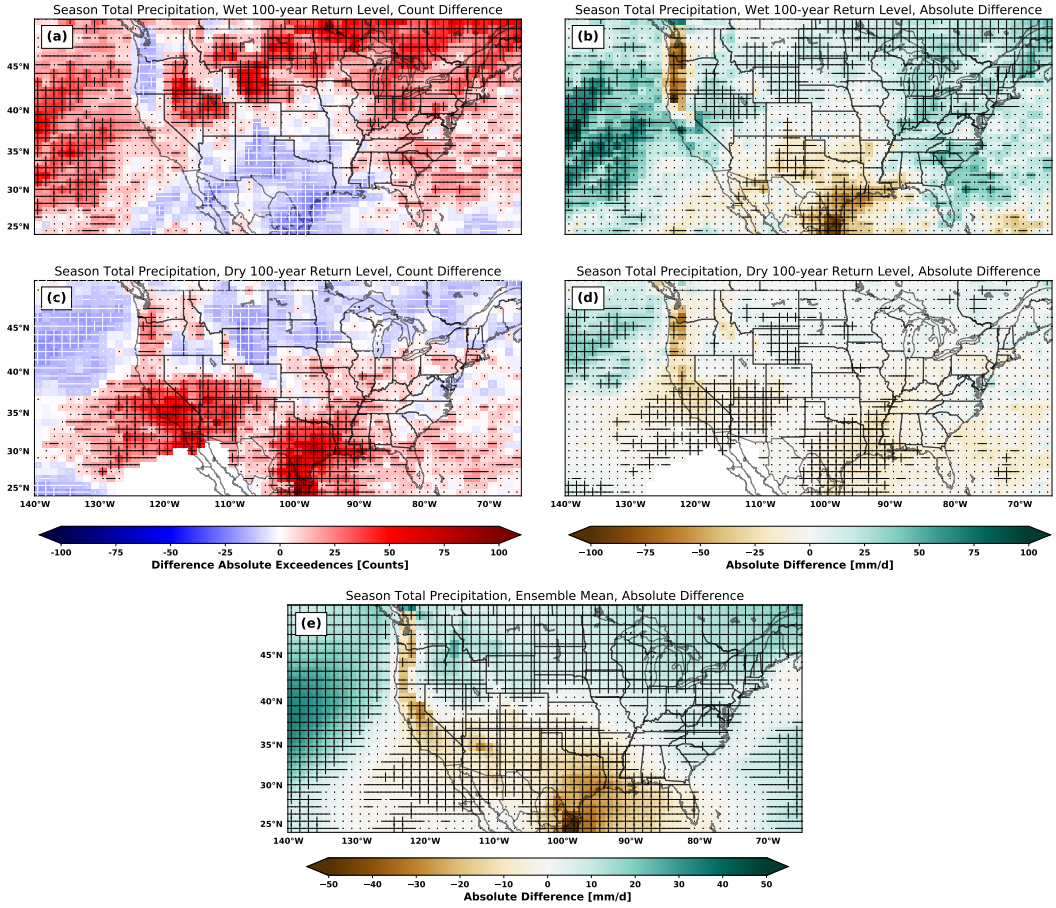

Figure B.5: As in Figure 2.5, but expressed in absolute differences.

Appendix C

Supporting Material for Chapter 3: The Anthropogenic Contribution to Hydrometeorological Variation

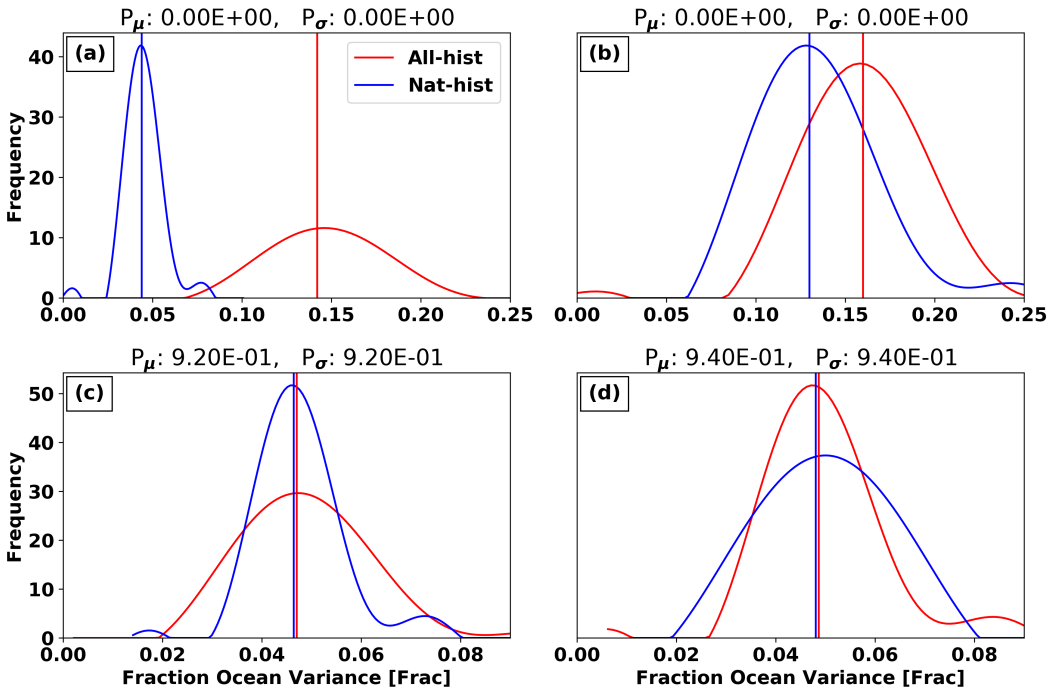

Figure C.1: The distributions of relative fraction of ocean forced variance, referring to the main text Figures 3.1 and 3.3. The distributions reflect the respective fraction of ocean forced variance for the All-hist simulations (Red) and the Nat-hist simulations (Blue). The data come from midlatitude grid points and show four representative cases of change. Panel (a) shows a location showing both a statistically significant change in mean and in the standard deviation (i.e. a stippled location in both Figures 3.1 and 3.3). Panel (b) shows a statistically significant change in the mean but not the standard deviation (i.e. a stippled location in Figure 3.1 but not 3.3). Panel (c) shows a statistically significant change in the standard deviation but not the mean (i.e. a stippled location in Figure 3.3 but not 3.1). Panel (d) shows a location where neither the change in the mean or the standard deviation is significant (i.e. a location which is not stippled in both Figures 3.3 and 3.1). To describe a specific case, panel (a) shows that at that particular location, the average value of the fraction of ocean forced variability in the Nat-hist simulations is approximately 5% (this is what is shown in Figure 3.1), but could range as low as 3% or as high as 8% (this range, as indicated by the standard deviation of the distribution, is what would be reflected in Figure 3.3). At the same location, the All-hist simulations indicate that the average value of the fraction of ocean forced variance is approximately 14%, but could range as low as 7% or as high as 23%.

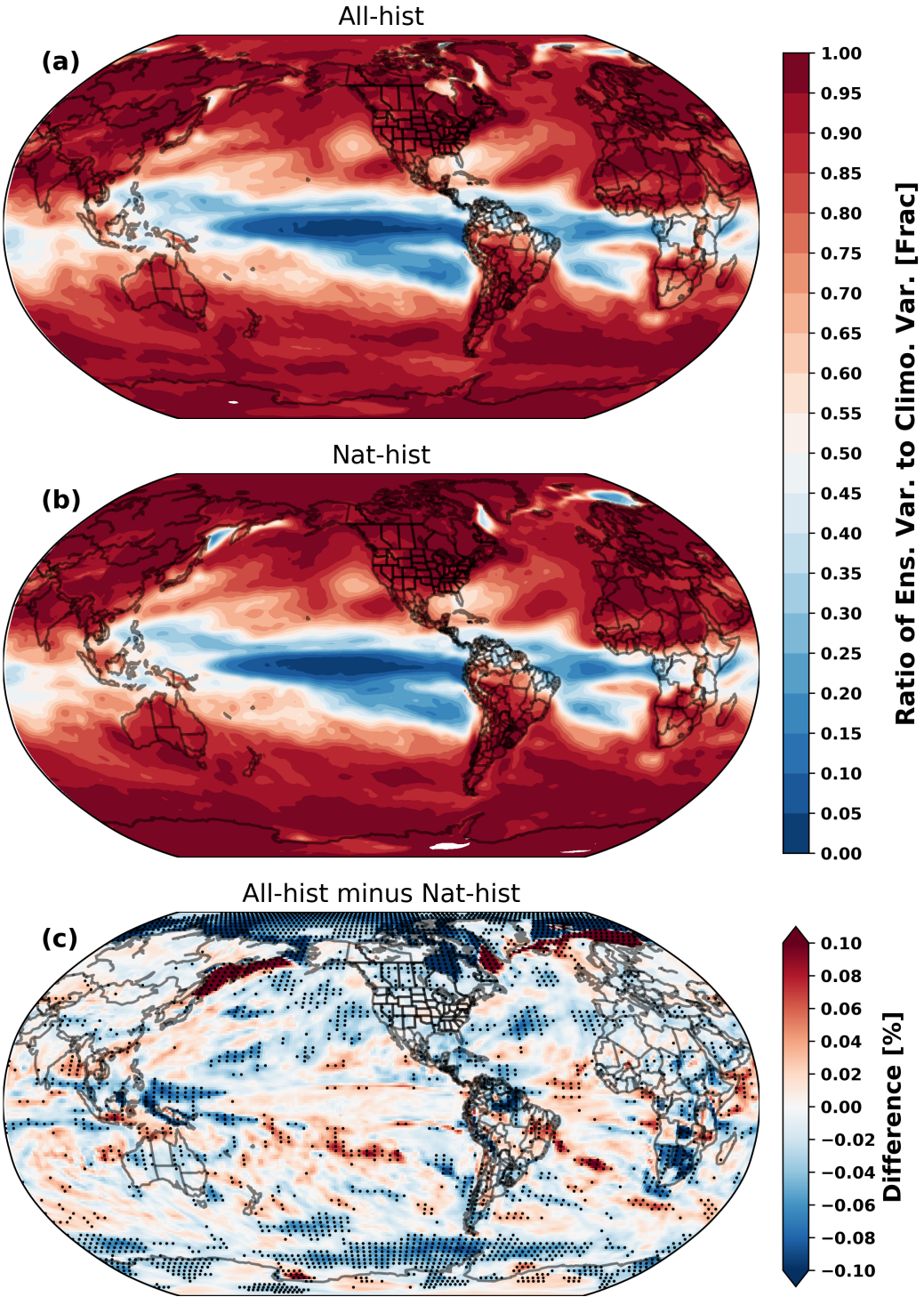

Figure C.2: The ratio of the mean variability across ensemble members to the mean of the climatological variability for each ensemble member, for the All-hist simulations (a), Nat-hist simulations (b), and their difference, All-hist minus Nat-hist (c).

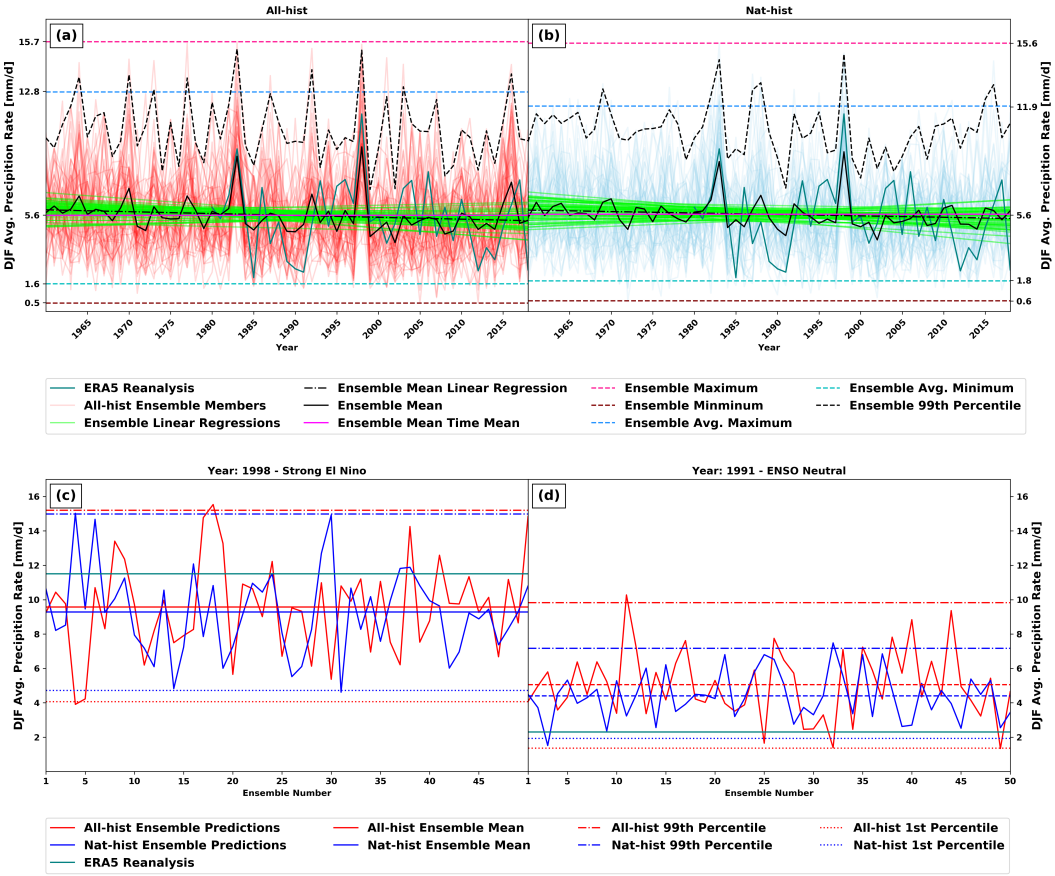

Figure C.3: The data shown here geographically correspond to Bodega Bay, California. Panel (a) shows the realizations for all 50 ensemble members in time from 1960-2018 (red). The Black curve represents the ensemble mean. The ERA5 reanalysis is shown in for when the data exist (olive). The linear regressions on each ensemble realization are plotted in green. The linear regression on the ensemble mean is plotted as the black dash-dot line. The lowest brown horizontal dashed line marks the absolute ensemble minimum. The second lowest cyan line marks the average ensemble minimum. The solid magenta line in the middle marks the time average of the ensemble mean. The dashed black line marks the 99$^{\text{th}}$ percentile of the ensemble realizations. The second to the highest dashed blue line marks the average ensemble maximum. And the highest hot pink dashed line marks the absolute ensemble maximum. Panel (b), as in panel (a) but for the Nat-hist simulations. Panel (c) shows the individual ensemble predictions for the strong El Niño year of 1998. The All-hist members drawn in red, the Nat-hist members in blue. The lowest dotted red/blue line marks the 1st percentile of the All/Nat-hist ensemble estimations. The central horizontal red/blue lines mark the All/Nat-hist ensemble mean prediction. The horizontal olive line represents the ERA5 observation. The two uppermost red/blue dash-dot lines mark the 99$^{\text{th}}$ percentile of the ensemble estimations. Panel (d) as in panel (c) but for the ENSO neutral year of 1991. In panel (a) the correlation of the All/Nat ensemble mean with ERA5 is $r = 0.58$ ($r^2 = 0.34$)/$r = 0.55$ ($r^2 = 0.30$). The maximum correlation with any single All/Nat ensemble member is $r = 0.52$/$r = 0.54$, while the minimum All/Nat correlation is $r = -0.02$/$r = -0.2$

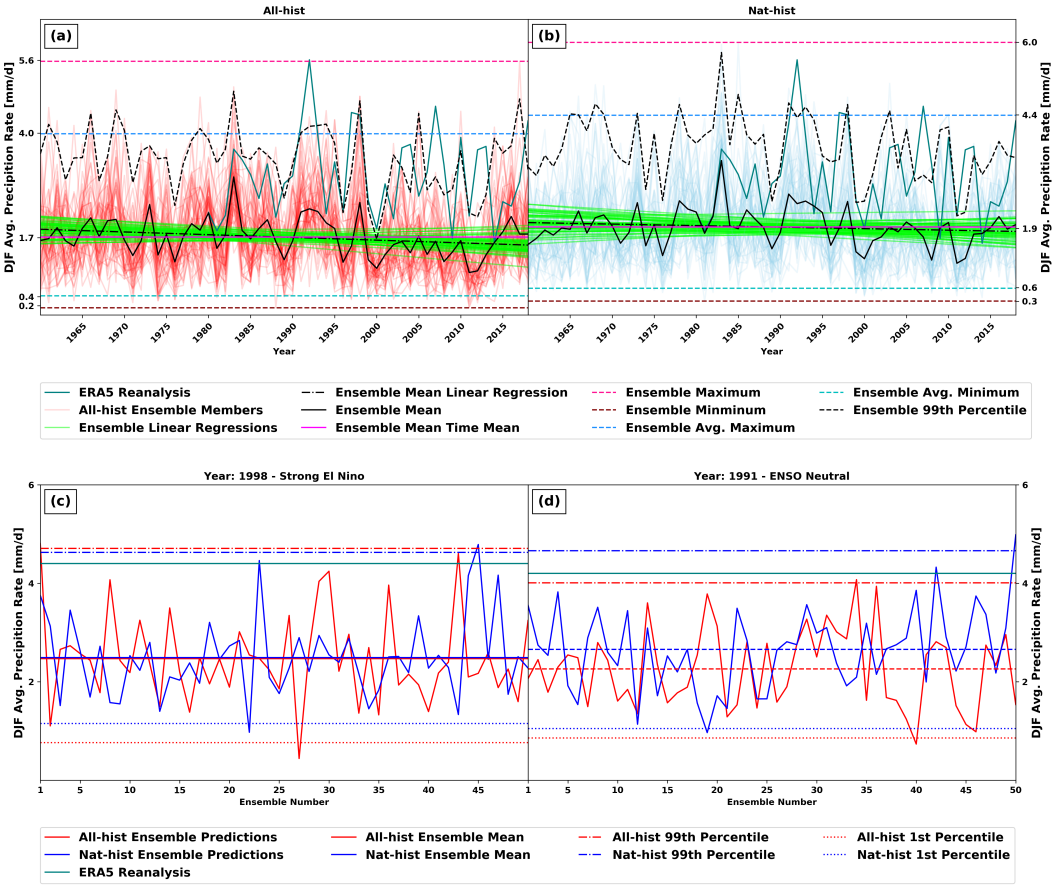

Figure C.4: As in supplementary Figure C.3, but for data representing the geographical location of Houston, Texas. In panel (a) the correlation of the All/Nat ensemble mean with ERA5 is $r = 0.35$ ($r^2 = 0.12$)/$r = 0.33$ ($r^2 = 0.11$). The maximum correlation with any single All/Nat ensemble member is $r = 0.52$/$r = 0.51$, while the minimum All/Nat correlation is $r = -0.12$/$r = -0.23$

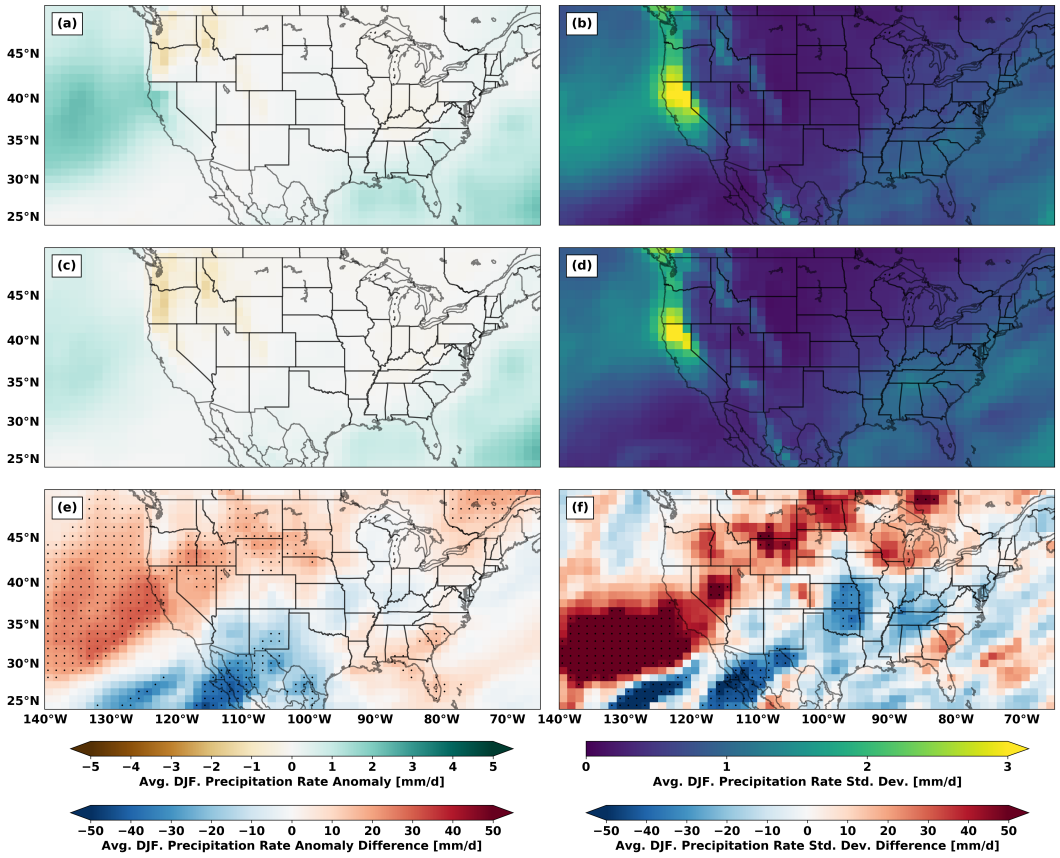

Figure C.5: The simulated outcome for the strong El Niño year of 2015/16 for the All-hist simulations in the top row and the Nat-hist simulations in the bottom row, and their difference along the bottom row. The left column corresponds to the modeled precipitation anomaly and the right column corresponds to the ensemble standard deviation of the simulated average DJF precipitation rate.

Bibliography

Alexander , L. V., Zhang , X., Peterson , T. C., Caesar , J., Gleason , B., Klein Tank , A. M. G., Haylock , M., Collins , D., Trewin , B., Rahimzadeh , F., Tagipour , A., Rupa Kumar , K., Revadekar , J., Griffiths , G., Vincent , L., Stephenson , D. B., Burn , J., Aguilar , E., Brunet , M., Taylor , M., New , M., Zhai , P., Rusticucci , M., and Vazquez-Aguirre , J. L. Global observed changes in daily climate extremes of temperature and precipitation. *Journal of Geophysical Research*, 111(D5):D05109, 2006. ISSN 0148-0227. doi: 10.1029/2005JD006290. URL http://doi.wiley.com/10.1029/2005JD006290. 67

Alexander , M. A., Bladé , I., Newman , M., Lanzante , J. R., Lau , N.-C., and Scott , J. D. The Atmospheric Bridge: The Influence of ENSO Teleconnections on Air–Sea Interaction over the Global Oceans. *Journal of Climate*, 15(16):2205–2231, aug 2002. ISSN 0894-8755. doi: 10.1175/1520-0442(2002)015⟨2205:TABTIO⟩2.0.CO;2. URL https://tinyurl.com/sj5apo7. 106

Allan , R. P. and Soden , B. J. Atmospheric Warming and the Amplification of Precipitation Extremes. *Science*, 321(5895):1481–1484, sep 2008. ISSN 0036-8075. doi: 10.1126/science.1160787. URL http://www.sciencemag.org/lookup/doi/10.1126/science.1160787. 34

Allen , M. R. and Stott , P. A. Estimating signal amplitudes in optimal fingerprinting, part I: theory. *Climate Dynamics*, 21(5-6):477–491, nov 2003. ISSN 0930-7575. doi: 10.1007/s00382-003-0313-9. URL http://link.springer.com/10.1007/s00382-003-0313-9. 35

Allen , M. R. and Ingram , W. J. Constraints on future changes in climate and the hydrologic cycle. *Nature*, 419(6903):228–232, sep 2002. ISSN 0028-0836. doi: 10.1038/nature01092. URL http://www.nature.com/articles/nature01092. 4, 34, 102

Andrews , T., Gregory , J. M., Webb , M. J., and Taylor , K. E. Forcing, feedbacks and climate sensitivity in CMIP5 coupled atmosphere-ocean climate models. *Geophysical Research Letters*, 39(9):n/a–n/a, may 2012. ISSN 00948276. doi: 10.1029/2012GL051607. URL http://doi.wiley.com/10.1029/2012GL051607. 33

Arrhenius , S. On the Influence of Carbonic Acid in the Air upon the Temperature of the Earth. *Publications of the Astronomical Society of the Pacific*, 9(May):14, feb 1897. ISSN 0004-6280. doi: 10.1086/121158. URL http://iopscience.iop.org/article/10.1086/121158. 33

Barnes , E. A. and Screen , J. A. The impact of Arctic warming on the midlatitude jet-stream: Can it? Has it? Will it? *Wiley Interdisciplinary Reviews: Climate Change*, 6(3):277–286, may 2015. ISSN 17577780. doi: 10.1002/wcc.337. URL http://doi.wiley.com/10.1002/wcc.337. 4

Barnes , E. A., Dunn-Sigouin , E., Masato , G., and Woollings , T. Exploring recent trends in Northern Hemisphere blocking. *Geophysical Research Letters*, 41(2):638–644, jan 2014. ISSN 00948276. doi: 10.1002/2013GL058745. URL http://doi.wiley.com/10.1002/2013GL058745. 60

Barnett , T. P., Pierce , D. W., AchutaRao , K. M., Gleckler , P. J., Santer , B. D., and Gregory , J. M. Penetration of Human-Induced Warming into the World's Oceans. *Science*, 309(5732):284–287, jul 2005a. ISSN 0036-8075. doi: 10.1126/science.1112418. URL http://www.sciencemag.org/cgi/doi/10.1126/science.1112418. 36

Barnett , T., Zwiers , F., Hengerl , G., Allen , M., Crowly , T., Gillett , N., Hasselmann , K., Jones , P., Santer , B., Schnur , R., Scott , P., Taylor , K., and Tett , S. Detecting and Attributing External Influences on the Climate System: A Review of Recent Advances. *Journal of Climate*, 18(9):1291–1314, may 2005b. ISSN 0894-8755. doi: 10.1175/JCLI3329.1. URL http://journals.ametsoc.org/doi/abs/10.1175/JCLI3329.1. 35

Basu , R. Relation between Elevated Ambient Temperature and Mortality: A Review of the Epidemiologic Evidence. *Epidemiologic Reviews*, 24(2):190–202, dec 2002. ISSN 0193-936X. doi: 10.1093/epirev/mxf007. URL https://academic.oup.com/epirev/article-lookup/doi/10.1093/epirev/mxf007. 5

Bell , J. E., Brown , C. L., Conlon , K., Herring , S., Kunkel , K. E., Lawrimore , J., Luber , G., Schreck , C., Smith , A., and Uejio , C. Changes in extreme events and the potential impacts on human health. *Journal of the Air & Waste Management Association*, 68(4):265–287, apr 2018. ISSN 1096-2247. doi: 10.1080/10962247.2017.1401017. URL https://doi.org/10.1080/10962247.2017.1401017. 37

Benjamini , Y. and Hochberg , Y. Controlling the False Discovery Rate : a Practical and Powerful Approach to Multiple Testing. *Journal of the Royal Statistical Society. Series B (Methodological)*, 57(1):289–300, 1995. URL http://www.jstor.org/stable/2346101. 48, 79

Burch , G. J., Moore , I. D., and Burns , J. Soil hydrophobic effects on infiltration and catchment runoff. *Hydrological Processes*, 3(3):211–222, jul 1989. ISSN 08856087. doi: 10.1002/hyp.3360030302. URL http://doi.wiley.com/10.1002/hyp.3360030302. 72

Burgers , G. and Stephenson , D. B. The "normality" of El Niño. *Geophysical Research Letters*, 26(8):1027–1030, apr 1999. ISSN 00948276. doi: 10.1029/1999GL900161. URL http://doi.wiley.com/10.1029/1999GL900161. 73

CAL FIRE. , H. W. A. S. R. 2015 Wildfire Activity Statistics Annual Report, 2015. URL http://www.fire.ca.gov/downloads/redbooks/2015{_}Redbook/2015{_}Redbook{_}FINAL.PDF. 2

California Department of Water Resources . Water Year 2017: What a Difference a Year Makes. (September):11, 2017. URL http://water.ca.gov/waterconditions/docs/2017/WaterYear2017.pdf. 72

Capotondi , A., Wittenberg , A. T., Newman , M., Di Lorenzo , E., Yu , J.-Y., Braconnot , P., Cole , J., Dewitte , B., Giese , B., Guilyardi , E., Jin , F.-F., Karnauskas , K., Kirtman , B., Lee , T., Schneider , N., Xue , Y., and Yeh , S.-W. Understanding ENSO Diversity. *Bulletin of the American Meteorological Society*, 96(6):921–938, jun 2015. ISSN 0003-0007. doi: 10.1175/BAMS-D-13-00117.1. URL http://journals.ametsoc.org/doi/10.1175/BAMS-D-13-00117.1. 105

Cassardo , C., Mercalli , L., and Berro , D. C. Characteristics of the Summer 2003 Heat Wave in Piedmont, Italy, and its Effects on Water Resources. *Journal of the Korean Meteorological Society*, 43(3):195–221, 2007. URL https://tinyurl.com/t9a388j. 2

Changnon , S. D. Measures of Economic Impacts of Weather Extremes. *Bulletin of the American Meteorological Society*, 84(9):1231–1236, sep 2003. ISSN 0003-0007. doi: 10.1175/BAMS-84-9-1231. URL http://journals.ametsoc.org/doi/10.1175/BAMS-84-9-1231. 37

Copernicus Climate Change Service Climate Data Store (CDS) . Copernicus Climate Change Service (C3S): ERA5: Fifth generation of ECMWF atmospheric reanalyses of the global climate, 2017. URL https://tinyurl.com/https-cds-climate-copernicus. 78

Corringham , T. W. and Cayan , D. R. The Effect of El Niño on Flood Damages in the Western United States. *Weather, Climate, and Society*, 11(3):489–504, jul 2019. ISSN 1948-8327. doi: 10.1175/WCAS-D-18-0071.1. URL http://journals.ametsoc.org/doi/10.1175/WCAS-D-18-0071.1. 110

Curriero , F. C., Patz , J. A., Rose , J. B., and Lele , S. The Association Between Extreme Precipitation and Waterborne Disease Outbreaks in the United States, 1948–1994. *American Journal of Public Health*, 91(8):1194–1199, aug 2001. ISSN 0090-0036. doi: 10.2105/AJPH.91.8.1194. URL http://ajph.aphapublications.org/doi/10.2105/AJPH.91.8.1194. 5

Davy , R. and Esau , I. Global climate models' bias in surface temperature trends and variability. *Environmental Research Letters*, 9(11): 114024, nov 2014. ISSN 1748-9326. doi: 10.1088/1748-9326/9/11/114024. URL http://stacks.iop.org/1748-9326/9/i=11/a=114024?key=crossref.62a944a006fca4eb162e69a83af29733. 45

Deser , C., Phillips , A. S., and Hurrell , J. W. Pacific Interdecadal Climate Variability: Linkages between the Tropics and the North Pacific during Boreal Winter since 1900. *Journal of Climate*, 17(16):3109–3124, aug 2004. ISSN 0894-8755. doi: 10.1175/1520-0442(2004)017⟨3109:PICVLB⟩2.0.CO;2. URL https://tinyurl.com/uwt7e9t. 40

Deser , C., Phillips , A., Bourdette , V., and Teng , H. Uncertainty in climate change projections: The role of internal variability. *Climate Dynamics*, 38(3-4): 527–546, feb 2012. ISSN 09307575. doi: 10.1007/s00382-010-0977-x. URL http://link.springer.com/10.1007/s00382-010-0977-x. 81

Deser , C., Phillips , A. S., Alexander , M. A., and Smoliak , B. V. Projecting North American Climate over the Next 50 Years: Uncertainty due to Internal Variability*. *Journal of Climate*, 27(6):2271–2296, mar 2014. ISSN 0894-8755. doi: 10.1175/JCLI-D-13-00451.1. URL http://journals.ametsoc.org/doi/abs/10.1175/JCLI-D-13-00451.1. 40, 62

Dettinger , M. Climate Change, Atmospheric Rivers, and Floods in California - A Multimodel Analysis of Storm Frequency and Magnitude Changes. *JAWRA Journal of the American Water Resources Association*, 47(3):514–523, jun 2011. ISSN 1093474X. doi: 10.1111/j.1752-1688.2011.00546.x. URL http://doi.wiley.com/10.1111/j.1752-1688.2011.00546.x. 70

Dettinger , M. D. Atmospheric Rivers as Drought Busters on the U.S. West Coast. *Journal of Hydrometeorology*, 14(6):1721–1732, dec 2013. ISSN 1525-755X. doi: 10.1175/JHM-D-13-02.1. URL http://journals.ametsoc.org/doi/abs/10.1175/JHM-D-13-02.1. 54

Díaz , J., Jordán , A., García , R., López , C., Alberdi , J., Hernández , E., and Otero , A. Heat waves in Madrid 1986–1997: effects on the health of the elderly. *International Archives of Occupational and Environmental Health*, 75(3):163–170, mar 2002. ISSN 0340-0131. doi: 10.1007/s00420-001-0290-4. URL http://link.springer.com/10.1007/s00420-001-0290-4. 5

Dittus , A. J., Karoly , D. J., Lewis , S. C., Alexander , L. V., and Donat , M. G. A Multiregion Model Evaluation and Attribution Study of Historical Changes in the Area Affected by Temperature and Precipitation Extremes. *Journal of Climate*, 29(23):8285–8299, dec 2016. ISSN 0894-8755. doi: 10.1175/JCLI-D-16-0164.1. URL http://journals.ametsoc.org/doi/10.1175/JCLI-D-16-0164.1. 37

Dittus , A. J., Karoly , D. J., Donat , M. G., Lewis , S. C., and Alexander , L. V. Understanding the role of sea surface temperature-forcing for variability in global temperature and precipitation extremes. *Weather and Climate Extremes*, 21 (August 2017):1–9, sep 2018. ISSN 22120947. doi: 10.1016/j.wace.2018.06.002. URL https://doi.org/10.1016/j.wace.2018.06.002. 85

Du , H., Alexander , L. V., Donat , M. G., Lippmann , T., Srivastava , A., Salinger , J., Kruger , A., Choi , G., He , H. S., Fujibe , F., Rusticucci , M., Nandintsetseg , B., Manzanas , R., Rehman , S., Abbas , F., Zhai , P., Yabi , I., Stambaugh , M. C., Wang , S., Batbold , A., Oliveira , P. T., Adrees , M., Hou , W., Zong , S., Santos e Silva , C. M., Lucio , P. S., and Wu , Z. Precipitation from Persistent Extremes is Increasing in Most Regions and Globally. *Geophysical Research Letters*, pages 1–9, may 2019. ISSN 0094-8276. doi: 10.1029/2019GL081898. URL https://onlinelibrary.wiley.com/doi/abs/10.1029/2019GL081898. 60

Easterling , D. R. Climate Extremes: Observations, Modeling, and Impacts. *Science*, 289(5487):2068–2074, sep 2000. ISSN 00368075. doi: 10.1126/science.289.5487.2068. URL http://www.sciencemag.org/cgi/doi/10.1126/science.289.5487.2068. 38

Easterling , D., Arnold , J., Knutson , T., Kunkel , K., LeGrande , A., Leung , L., Vose , R., Waliser , D., and Wehner , M. Ch. 7: Precipitation Change in the United States. Climate Science Special Report: Fourth National Climate Assessment, Volume I. Technical report, U.S. Global Change Research Program, Washington, DC, 2017. URL https://science2017.globalchange.gov/chapter/7/. 37

EM-DAT . The International Disaster Database, 2016. URL http://www.emdat.be/. 5

Emori , S. and Brown , S. J. Dynamic and thermodynamic changes in mean and extreme precipitation under changed climate. *Geophysical Research Letters*, 32 (17):1–5, sep 2005. ISSN 00948276. doi: 10.1029/2005GL023272. URL http://doi.wiley.com/10.1029/2005GL023272. 74

Fischer , E. M. and Knutti , R. Anthropogenic contribution to global occurrence of heavy-precipitation and high-temperature extremes. *Nature Climate Change*, 5(6):560–564, jun 2015. ISSN 1758-678X. doi: 10.1038/nclimate2617. URL http://www.nature.com/articles/nclimate2617. 3

Flato , G., Marotzke , J., Abiodun , B., Braconnot , P., Chou , S. C., Collins , W., Cox , P., Driouech , F., Emori , S., Eyring , V., Forest , C., Gleckler , P., Guilyardi , E., Jakob , C., Kattsov , V., Reason , C., and Rummukainen , M. *Climate Change 2013 - The Physical Science Basis*. Cambridge University Press, Cambridge, 2014. ISBN 9781107415324. doi: 10.1017/CBO9781107415324. URL http://ebooks.cambridge.org/ref/id/CBO9781107415324. 3, 4

Folland , C., Stone , D., Frederiksen , C., Karoly , D., and Kinter , J. The International CLIVAR Climate of the 20th Century Plus (C20C+) Project: Report of the Sixth Workshop. *CLIVAR Exchanges*, 19(2):57–59, 2014. URL https://tinyurl.com/https-crd-lbl-gov-assets-pub. 39, 41, 77

Francis , J. and Skific , N. Evidence linking rapid Arctic warming to mid-latitude weather patterns. *Philosophical Transactions of the Royal Society A: Mathematical, Physical and Engineering Sciences*, 373(2045):20140170, jul 2015. ISSN 1364-503X. doi: 10.1098/rsta.2014.0170. URL https://royalsocietypublishing.org/doi/10.1098/rsta.2014.0170. 60

Frich , P., Alexander , L., Della-Marta , P., Gleason , B., Haylock , M., Klein Tank , A., and Peterson , T. Observed coherent changes in climatic extremes during the second half of the twentieth century. *Climate Research*, 19(3):193–212, 2002. ISSN 0936-577X. doi: 10.3354/cr019193. URL http://www.int-res.com/abstracts/cr/v19/n3/p193-212/. 3

Gates , W. L. AMIP: The Atmospheric Model Intercomparison Project. *Bulletin of the American Meteorological Society*, 73(12):1962–1970, dec 1992. ISSN 0003-0007. doi: 10.1175/1520-0477(1992)073⟨1962:ATAMIP⟩2.0.CO;2. URL https://tinyurl.com/vsxrqnf. 41

Gershunov , A., Shulgina , T., Clemesha , R. E. S., Guirguis , K., Pierce , D. W., Dettinger , M. D., Lavers , D. A., Cayan , D. R., Polade , S. D., Kalansky , J., and Ralph , F. M. Precipitation regime change in Western North America: The role of Atmospheric Rivers. *Scientific Reports*, 9(1):9944, dec 2019. ISSN 2045-2322. doi: 10.1038/s41598-019-46169-w. URL http://www.nature.com/articles/s41598-019-46169-w. 75, 93, 98, 113

Gillett , N. P., Zwiers , F. W., Weaver , A. J., and Stott , P. A. Detection of human influence on sea-level pressure. *Nature*, 422(6929):292–294, mar 2003. ISSN 0028-0836. doi: 10.1038/nature01487. URL http://www.nature.com/articles/nature01487. 35

Gillett , N. P., Shiogama , H., Funke , B., Hegerl , G., Knutti , R., Matthes , K., Santer , B. D., Stone , D., and Tebaldi , C. The Detection and Attribution Model Intercomparison Project (DAMIP v1.0) contribution to CMIP6. *Geoscientific Model Development*, 9(10):3685–3697, oct 2016. ISSN 1991-9603. doi: 10.5194/gmd-9-3685-2016. URL https://www.geosci-model-dev.net/9/3685/2016/. 42

Glantz , M. H. Hurricane Katrina as a "teachable moment". *Advances in Geosciences*, 14:287–294, apr 2008. ISSN 1680-7359. doi: 10.5194/adgeo-14-287-2008. URL https://www.adv-geosci.net/14/287/2008/. 2

Gochis , D., Schumacher , R., Friedrich , K., Doesken , N., Kelsch , M., Sun , J., Ikeda , K., Lindsey , D., Wood , A., Dolan , B., Matrosov , S., Newman , A., Mahoney , K., Rutledge , S., Johnson , R., Kucera , P., Kennedy , P., Sempere-Torres , D., Steiner , M., Roberts , R., Wilson , J., Yu , W., Chandrasekar , V., Rasmussen , R., Anderson , A., and Brown , B. The Great Colorado Flood of September 2013. *Bulletin of the American Meteorological Society*, 96(9):1461–1487, sep 2015. ISSN 0003-0007. doi: 10.1175/BAMS-D-13-00241.1. URL http://journals.ametsoc.org/doi/10.1175/BAMS-D-13-00241.1. 38

Hegerl , G. C., Hasselmann , K., Cubasch , U., Mitchell , J. F. B., Roeckner , E., Voss , R., and Waszkewitz , J. Multi-fingerprint direction and attribution analysis of greenhouse gas, greenhouse gas-plus-aerosol and solar forced climate change. *Climate Dynamics*, 14(1):71–72, dec 1997. ISSN 0930-7575. doi: 10.1007/s003820050209. URL http://link.springer.com/10.1007/s003820050209. 35

Hegerl , G. and Zwiers , F. Use of models in detection and attribution of climate change. *Wiley Interdisciplinary Reviews: Climate Change*, 2(4):570–591, jul 2011. ISSN 17577780. doi: 10.1002/wcc.121. URL http://doi.wiley.com/10.1002/wcc.121. 35

Hegerl , G. C. and North , G. R. Comparison of Statistically Optimal Approaches to Detecting Anthropogenic Climate Change. *Journal of Climate*, 10(5):1125–1133, may 1997. ISSN 0894-8755. doi: 10.1175/1520-0442(1997)010⟨1125:COSOAT⟩2.0.CO;2. URL https://tinyurl.com/rerp7lt. 35

Hegerl , G. C., von Storch , H., Hasselmann , K., Santer , B. D., Cubasch , U., and Jones , P. D. Detecting Greenhouse-Gas-Induced Climate Change with an Optimal Fingerprint Method. *Journal of Climate*, 9(10):2281–2306, oct 1996. ISSN 0894-8755. doi: 10.1175/1520-0442(1996)009⟨2281:DGGICC⟩2.0.CO;2. URL https://tinyurl.com/t2jelbm. 35

Held , I. M. and Soden , B. J. Robust Responses of the Hydrological Cycle to Global Warming. *Journal of Climate*, 19(21):5686–5699, nov 2006. ISSN 0894-8755. doi: 10.1175/JCLI3990.1. URL http://journals.ametsoc.org/doi/abs/10.1175/JCLI3990.1. 4, 34, 52

Hennessy , K. J., Gregory , J. M., and Mitchell , J. F. B. Changes in daily precipitation under enhanced greenhouse conditions. *Climate Dynamics*, 13(9): 667–680, sep 1997. ISSN 0930-7575. doi: 10.1007/s003820050189. URL http://link.springer.com/10.1007/s003820050189. 34

Higgins , R. W. and Kousky , V. E. Changes in Observed Daily Precipitation over the United States between 1950–79 and 1980–2009. *Journal of Hydrometeorology*, 14(1):105–121, feb 2013. ISSN 1525-755X. doi: 10.1175/JHM-D-12-062.1. URL http://journals.ametsoc.org/doi/abs/10.1175/JHM-D-12-062.1. 37

Hoerling , M., Kumar , A., Dole , R., Nielsen-Gammon , J. W., Eischeid , J., Perlwitz , J., Quan , X.-W., Zhang , T., Pegion , P., and Chen , M. Anatomy of an Extreme Event. *Journal of Climate*, 26(9):2811–2832, may 2013. ISSN 0894-8755. doi: 10.1175/JCLI-D-12-00270.1. URL http://journals.ametsoc.org/doi/abs/10.1175/JCLI-D-12-00270.1. 62

Hoerling , M., Eischeid , J., Perlwitz , J., Quan , X.-W., Wolter , K., and Cheng , L. Characterizing Recent Trends in U.S. Heavy Precipitation. *Journal of Climate*, 29(7):2313–2332, apr 2016. ISSN 0894-8755. doi: 10.1175/JCLI-D-15-0441.1. URL http://journals.ametsoc.org/doi/10.1175/JCLI-D-15-0441.1. 39, 45

Hoerling , M. P., Kumar , A., and Zhong , M. El Niño, La Niña, and the Nonlinearity of Their Teleconnections. *Journal of Climate*, 10(8):1769–1786, aug 1997. ISSN 0894-8755. doi: 10.1175/1520-0442(1997)010⟨1769:ENOLNA⟩2.0.CO;2. URL https://tinyurl.com/t9c4nub. 73

Hoskins , B. and Woollings , T. Persistent Extratropical Regimes and Climate Extremes. *Current Climate Change Reports*, 1(3):115–124, sep 2015. ISSN 2198-6061. doi: 10.1007/s40641-015-0020-8. URL http://link.springer.com/10.1007/s40641-015-0020-8. 60

IPCC . *Managing the Risks of Extreme Events and Disasters to Advance Climate Change Adaptation. A Special Report of Working Groups I and II of the Intergovernmental Panel on Climate Change [Field, C.B., V. Barros, T.F. Stocker, D. Qin, D.J. Dokken, K.L. Ebi, M.D.* Cambridge University Press, Cambridge, UK, and New York, NY, USA, 2012. ISBN 9781139177245. doi: 10.1017/CBO9781139177245. URL http://ebooks.cambridge.org/ref/id/CBO9781139177245. 2

Karl , T. R. and Knight , R. W. Secular Trends of Precipitation Amount, Frequency, and Intensity in the United States. *Bulletin of the American Meteorological Society*, 79(2):231–241, feb 1998. ISSN 0003-0007. doi: 10.1175/1520-0477(1998)079⟨0231:STOPAF⟩2.0.CO;2. URL https://tinyurl.com/ror43bm. 34, 37

Karl , T. R., Knight , R. W., and Plummer , N. Trends in high-frequency climate variability in the twentieth century. *Nature*, 377(6546):217–220, sep 1995. ISSN 0028-0836. doi: 10.1038/377217a0. URL http://www.nature.com/articles/377217a0. 114

Kay , J. E., Hillman , B. R., Klein , S. A., Zhang , Y., Medeiros , B., Pincus , R., Gettelman , A., Eaton , B., Boyle , J., Marchand , R., and Ackerman , T. P. Exposing Global Cloud Biases in the Community Atmosphere Model (CAM) Using Satellite Observations and Their Corresponding Instrument Simulators. *Journal of Climate*, 25(15):5190–5207, aug 2012. ISSN 0894-8755. doi: 10.1175/JCLI-D-11-00469.1. URL http://journals.ametsoc.org/doi/abs/10.1175/JCLI-D-11-00469.1. 45

Kelley , C. P., Mohtadi , S., Cane , M. A., Seager , R., and Kushnir , Y. Climate change in the Fertile Crescent and implications of the recent Syrian drought. *Proceedings of the National Academy of Sciences*, 112(11):3241–3246, mar 2015. ISSN 0027-8424. doi: 10.1073/pnas.1421533112. URL http://www.pnas.org/content/112/11/3241.abstract. 6

Kirchmeier-Young , M. C., Wan , H., Zhang , X., and Seneviratne , S. I. Importance of Framing for Extreme Event Attribution: The Role of Spatial and Temporal Scales. *Earth's Future*, page 2019EF001253, oct 2019. ISSN 2328-4277. doi: 10.1029/2019EF001253. URL https://onlinelibrary.wiley.com/doi/abs/10.1029/2019EF001253. 45

Koopman , P. A. R. Confidence Intervals for the Ratio of Two Binomial Proportions. *Biometrics*, 40(2):513, jun 1984. ISSN 0006341X. doi: 10.2307/2531405. URL https://www.jstor.org/stable/2531405?origin=crossref. 46

Koster , R. D., Suarez , M. J., and Heiser , M. Variance and Predictability of Precipitation at Seasonal-to-Interannual Timescales. *Journal of Hydrometeorology*, 1(1):26–46, feb 2000. ISSN 1525-755X. doi: 10.1175/1525-7541(2000)001⟨0026:VAPOPA⟩2.0.CO;2. URL https://tinyurl.com/srf32bw. 81

Kunkel , K. E., Pielke , R. A., and Changnon , S. A. Temporal Fluctuations in Weather and Climate Extremes That Cause Economic and Human Health Impacts: A Review. *Bulletin of the American Meteorological Society*, 80(6):1077–1098, jun 1999. ISSN 0003-0007. doi: 10.1175/1520-0477(1999)080⟨1077:TFIWAC⟩2.0.CO;2. URL https://tinyurl.com/rofkpu9. 4, 36, 37, 72

Kunkel , K. E., Easterling , D. R., Redmond , K., and Hubbard , K. Temporal variations of extreme precipitation events in the United States: 1895-2000. *Geophysical Research Letters*, 30(17):n/a–n/a, sep 2003. ISSN 00948276. doi: 10.1029/2003GL018052. URL http://doi.wiley.com/10.1029/2003GL018052. 39

Kunkel , K. E., Karl , T. R., Brooks , H., Kossin , J., Lawrimore , J. H., Arndt , D., Bosart , L., Changnon , D., Cutter , S. L., Doesken , N., Emanuel , K., Groisman , P. Y., Katz , R. W., Knutson , T., O'Brien , J., Paciorek , C. J., Peterson , T. C., Redmond , K., Robinson , D., Trapp , J., Vose , R., Weaver , S., Wehner , M., Wolter , K., and Wuebbles , D. Monitoring and Understanding Trends in Extreme Storms: State of Knowledge. *Bulletin of the American Meteorological Society*, 94(4):499–514, apr 2013. ISSN 0003-0007. doi: 10.1175/BAMS-D-11-00262.1. URL http://journals.ametsoc.org/doi/abs/10.1175/BAMS-D-11-00262.1. 34, 37

Lambert , F. H., Stott , P. A., Allen , M. R., and Palmer , M. A. Detection and attribution of changes in 20th century land precipitation. *Geophysical Research Letters*, 31(10):n/a–n/a, may 2004. ISSN 00948276. doi: 10.1029/2004GL019545. URL http://doi.wiley.com/10.1029/2004GL019545. 34

Langenbrunner , B., Neelin , J. D., Lintner , B. R., and Anderson , B. T. Patterns of precipitation change and climatological uncertainty among CMIP5 models, with a focus on the midlatitude pacific storm track. *Journal of Climate*, 28(19): 7857–7872, oct 2015. ISSN 08948755. doi: 10.1175/JCLI-D-14-00800.1. URL http://journals.ametsoc.org/doi/10.1175/JCLI-D-14-00800.1. 98

Lee , S.-K., Lopez , H., Chung , E.-S., DiNezio , P., Yeh , S.-W., and Wittenberg , A. T. On the Fragile Relationship Between El Niño and California Rainfall. *Geophysical Research Letters*, 45(2):907–915, jan 2018. ISSN 00948276. doi: 10.1002/2017GL076197. URL http://doi.wiley.com/10.1002/2017GL076197. 71

Lenssen , N. J. L., Schmidt , G. A., Hansen , J. E., Menne , M. J., Persin , A., Ruedy , R., and Zyss , D. Improvements in the uncertainty model in the Goddard Institute for Space Studies Surface Temperature (GISTEMP) analysis. *Journal of Geophysical Research: Atmospheres*, 124(12):6307–6326, jun 2019. ISSN 2169-897X. doi: 10.1029/2018JD029522. URL https://onlinelibrary.wiley.com/doi/abs/10.1029/2018JD029522. 33

Levine , X. J. and Schneider , T. Response of the Hadley Circulation to Climate Change in an Aquaplanet GCM Coupled to a Simple Representation of Ocean Heat Transport. *Journal of the Atmospheric Sciences*, 68(4):769–783, apr 2011. ISSN 0022-4928. doi: 10.1175/2010JAS3553.1. URL http://journals.ametsoc.org/doi/abs/10.1175/2010JAS3553.1. 96

L'Heureux , M. L., Takahashi , K., Watkins , A. B., Barnston , A. G., Becker , E. J., Di Liberto , T. E., Gamble , F., Gottschalck , J., Halpert , M. S., Huang , B., Mosquera-Vásquez , K., and Wittenberg , A. T. Observing and Predicting the 2015/16 El Niño. *Bulletin of the American Meteorological Society*, 98(7): 1363–1382, 2017. ISSN 00030007. doi: 10.1175/BAMS-D-16-0009.1. URL http://journals.ametsoc.org/doi/10.1175/BAMS-D-16-0009.1. 70

Liu , Z., Mehran , A., Phillips , T., and AghaKouchak , A. Seasonal and regional biases in CMIP5 precipitation simulations. *Climate Research*, 60(1):35–50, may 2014. ISSN 0936-577X. doi: 10.3354/cr01221. URL http://www.int-res.com/abstracts/cr/v60/n1/p35-50/. 45

Lorenz , E. N. The predictability of a flow which possesses many scales of motion. *Tellus*, 21(3):289–307, jan 1969. ISSN 0040-2826. doi: 10.3402/tellusa.v21i3.10086. URL https://www.tandfonline.com/doi/full/10.3402/tellusa.v21i3.10086. 81

Lu , J., Vecchi , G. A., and Reichler , T. Expansion of the Hadley cell under global warming. *Geophysical Research Letters*, 34(6):L06805, mar 2007. ISSN 0094-8276. doi: 10.1029/2006GL028443. URL http://doi.wiley.com/10.1029/2006GL028443. 96

Madden , R. A. and Ramanathan , V. Detecting Climate Change due to Increasing Carbon Dioxide. *Science*, 209(4458):763–768, aug 1980. ISSN 0036-8075. doi: 10.1126/science.209.4458.763. URL http://www.sciencemag.org/cgi/doi/10.1126/science.209.4458.763. 35

Mann , M. E., Rahmstorf , S., Kornhuber , K., Steinman , B. A., Miller , S. K., Petri , S., Coumou , D., Petri , S., Kornhuber , K., Rahmstorf , S., and Steinman , B. A. Projected Changes in Persistent Extreme Summer Weather Events: The Role of Quasi-Resonant Amplification. *Science Advances*, 4(10):eaat3272, oct 2018. ISSN 2375-2548. doi: 10.1126/sciadv.aat3272. URL http://advances.sciencemag.org/lookup/doi/10.1126/sciadv.aat3272. 60

Marvel , K., Cook , B. I., Bonfils , C. J. W., Durack , P. J., Smerdon , J. E., and Williams , A. P. Twentieth-century hydroclimate changes consistent with human influence. *Nature*, 569(7754):59–65, may 2019. ISSN 0028-0836. doi: 10.1038/s41586-019-1149-8. URL http://www.nature.com/articles/s41586-019-1149-8. 38

Medeiros , B., Stevens , B., and Bony , S. Using aquaplanets to understand the robust responses of comprehensive climate models to forcing. *Climate Dynamics*, 44(7-8):1957–1977, apr 2015. ISSN 0930-7575. doi: 10.1007/s00382-014-2138-0. URL http://link.springer.com/10.1007/s00382-014-2138-0. 52

Medellín-Azuara , J., Macewan , D., Howitt , R. E., Sumner , D. A., Lund , J. R., Scheer , J., Gailey , R., Hart , Q., Alexander , N. D., Arnold , B., Kwon , A., Bell , A., and Li , W. Economic Analysis of the 2016 California Drought on Agriculture. *Center for Watershed Sciences. University of California, Davis, California*, page 17, 2016. URL https://tinyurl.com/https-watershed-ucdavis-edu. 2

Meehl , G. A. More Intense, More Frequent, and Longer Lasting Heat Waves in the 21st Century. *Science*, 305(5686):994–997, aug 2004. ISSN 0036-8075. doi: 10.1126/science.1098704. URL http://www.sciencemag.org/cgi/doi/10.1126/science.1098704. 4

Min , S.-K., Zhang , X., Zwiers , F. W., and Hegerl , G. C. Human contribution to more-intense precipitation extremes. *Nature*, 470(7334):378–381, feb 2011. ISSN 0028-0836. doi: 10.1038/nature09763. URL http://www.nature.com/articles/nature09763. 38

Mirle , K., Uk , M. R. A., Canada , N. G., Gutzler , D., Republic , S.-k. M., Uk , D. M., Germany , T. M., Uk , D. P., and France , A. R. Detection and Attribution of Climate Change: from Global to Regional. In Intergovernmental Panel on Climate Change , editor, *Climate Change 2013 - The Physical Science Basis*, volume 9781107057, pages 867–952. Cambridge University Press, Cambridge, 2013. ISBN 9781107415324. doi: 10.1017/CBO9781107415324.022. URL https://tinyurl.com/wbtwn9e. 35

Mitas , C. M. Has the Hadley cell been strengthening in recent decades? *Geophysical Research Letters*, 32(3):L03809, 2005. ISSN 0094-8276. doi: 10.1029/2004GL021765. URL http://doi.wiley.com/10.1029/2004GL021765. 96

Mitas , C. M. and Clement , A. Recent behavior of the Hadley cell and tropical thermodynamics in climate models and reanalyses. *Geophysical Research Letters*, 33(1):n/a–n/a, jan 2006. ISSN 00948276. doi: 10.1029/2005GL024406. URL http://doi.wiley.com/10.1029/2005GL024406. 96

Mitchell , J. F. B., Wilson , C. A., and Cunnington , W. M. On Co2 climate sensitivity and model dependence of results. *Quarterly Journal of the Royal Meteorological Society*, 113(475):293–322, jul 2007. ISSN 00359009. doi: 10.1002/qj.49711347517. URL http://doi.wiley.com/10.1002/qj.49711347517. 34

Moore , J. and Ellis , A. 2014 Aerial Survey Results : California. Technical Report March, United States Department of Agriculture, 2015. URL https://tinyurl.com/vdbdqwo. 2

Myhre , G., Shindell , D., Bréon , F.-M., Collins , W., Fuglestvedt , J., Huang , J., Koch , D., Lamarque , J.-F., Lee , D., Mendoza , B., Nakajima , T., Robock , A., Stephens , G., Takemura , T., and Zhang , H. Anthropogenic and Natural Radiative Forcing. In: Climate Change 2013: The Physical Science Basis. Contribution of Working Group I to the Fifth Assessment Report of the Intergovernmental Panel on Climate Change [Stocker, T.F., D. Qin, G.-K. Plattner, M. Ti. Technical report, Cambridge University Press, Cambridge, United Kingdom and New York, NY, USA, 2013. URL https://tinyurl.com/y4lrvywd. 33

Neale , R. B., Chen , C.-C., Gettelman , A., Lauritzen , P. H., Park , S., Williamson , D. L., Conley , A. J., Garcia , R., Kinnison , D., Lamarque , J.-F., Marsh , D., Mills , M., Smith , A. K., Tilmes , S., Vitt , F., Cameron-Smith , P., Collins , W. D., Iacono , M. J., and R. C. Easter , Liu , X., Ghan , S. J., Rasch , P. J., and Taylor , M. A. Description of the NCAR Community Atmosphere Model (CAM 5.0). NCAR Technical Note NCAR/TN-486+STR, National Center for Atmospheric Research, Boulder, Colorado, 2012. URL https://tinyurl.com/uzwol2n. 42, 77

NOAA National Centers for Environmental information . Equatorial Pacific Sea Surface Temperatures. URL https://www.ncdc.noaa.gov/teleconnections/enso/indicators/sst/. 70

NOAA National Centers for Environmental information . Climate at a Glance: Regional Time Series, 2019. URL https://tinyurl.com/y29yf9tk. 64

NOAA National Centers for Environmental Information (NCEI) . U.S. Billion-Dollar Weather and Climate Disasters, 2019. URL https://www.ncdc.noaa.gov/billions/. 37

O'Brien , J. P., O'Brien , T. A., Patricola , C. M., and Wang , S.-Y. S. Metrics for understanding large-scale controls of multivariate temperature and precipitation variability. *Climate Dynamics*, 53(7-8):3805–3823, oct 2019. ISSN 0930-7575. doi: 10.1007/s00382-019-04749-6. URL http://link.springer.com/10.1007/s00382-019-04749-6. 71

O'Brien , T. A., Collins , W. D., Kashinath , K., Rübel , O., Byna , S., Gu , J., Krishnan , H., and Ullrich , P. A. Resolution dependence of precipitation statistical fidelity in hindcast simulations. *Journal of Advances in Modeling Earth Systems*, 8(2):976–990, jun 2016. ISSN 19422466. doi: 10.1002/2016MS000671. URL http://doi.wiley.com/10.1002/2016MS000671. 74, 90

OBrien , T. A., Risser , M. D., OBrien , J. P., Patricola , C. M., Paciorek , C. J., Krishnan , H., Rhoades , A. M., and Collins , W. D. Chance Rather than Trends in the Unusual 2017 California Wet Season. *In Prep.*, 2019. 54, 55, 71, 72

O'Gorman , P. a. and Schneider , T. The physical basis for increases in precipitation extremes in simulations of 21st-century climate change. *Proceedings of the National Academy of Sciences*, 106(35):14773–14777, sep 2009. ISSN 0027-8424. doi: 10.1073/pnas.0907610106. URL http://www.pnas.org/cgi/doi/10.1073/pnas.0907610106. 4, 74

Olivier , J. G. J., Van Aardenne , J. A., Dentener , F. J., Pagliari , V., Ganzeveld , L. N., and Peters , J. A. H. W. Recent trends in global greenhouse gas emissions:regional trends 1970–2000 and spatial distributionof key sources in 2000. *Environmental Sciences*, 2(2-3):81–99, jun 2005. ISSN 1569-3430. doi: 10.1080/15693430500400345. URL https://www.tandfonline.com/doi/full/10.1080/15693430500400345. 33

Otto , F. E. L., Philip , S., Kew , S., Li , S., King , A., and Cullen , H. Attributing high-impact extreme events across timescales—a case study of four different types of events. *Climatic Change*, 149(3-4):399–412, aug 2018. ISSN 0165-0009. doi: 10.1007/s10584-018-2258-3. URL http://link.springer.com/10.1007/s10584-018-2258-3. 34, 36, 37

Otto , F. E. Attribution of Weather and Climate Events. *Annual Review of Environment and Resources*, 42(1):627–646, oct 2017. ISSN 1543-5938. doi: 10.1146/annurev-environ-102016-060847. URL http://www.annualreviews.org/doi/10.1146/annurev-environ-102016-060847. 35, 36

Paciorek , C. J., Stone , D. A., and Wehner , M. F. Quantifying statistical uncertainty in the attribution of human influence on severe weather. *Weather and Climate Extremes*, 20(January):69–80, jun 2018. ISSN 22120947. doi: 10.1016/j.wace.2018.01.002. URL https://linkinghub.elsevier.com/retrieve/pii/S2212094717300841. 46

Paek , H., Yu , J.-Y., and Qian , C. Why were the 2015/2016 and 1997/1998 extreme El Niños different? *Geophysical Research Letters*, 44(4):1848–1856, 2017. ISSN 00948276. doi: 10.1002/2016GL071515. URL http://doi.wiley.com/10.1002/2016GL071515. 71, 107

Pall , P., Allen , M. R., and Stone , D. A. Testing the Clausius–Clapeyron constraint on changes in extreme precipitation under CO2 warming. *Climate Dynamics*, 28(4):351–363, jan 2007. ISSN 0930-7575. doi: 10.1007/s00382-006-0180-2. URL http://link.springer.com/10.1007/s00382-006-0180-2. 68

Pall , P., Aina , T., Stone , D. A., Stott , P. A., Nozawa , T., Hilberts , A. G. J., Lohmann , D., and Allen , M. R. Anthropogenic greenhouse gas contribution to flood risk in England and Wales in autumn 2000. *Nature*, 470(7334):382–385, feb 2011. ISSN 0028-0836. doi: 10.1038/nature09762. URL http://www.nature.com/articles/nature09762. 36

Pall , P., Patricola , C. M., Wehner , M. F., Stone , D. A., Paciorek , C. J., and Collins , W. D. Diagnosing conditional anthropogenic contributions to heavy Colorado rainfall in September 2013. *Weather and Climate Extremes*, 17(July 2016):1–6, sep 2017. ISSN 22120947. doi: 10.1016/j.wace.2017.03.004. URL https://linkinghub.elsevier.com/retrieve/pii/S2212094716300470. 36, 38

Patricola , C. M. and Wehner , M. F. Anthropogenic influences on major tropical cyclone events. *Nature*, 563(7731):339–346, nov 2018. ISSN 0028-0836. doi: 10.1038/s41586-018-0673-2. URL http://www.nature.com/articles/s41586-018-0673-2. 36

Patricola , C. M., O'Brien , J. P., Risser , M. D., Rhoades , A. M., O'Brien , T. A., Ullrich , P. A., Stone , D. A., and Collins , W. D. Maximizing ENSO as a source of western US hydroclimate predictability. *Climate Dynamics*, oct 2019. ISSN 0930-7575. doi: 10.1007/s00382-019-05004-8. URL http://link.springer.com/10.1007/s00382-019-05004-8. 100, 101, 106

Pendergrass , A. G. and Hartmann , D. L. The Atmospheric Energy Constraint on Global-Mean Precipitation Change. *Journal of Climate*, 27(2):757–768, jan 2014. ISSN 0894-8755. doi: 10.1175/JCLI-D-13-00163.1. URL http://journals.ametsoc.org/doi/abs/10.1175/JCLI-D-13-00163.1. 34

Pendergrass , A. G., Knutti , R., Lehner , F., Deser , C., and Sanderson , B. M. Precipitation variability increases in a warmer climate. *Scientific Reports*, 7(1):17966, dec 2017. ISSN 2045-2322. doi: 10.1038/s41598-017-17966-y. URL http://www.nature.com/articles/s41598-017-17966-y. 75, 76, 114

Philander , S. G. H. El Niño and La Niña. *Journal of the Atmospheric Sciences*, 42(23):2652–2662, dec 1985. ISSN 0022-4928. doi: 10.1175/1520-0469(1985)042⟨2652:ENALN⟩2.0.CO;2. URL https://tinyurl.com/vmxw99f. 73, 106

Prein , A. F., Rasmussen , R. M., Ikeda , K., Liu , C., Clark , M. P., and Holland , G. J. The future intensification of hourly precipitation extremes. *Nature Climate Change*, 7(1):48–52, jan 2017. ISSN 1758-678X. doi: 10.1038/nclimate3168. URL http://www.nature.com/articles/nclimate3168. 4

Ramos , A. M., Trigo , R. M., Liberato , M. L. R., and Tomé , R. Daily Precipitation Extreme Events in the Iberian Peninsula and Its Association with Atmospheric Rivers. *Journal of Hydrometeorology*, 16(2):579–597, apr 2015. ISSN 1525-755X. doi: 10.1175/JHM-D-14-0103.1. URL http://journals.ametsoc.org/doi/10.1175/JHM-D-14-0103.1. 83

Rauscher , S. A., O'Brien , T. A., Piani , C., Coppola , E., Giorgi , F., Collins , W. D., and Lawston , P. M. A multimodel intercomparison of resolution effects on precipitation: simulations and theory. *Climate Dynamics*, 47(7-8):2205–2218, oct 2016. ISSN 0930-7575. doi: 10.1007/s00382-015-2959-5. URL http://link.springer.com/10.1007/s00382-015-2959-5. 74

Reardon , S. Hurricane Katrina's psychological scars revealed. *Nature*, 524(7566): 395–396, aug 2015. ISSN 0028-0836. doi: 10.1038/524395a. URL http://www.nature.com/articles/524395a. 2

Risser , M. D. and Wehner , M. F. Attributable Human-Induced Changes in the Likelihood and Magnitude of the Observed Extreme Precipitation during Hurricane Harvey. *Geophysical Research Letters*, 44(24):12,457–12,464, dec 2017. ISSN 00948276. doi: 10.1002/2017GL075888. URL http://doi.wiley.com/10.1002/2017GL075888. 36

Robine , J.-M., Cheung , S. L. K., Le Roy , S., Van Oyen , H., Griffiths , C., Michel , J.-P., and Herrmann , F. R. Death toll exceeded 70,000 in Europe during the summer of 2003. *Comptes Rendus Biologies*, 331(2):171–178, feb 2008. ISSN 16310691. doi: 10.1016/j.crvi.2007.12.001. URL http://www.sciencedirect.com/science/article/pii/S1631069107003770. 2

Rutz , J. J., Steenburgh , W. J., and Ralph , F. M. Climatological Characteristics of Atmospheric Rivers and Their Inland Penetration over the Western United States. *Monthly Weather Review*, 142(2):905–921, feb 2014. ISSN 0027-0644. doi: 10.1175/MWR-D-13-00168.1. URL http://journals.ametsoc.org/doi/abs/10.1175/MWR-D-13-00168.1. 50

Salathé , E. P. Influences of a shift in North Pacific storm tracks on western North American precipitation under global warming. *Geophysical Research Letters*, 33 (19):L19820, oct 2006. ISSN 0094-8276. doi: 10.1029/2006GL026882. URL http://doi.wiley.com/10.1029/2006GL026882. 98

Santer , B. D., Wigley , T. M. L., and Jones , P. D. Correlation methods in fingerprint detection studies. *Climate Dynamics*, 8(6):265–276, jul 1993. ISSN 0930-7575. doi: 10.1007/BF00209666. URL http://link.springer.com/10.1007/BF00209666. 35

Santer , B. D., Wehner , M., Wigley , T. M. L., Sausen , R., Meehl , G. A., Taylor , K. E., Ammann , C., Arblaster , J., Washington , W. M., Boyle , J. S., and Brüggemann , W. Contributions of Anthropogenic and Natural Forcing to Recent Tropopause Height Changes. *Science*, 301(5632):479–483, jul 2003. ISSN 0036-8075. doi: 10.1126/science.1084123. URL http://www.sciencemag.org/cgi/doi/10.1126/science.1084123. 36

Santer , B. D., Taylor , K. E., Gleckler , P. J., Bonfils , C., Barnett , T. P., Pierce , D. W., Wigley , T. M. L., Mears , C., Wentz , F. J., Bruggemann , W., Gillett , N. P., Klein , S. A., Solomon , S., Stott , P. A., and Wehner , M. F. Incorporating model quality information in climate change detection and attribution studies. *Proceedings of the National Academy of Sciences*, 106(35):14778–14783, sep 2009. ISSN 0027-8424. doi: 10.1073/pnas.0901736106. URL http://www.pnas.org/cgi/doi/10.1073/pnas.0901736106. 35

Santer , B. D., Taylor , K. E., Wigley , T. M. L., Penner , J. E., Jones , P. D., and Cubasch , U. Towards the detection and attribution of an anthropogenic effect on climate. *Climate Dynamics*, 12(2):77–100, dec 1995. ISSN 0930-7575. doi: 10.1007/BF00223722. URL http://link.springer.com/10.1007/BF00223722. 35

Savtchenko , A. K., Huffman , G., and Vollmer , B. Assessment of Precipitation Anomalies in California Using TRMM and MERRA Data. *Journal of Geophysical Research: Atmospheres*, 120(16):n/a–n/a, aug 2015. ISSN 2169897X. doi: 10.1002/2015JD023573. URL http://doi.wiley.com/10.1002/2015JD023573. 71

Seager , R. and Hoerling , M. Atmosphere and Ocean Origins of North American Droughts. *Journal of Climate*, 27(12):4581–4606, jun 2014. ISSN 0894-8755. doi: 10.1175/JCLI-D-13-00329.1. URL http://journals.ametsoc.org/doi/10.1175/JCLI-D-13-00329.1. 45, 62

Seager , R., Naik , N., and Vogel , L. Does Global Warming Cause Intensified Interannual Hydroclimate Variability? *Journal of Climate*, 25(9):3355–3372, may 2012. ISSN 0894-8755. doi: 10.1175/JCLI-D-11-00363.1. URL http://journals.ametsoc.org/doi/10.1175/JCLI-D-11-00363.1. 73, 75, 99

Seager , R., Hoerling , M., Schubert , S., Wang , H., Lyon , B., Kumar , A., Nakamura , J., and Henderson , N. Causes of the 2011 to 2014 California drought. *Journal of Climate*, (xxxx):150716154721008, 2015. ISSN 0894-8755. doi: 10.1175/JCLI-D-14-00860.1. URL http://journals.ametsoc.org/doi/abs/10.1175/JCLI-D-14-00860.1. 7, 70

Shaw , T. A., Baldwin , M., Barnes , E. A., Caballero , R., Garfinkel , C. I., Hwang , Y.-T., Li , C., O'Gorman , P. A., Rivière , G., Simpson , I. R., and Voigt , A. Storm track processes and the opposing influences of climate change. *Nature Geoscience*, 9(9):656–664, sep 2016. ISSN 1752-0894. doi: 10.1038/ngeo2783. URL http://www.nature.com/articles/ngeo2783. 4, 98

Sheffield , J. and Wood , E. F. Projected changes in drought occurrence under future global warming from multi-model, multi-scenario, IPCC AR4 simulations. *Climate Dynamics*, 31(1):79–105, jul 2008. ISSN 0930-7575. doi: 10.1007/s00382-007-0340-z. URL http://link.springer.com/10.1007/s00382-007-0340-z. 4

Sheffield , J., Barrett , A. P., Colle , B., Nelun Fernando , D., Fu , R., Geil , K. L., Hu , Q., Kinter , J., Kumar , S., Langenbrunner , B., Lombardo , K., Long , L. N., Maloney , E., Mariotti , A., Meyerson , J. E., Mo , K. C., David Neelin , J., Nigam , S., Pan , Z., Ren , T., Ruiz-Barradas , A., Serra , Y. L., Seth , A., Thibeault , J. M., Stroeve , J. C., Yang , Z., and Yin , L. North American Climate in CMIP5 Experiments. Part I: Evaluation of Historical Simulations of Continental and Regional Climatology*. *Journal of Climate*, 26(23):9209–9245, dec 2013. ISSN 0894-8755. doi: 10.1175/JCLI-D-12-00592.1. URL http://journals.ametsoc.org/doi/abs/10.1175/JCLI-D-12-00592.1. 45

Sillmann , J., Kharin , V. V., Zwiers , F. W., Zhang , X., and Bronaugh , D. Climate extremes indices in the CMIP5 multimodel ensemble: Part 2. Future climate projections. *Journal of Geophysical Research Atmospheres*, 118(6):2473–2493, 2013. ISSN 21698996. doi: 10.1002/jgrd.50188. 67

Singh , D., Ting , M., Scaife , A. A., and Martin , N. California Winter Precipitation Predictability: Insights From the Anomalous 2015-2016 and 2016-2017 Seasons. *Geophysical Research Letters*, 45(18):9972–9980, sep 2018. ISSN 00948276. doi: 10.1029/2018GL078844. URL http://doi.wiley.com/10.1029/2018GL078844. 107

Stegall , S. T. and Kunkel , K. E. Simulation of Daily Extreme Precipitation over the United States in the CMIP5 30-Yr Decadal Prediction Experiment. *Journal of Applied Meteorology and Climatology*, 58(4):875–886, apr 2019. ISSN 1558-8424. doi: 10.1175/JAMC-D-18-0057.1. URL http://journals.ametsoc.org/doi/10.1175/JAMC-D-18-0057.1. 39

Stone , D. A. and Pall , P. A benchmark estimate of the effect of anthropogenic emissions on the ocean surface. *Submitted to International Journal of Climatology*, 2017. URL https://tinyurl.com/u2njtlq. 39, 43

Stone , D. A. and Allen , M. R. The End-to-End Attribution Problem: From Emissions to Impacts. *Climatic Change*, 71(3):303–318, aug 2005. ISSN 0165-0009. doi: 10.1007/s10584-005-6778-2. URL http://link.springer.com/10.1007/s10584-005-6778-2. 34, 36

Stone , D. A., Risser , M. D., Angélil , O. M., Wehner , M. F., Cholia , S., Keen , N., Krishnan , H., O'Brien , T. A., and Collins , W. D. A basis set for exploration of sensitivity to prescribed ocean conditions for estimating human contributions to extreme weather in CAM5.1-1degree. *Weather and Climate Extremes*, 19(August 2017):10–19, mar 2018. ISSN 22120947. doi: 10.1016/j.wace.2017.12.003. URL https://linkinghub.elsevier.com/retrieve/pii/S2212094717301147. 39, 42, 44

Stone , D. A., Christidis , N., Folland , C., Perkins-Kirkpatrick , S., Perlwitz , J., Shiogama , H., Wehner , M. F., Wolski , P., Cholia , S., Krishnan , H., Murray , D., Angélil , O., Beyerle , U., Ciavarella , A., Dittus , A., Quan , X.-W., and Tadross , M. Experiment design of the International CLIVAR C20C+ Detection and Attribution project. *Weather and Climate Extremes*, 24: 100206, jun 2019. ISSN 22120947. doi: 10.1016/j.wace.2019.100206. URL https://linkinghub.elsevier.com/retrieve/pii/S2212094719300027. 39, 40, 41

Stott , P. A., Stone , D. A., and Allen , M. R. Human contribution to the European heatwave of 2003. *Nature*, 432(7017):610–614, dec 2004. ISSN 0028-0836. doi: 10.1038/nature03089. URL http://www.nature.com/articles/nature03089. 36

Stott , P. A., Forest , C. E., and Building , M. Ensemble climate predictions using climate models and observational constraints. *Philosophical transactions. Series A, Mathematical, physical, and engineering sciences*, 365(1857):2029–52, 2007. ISSN 1364-503X. doi: 10.1098/rsta.2007.2075. URL http://www.ncbi.nlm.nih.gov/pubmed/17569655. 35

Svoma , B. M. and Balling , R. C. United States' Interannual Precipitation Variability Over the Past Century: Is Variability Increasing as Predicted By Models? *Physical Geography*, 31(4):307–318, jul 2010. ISSN 0272-3646. doi: 10.2747/0272-3646.31.4.307. URL https://www.tandfonline.com/doi/full/10.2747/0272-3646.31.4.307. 76, 114

Swain , D. L., Langenbrunner , B., Neelin , J. D., and Hall , A. Increasing precipitation volatility in twenty-first-century California. *Nature Climate Change*, 8(5): 427–433, may 2018. ISSN 1758-678X. doi: 10.1038/s41558-018-0140-y. URL http://www.nature.com/articles/s41558-018-0140-y. 54, 55, 75, 94, 98

Taylor , K. E., Stouffer , R. J., and Meehl , G. A. An Overview of CMIP5 and the Experiment Design. *Bulletin of the American Meteorological Society*, 93(4): 485–498, apr 2012. ISSN 0003-0007. doi: 10.1175/BAMS-D-11-00094.1. URL http://journals.ametsoc.org/doi/abs/10.1175/BAMS-D-11-00094.1. 43

Tett , S. F. B., Stott , P. A., Allen , M. R., Ingram , W. J., and Mitchell , J. F. B. Causes of twentieth-century temperature change near the Earth's surface. *Nature*, 399(6736):569–572, jun 1999. ISSN 0028-0836. doi: 10.1038/21164. URL http://www.nature.com/articles/21164. 35

Trenberth , K. Changes in precipitation with climate change. *Climate Research*, 47(1):123–138, mar 2011. ISSN 0936-577X. doi: 10.3354/cr00953. URL http://www.int-res.com/abstracts/cr/v47/n1-2/p123-138/. 4, 72

Trenberth , K. E. Conceptual Framework for Changes of Extremes of the Hydrological Cycle with Climate Change. 1999. doi: https://doi.org/10.1023/A:1005488920935. URL https://doi.org/10.1023/A:1005488920935. 34

Trenberth , K. E., Dai , A., Rasmussen , R. M., and Parsons , D. B. The Changing Character of Precipitation. *Bulletin of the American Meteorological Society*, 84 (9):1205–1218, sep 2003. ISSN 0003-0007. doi: 10.1175/BAMS-84-9-1205. URL http://journals.ametsoc.org/doi/10.1175/BAMS-84-9-1205. 34, 102

Tsonis , A. A. Widespread increases in low-frequency variability of precipitation over the past century. *Nature*, 382(6593):700–703, aug 1996. ISSN 00280836. doi: 10.1038/382700a0. URL http://www.nature.com/articles/382700a0. 75, 76, 114

Vahedifard , F., AghaKouchak , A., Ragno , E., Shahrokhabadi , S., and Mallakpour , I. Lessons from the Oroville dam. *Science*, 355(6330):1139.2–1140, mar 2017. ISSN 0036-8075. doi: 10.1126/science.aan0171. URL http://www.sciencemag.org/lookup/doi/10.1126/science.aan0171. 54

Van der Wiel , K., Kapnick , S. B., van Oldenborgh , G. J., Whan , K., Philip , S., Vecchi , G. A., Singh , R. K., Arrighi , J., and Cullen , H. Rapid attribution of the August 2016 flood-inducing extreme precipitation in south Louisiana to climate change. *Hydrology and Earth System Sciences*, 21(2): 897–921, feb 2017. ISSN 1607-7938. doi: 10.5194/hess-21-897-2017. URL https://www.hydrol-earth-syst-sci.net/21/897/2017/. 38

Vano , J. A., Miller , K., Dettinger , M. D., Cifelli , R., Curtis , D., Dufour , A., Olsen , J. R., and Wilson , A. M. Hydroclimatic Extremes as Challenges for the Water Management Community: Lessons from Oroville Dam and Hurricane Harvey. *Bulletin of the American Meteorological Society*, 100(1):S9–S14, jan 2019. ISSN 0003-0007. doi: 10.1175/BAMS-D-18-0219.1. URL http://journals.ametsoc.org/doi/10.1175/BAMS-D-18-0219.1. 54, 71

Wang , S.-Y., Hipps , L., Gillies , R. R., and Yoon , J.-H. Probable causes of the abnormal ridge accompanying the 2013-2014 California drought: ENSO precursor and anthropogenic warming footprint. *Geophysical Research Letters*, 41(9): 3220–3226, may 2014. ISSN 00948276. doi: 10.1002/2014GL059748. URL http://doi.wiley.com/10.1002/2014GL059748. 70

Wang , S.-Y. S., Yoon , J.-H., Becker , E., and Gillies , R. California from drought to deluge. *Nature Climate Change*, 7(7):465–468, jul 2017. ISSN 1758-678X. doi: 10.1038/nclimate3330. URL http://www.nature.com/articles/nclimate3330. 71

Westra , S. and Sharma , A. An Upper Limit to Seasonal Rainfall Predictability? *Journal of Climate*, 23(12):3332–3351, jun 2010. ISSN 0894-8755. doi: 10.1175/2010JCLI3212.1. URL http://journals.ametsoc.org/doi/10.1175/2010JCLI3212.1. 81

Wilbanks , T. and Fernandez , S. *Climate Change and Infrastructure, Urban Systems, and Vulnerabilities*. Island Press/Center for Resource Economics, Washington, DC, 2014. ISBN 978-1-59726-469-3. doi: 10.5822/978-1-61091-556-4. URL http://link.springer.com/10.5822/978-1-61091-556-4. 5

Williams , I. N. and Patricola , C. M. Diversity of ENSO Events Unified by Convective Threshold Sea Surface Temperature: A Nonlinear ENSO Index. *Geophysical Research Letters*, 45(17):9236–9244, sep 2018. ISSN 00948276. doi: 10.1029/2018GL079203. URL http://doi.wiley.com/10.1029/2018GL079203. 100, 106

Zhang , X., Alexander , L., Hegerl , G. C., Jones , P., Tank , A. K., Peterson , T. C., Trewin , B., and Zwiers , F. W. Indices for monitoring changes in extremes based on daily temperature and precipitation data. *Wiley Interdisciplinary Reviews: Climate Change*, 2(6):851–870, nov 2011. ISSN 17577780. doi: 10.1002/wcc.147. URL http://doi.wiley.com/10.1002/wcc.147. 41, 55, 56

Zhou , Y. and Kim , H. M. Prediction of atmospheric rivers over the North Pacific and its connection to ENSO in the North American multi-model ensemble (NMME). *Climate Dynamics*, 51(5-6):1623–1637, 2018. ISSN 14320894. doi: 10.1007/s00382-017-3973-6. URL http://dx.doi.org/10.1007/s00382-017-3973-6. 83

Zwiers , F. W., Alexander , L. V., Hegerl , G. C., Knutson , T. R., Kossin , J. P., Naveau , P., Nicholls , N., Schär , C., Seneviratne , S. I., and Zhang , X. *Climate Extremes: Challenges in Estimating and Understanding Recent Changes in the Frequency and Intensity of Extreme Climate and Weather Events*, pages 339–389. Springer Netherlands, Dordrecht, 2013. ISBN 978-94-007-6692-1. doi: 10.1007/978-94-007-6692-1_13. URL https://tinyurl.com/snkhy3q. 35